Title

Viscoelastic Behavior and Dynamics of Glass-Forming Liquids in Bulk and under Nanoconfinement

Author

Xia, Yiqing

Publication Date

2021

Peer reviewed|Thesis/dissertation

Viscoelastic Behavior and Dynamics of Glass-Forming Liquids in Bulk and under Nanoconfinement

By

YIQING XIA
DISSERTATION

Submitted in partial satisfaction of the requirements for the degree of

DOCTOR OF PHILOSOPHY

in

Materials Science and Engineering

in the

OFFICE OF GRADUATE STUDIES

of the

UNIVERSITY OF CALIFORNIA

DAVIS

Approved:

_____

Sabyasachi Sen, Chair

_____

Yayoi Takamura

_____

Roopali Kukreja

Committee in Charge

2021

Viscoelastic Behavior and Dynamics of Glass-Forming Liquids in Bulk and under Nanoconfinement

Abstract

A detailed knowledge of the atomic structure of glasses is of enormous significance in understanding the structure-property relationships in these materials. On the other hand, the dynamical behavior of their parent supercooled liquids is intimately linked to the materials' viability for all stages of industrial glass production. However, the atomistic mechanism of viscous flow and the structural control on the viscoelastic behavior and the associated relaxation phenomena in supercooled inorganic glass-forming liquids remain poorly understood to date. In addition, the structure and properties of a liquid can be quite different as the liquid volume reaches a length scale of several nanometers in confined geometries. These nanoconfined liquids display a plethora of intriguing behavior including the well-known melting point depression and the nonuniversal depression/elevation of the glass transition temperature. Despite extensive experimental and simulation studies on nanoconfined fluids, the atomistic mechanisms responsible for such behavior remain controversial and largely unresolved.

This dissertation presents the studies of the viscoelastic behavior of chalcogenide and phosphate glass-forming liquids investigated using a combination of small-amplitude oscillatory and steady shear parallel-plate rheometry and high-temperature nuclear magnetic resonance (NMR) spectroscopy in order to probe the corresponding structural relaxation processes associated with their viscous flow in the bulk state. The rheological spectra of these liquids reveal the presence of a slow and a fast relaxation process in these liquids, which could be attributed to the bond scission/renewal, and the segmental chain motion dynamics, respectively. The existence of the

latter process was directly observed in short-chain phosphate liquids by high-temperature ^{31}P dynamical NMR spectroscopy. The network connectivity increases in As-Se and Ge-Se glass-forming liquids upon progressive addition of As/Ge to Se, which is manifested in a floppy-to-rigid transition of the dynamics. On the other hand, the phosphate network becomes increasingly cross-linked as either P_2O_5 is added to a metaphosphate composition or a high field-strength modifier cation replaces a low field strength cation in the structure of a metaphosphate composition. The attendant compositional evolution of the conformational entropy of Se chain segments in chalcogenides or phosphate chain segments in Na-Zn metaphosphates is shown to be related to the corresponding variation in their fragility indices.

The results of calorimetric and ^{2}H NMR spectroscopic studies of the thermodynamic and kinetic transitions of nanoconfined liquids are also reported. Nanoconfined supercooled water displays a strong dynamical heterogeneity with the coexistence of both mobile liquid-like and immobile solid-like water molecules at temperatures lower than the bulk melting point, consistent with a layer-by-layer solidification process. In the extreme case of confined media with bimodal pore structures, the spatial heterogeneity in the dynamics of both water and glass-forming supercooled ortho-terphenyl is preserved over a length scale of several angstroms. Collectively, these results suggest a mechanistic relationship between the structural and dynamical heterogeneities in nanoconfined fluids.

Acknowledgement

Firstly, I would like to express my sincere gratitude to my advisor Professor Sabyasachi Sen for his guidance in my education and on the research during the last five years. The success in finishing my degree would not have been possible without the invaluable insights and guidance from him through this journey. Deepest appreciation and gratitude go out to Professor Sen. Also, a special thanks to Dr. Bruce Aitken for the collaborations and insightful advice on the project. Additional thanks are provided to Professor Yayoi Takamura and Professor Roopali Kukreja for serving on my dissertation committee.

I would also like to acknowledge all of my group members, Dr. Maxwell Marple, Dr. Weidi Zhu, Bing Yuan and Hao Chen for the many insightful talks and collaborations. Additional thanks to Maxwell and Weidi for the guidance on the equipment operation and setting up a good example of researcher. And thanks to Bing for the many inspiring conversations and help during the COVID-19 pandemic.

A great deal of gratitude goes out to Professor Subhash Risbud, Professor Michael H. Bartl and Professor Milind Deo for many valuable advice on the MUSE project. Extended thanks go out to all of my colleagues in the MUSE EFRC center for the collaborations and for making MUSE a joyful center to be in. I would like to thank Ping Yu for assistance and guidance with the use of solid-state NMR.

Lastly, I would like to thank my parents for their unfailing love and encouragement during my whole life. The same gratitude and love goes out to my girlfriend Jialin Zhu. Their companionship across the Pacific Ocean is essential for overcoming all the difficulties through the journey.

Table of Contents

List of Figures

List of Tables

Chapter 1

Introduction

1.1 Background and Objective

Glasses are ubiquitous in both nature and in various technological applications. As a thermodynamically stable liquid is rapidly cooled below its melting point, instead of crystallization through a first-order phase transition, it may enter a thermodynamically metastable supercooled liquid state, which is in dynamical equilibrium. With further lowering of temperature, the viscosity of the supercooled liquid continues to increase, and the timescale of structural relaxation will increase to a point where, upon further lowering in temperature the liquid is no longer able to remain in dynamical equilibrium at the timescale of experimental observation. At this point the liquid is said to undergo a glass transition and its first order thermodynamic properties such as enthalpy or volume will deviate from the equilibrium liquid trend to the trend corresponding to the glassy state [1]. This liquid-to-glass transition is elucidated in an enthalpy vs. temperature plot (Fig. 1-1).

Though the glass transition has been extensively studied in the past several decades, its physical nature remains one of the most interesting open problems in condensed matter physics to date [2–8]. Particularly, a fundamental understanding of the rearrangements of atoms/molecules in a supercooled liquid that undergo a dynamical slowdown leading to the liquid-to-glass transition is key, as these processes are also responsible for the structural relaxation and viscous flow that control all stages of the industrial glass production and processing including melting, forming and annealing. These dynamical processes do not only depend on the external variables such as

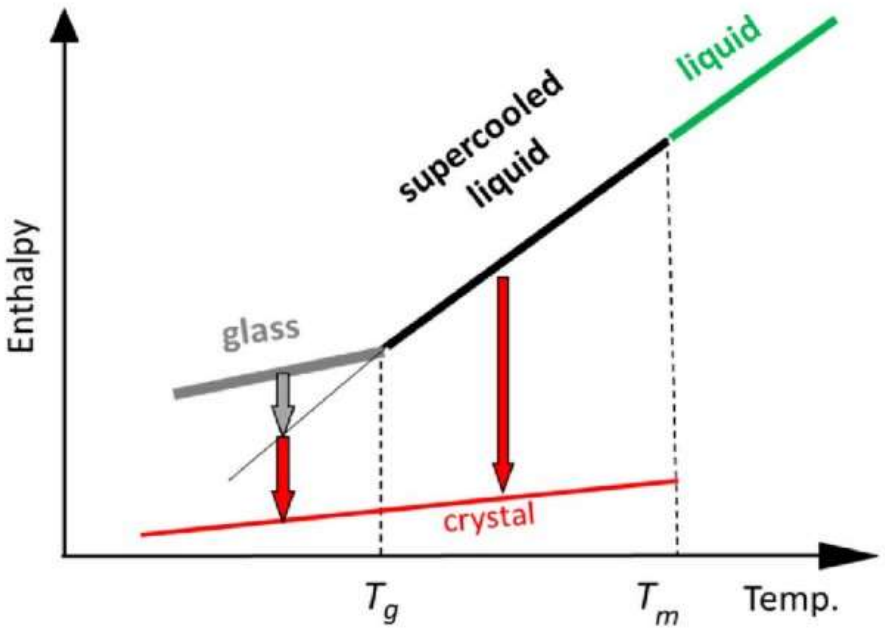

Figure 1-1 Enthalpy versus temperature diagram showing the phase transition (red line) and the glass transition (black and grey line) of a glass-forming liquid. Upon cooling below its melting point T_m, the liquid enters either the thermodynamically stable crystal regime or the supercooled regime and subsequently the glassy state through the dynamic glass transition at the glass transition temperature T_g. Vertical dashed lines denote T_m and T_g, respectively. Figure is taken from [1].

temperature and pressure but also are sensitive functions of the topology and connectivity of the structural network. For example, transport coefficients such as viscosity of a glass-forming liquid, can increase dramatically by nearly 14-15 orders of magnitude upon cooling from the melting point T_m to temperatures close to the glass transition T_g and it determines the melting condition, working range, softening point, and annealing temperature, all crucial processing parameters in the glass industry [9]. These transport coefficients are a macroscopic manifestation of the atomic/molecular dynamics in these liquids, which can be directly probed using techniques such as high-temperature dynamical nuclear magnetic resonance (NMR) spectroscopy. For example, high-temperature ^{11}B NMR spectroscopic studies of alkali borate liquids have shown that the timescale of the chemical exchange between 3- and 4- coordinated B atoms in simple alkali borate liquids via B-O bond scission-renewal process are similar to that of the viscoelastic relaxation

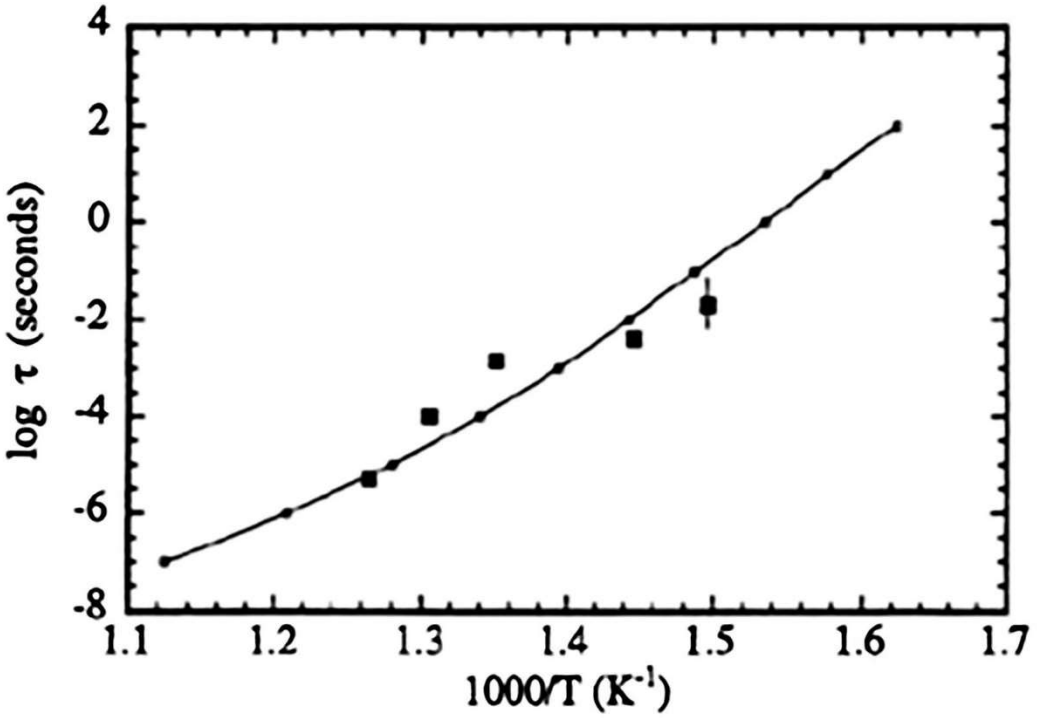

Figure 1-2 Temperature dependence of the shear relaxation timescale (solid line) of $(Na_2O)_{10}$-$(B_2O_3)_{90}$ liquid is compared with the timescale of borate species exchange obtained from 1D ^{11}B NMR line shape simulation (filled squares). Figure is taken from [10].

under shear stress of these liquids (Fig. 1-2) [10]. Therefore, close mechanistic associations can be made between the local bond scission/renewal dynamics and the viscous flow of these liquids.

On the other hand, the dynamical behavior and transport properties of liquids can be strongly altered upon nanoconfinement in natural or architected geometries [11–15]. As a liquid is confined in nanometer scale geometries such as nanopores, nanochannels, nanotubes, or other complex nanometer-sized spaces, it displays noticeably different behavior compared to its bulk counterpart [15–24]. The anomalous thermodynamic and kinetic transitions of fluids confined within nanometer-sized pores of solid materials are two such interesting and well-known effects of spatial confinement (Fig. 1-3). An atomistic understanding of the associated physicochemical processes is of enormous significance for both fundamental science and technological applications

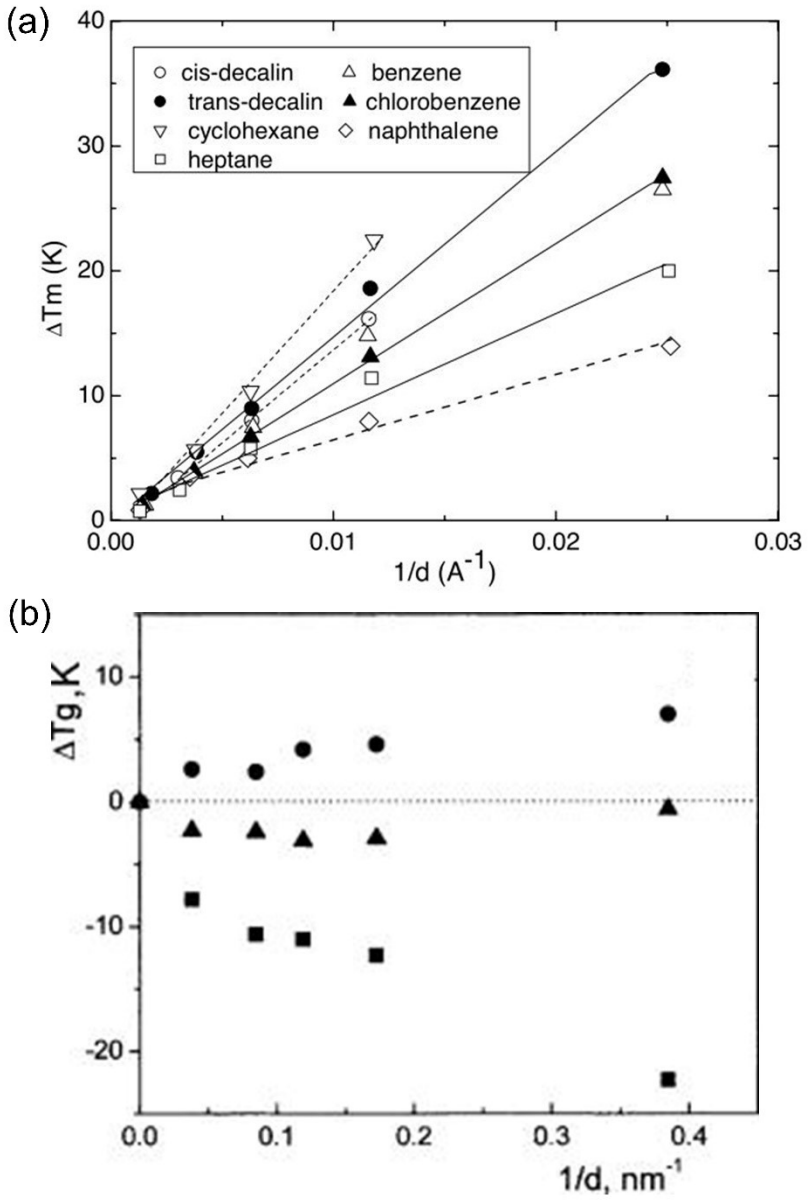

Figure 1-3 (a) Melting temperature depression as a function of the inverse of pore diameter for small molecules confined in nanopores. Lines and dashed lines through data are guide to the eyes. Figure is taken from [23]. (b) T_g change relative to the bulk as a function of pore diameter for ortho-terphenyl (squares), salol (triangles) and glycerol (circles). Figure is taken from [24].

as diverse as water transportation across cell membranes in aquaporin nanochannels, oil extraction from sedimentary rocks, and nanofluidics for biological assays [16,17,25,26]. The effects of spatial confinement can be attributed to either the finite physical size of the confining space or the atomistic interactions at the liquid-confining medium interface. While the melting point

depression of molecular liquids is found to be proportional to the inverse of the length scale of confinement, the response of the glass transition is observed to be nonuniversal, i.e. T_g can either increase or decrease for nanoconfined liquids (Fig. 1-3). In spite of extensive studies using a wide range of molecular modeling and experimental techniques, unambiguous mechanisms at the atomic level have rarely been established to explain these behaviors associated with the dynamical differences between liquids in the bulk and under nanoconfinement.

In this dissertation, I present the results of two sets of studies: one of them investigates the role of network connectivity and topology on the viscoleastic behavior and shear relaxation in supercooled glass-forming phosphate and chalcogenide liquids in the bulk, and the other focuses on the dynamical processes in liquids under nanoconfinement in relation to the thermodynamics of melting/freezing transition and the kinetics of glass transition.

1.2 Viscoelastic Behavior and Shear Relaxation in Bulk Glass-Forming Liquids

As noted above, the dynamical processes in supercooled glass-forming liquids display a remarkable slowdown upon cooling and liquids become increasingly viscous as temperature approaches T_g. The temperature dependence of viscosity can be written as $\eta = \eta_0 exp^{E(T)/RT}$, where $E(T)$ is the activation energy of the viscous flow and R is the ideal gas constant. If the activation energy is temperature independent, then the viscosity curve obeys an Arrhenius behavior as a function of temperature. Conversely, the temperature dependence of viscosity displays an increasingly non-Arrhenius behavior as the activation energy becomes dependent on temperature. To compare the manner in which different liquids becomes viscous as T_g is approached, the viscosity is typically plotted as a function of T_g/T, known as the Angell plot, shown in Fig. 1-4

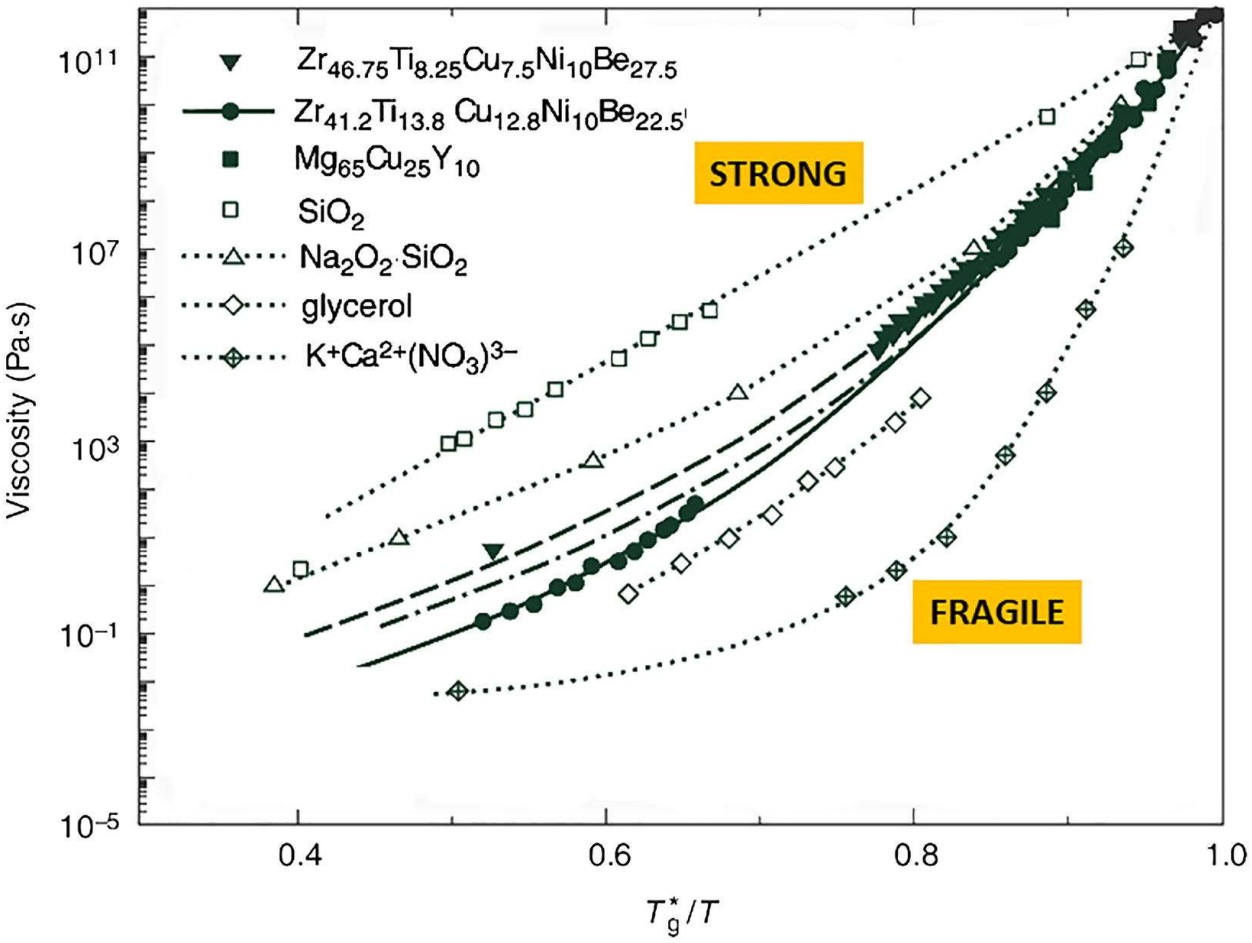

Figure 1-4 Temperature dependence of viscosity of a wide variety of glass-forming liquids in a scaled temperature T_g/T representation. Here T_g is defined as a temperature where viscsoity is 10^{12} Pa·s. Note the "strong-fragile" classification scheme. Strong (fragile) liquids are characterized by activation energy of viscous flow that is weakly (strongly) dependent on temperature. Figure is taken from [10].

[10]. It may be noted that for materials like silica, the viscosity curve is Arrhenius-like and such liquids are termed 'strong', while a large deviation from the Arrhenius behavior results in a so called 'fragile' liquid, such as the ionic liquid KNO_3-$Ca(NO_3)_2$. The degree of departure from the Arrhenius behavior in viscosity can be described by the fragility index m expressed as:

$$m = \left.\frac{d log\eta(T)}{d(T_g/T)}\right|_{T=T_g} \qquad (1\text{-}2)$$

which is the slope of viscosity in log scale at T_g. Recent studies by Sidebottom and coworkers have shown a universal trend of the fragility index m as a function of structural connectivity (Fig. 1-5) [27–30]. This result suggests an underlying universality in the relationship between the topology i.e. the spatial arrangements at short and intermediate range, and connectivity of the structural network and the temperature dependence of its shear relaxation timescale.

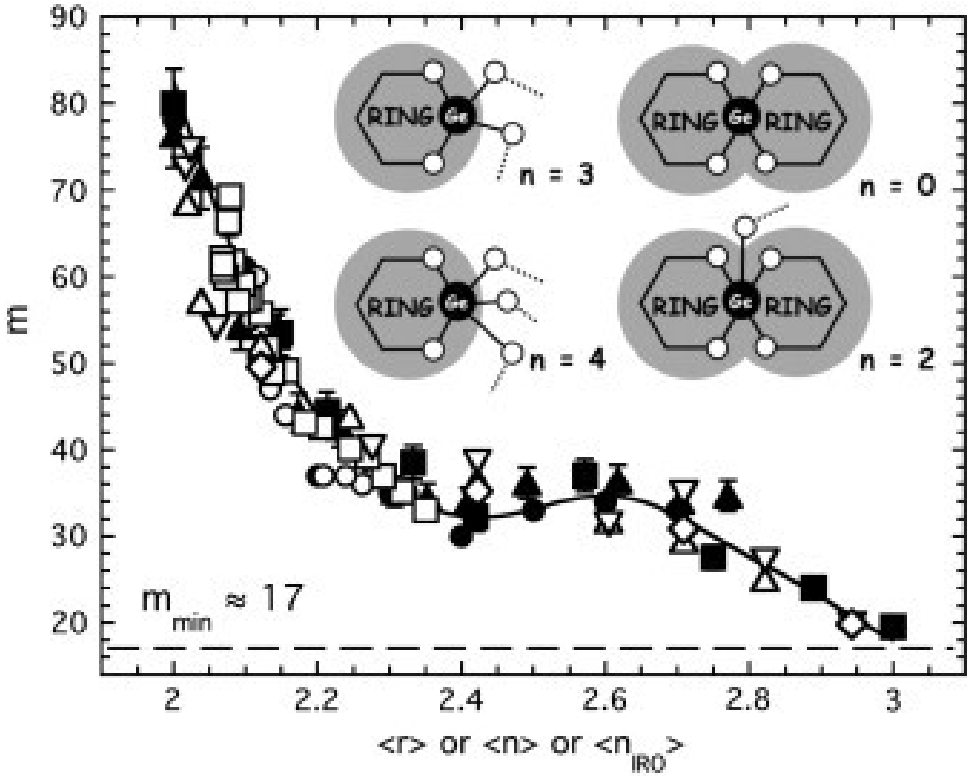

Figure 1-5 The fragility of chalcogenide $Se_x(As_{0.5}Ge_{0.5})_{1-x}$ glasses (filled circles) as a function of average coordination number, $\langle r \rangle$, follows an equivalent dependence as do a series of $(Na_2O)_x(P_2O_5)_{1-x}$ (filled squares) and $(Al(PO_3)_3)_x(NaPO_3)_{1-x}$ (filled triangles) glasses as a function of the average bridging oxygen bond number, $\langle n \rangle$ and $(Li_2O)_x(B_2O_3)_{1-x}$ (open circles), $(Na_2O)_x(B_2O_3)_{1-x}$ (open squares), $(Na_2O)_x(GeO_2)_{1-x}$ (open upright triangles), $(K_2O)_x(GeO_2)_{1-x}$ (open inverted triangles) and $(Rb_2O)_x(GeO_2)_{1-x}$ (open diamonds) glasses as a function of the effective number of bridging oxide bonds per boron/germanium atom $\langle n_{IRO} \rangle$. Error bars reflect a 5% uncertainty in determining the fragility and the solid line is only a guide for the eye. A minimum permissible fragility of m =17 is indicated by the horizontal dashed line and the inset contains illustrations of the four possible Ge atom configurations which include one or more rings as well as values for their effective connectivity. Figure is taken from [27].

Chalcogenide glasses are a class of technologically important materials that are characterized by energetically similar covalent bonds and by a wide range of network connectivity. For chalcogenide glass systems, the network connectivity or the average coordination number $\langle r \rangle$ is defined as $\langle r \rangle = \sum_i x_i r_i$ where x_i and r_i are the mole fraction and coordination number of species i in the system, respectively. Similarly, the structure of phosphate glasses can be easily transformed from a 3D network for P_2O_5 which comprises of PO_4 tetrahedra with three P–O–P linkages per tetrahedron, upon addition of modifier alkali or alkaline-earth oxides, to metaphosphates consisting predominantly of chains of corner-sharing PO_4 tetrahedra with two bridging oxygen bonds. The structural connectivity $\langle n \rangle$ in this case is defined as the average number of bridging oxygen bonds per phosphorus atom. Hence, a wide range of network connectivity can be achieved in chalcogenide and phosphate systems within their large composition range of glass formation, providing model systems to study the relationships between the atomic structure, corresponding dynamical processes and viscoelastic relaxation in these liquids. The viscoelastic behavior of the glass-forming liquids studied here are characterized by

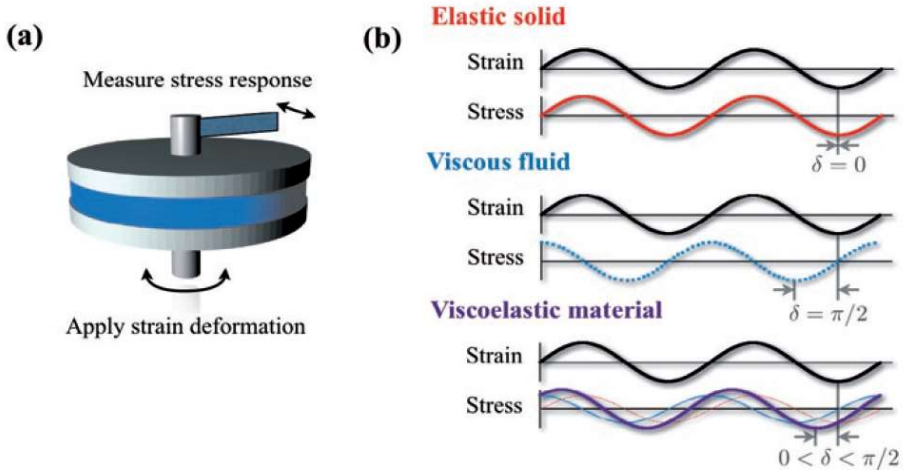

Figure 1-6 (a) Schematic representation of a typical rheometry setup, with the sample placed between two plates. (b) Schematic stress response to oscillatory strain deformation for an elastic solid, a viscous fluid and a viscoelastic material. Figure is taken from [31].

oscillatory parallel plate rheometry (Fig. 1-6) and with dynamical NMR spectroscopy, using line shape simulation [10]. In oscillating parallel plate rheometry a sinusoidal shear deformation is applied by rotating the upper plate with angular frequency ω at controlled temperatures. The resultant stress response is measured and characterized by the complex modulus G^* consisting of G' the storage modulus and G'' the loss modulus. As depicted in Fig. 1-6, the stress and strain are in phase and out of phase for purely elastic and viscous materials, respectively [31]. The storage modulus measures the stored energy, representing the solid-like (elastic) contributions to the measured stress response. The loss modulus measures the energy dissipated, representing fluid-like contributions to the stress response. The absolute value of complex viscosity can then be determined as $|\eta^*| = \frac{|G^*|}{\omega}$. All three parameters G', G'' and $|\eta^*|$ can then be obtained over a range of temperatures, as a function of angular frequency ω. When the frequency is low, the response of a liquid is predominantly viscous with $G'' > G'$. On the other hand, at high enough frequencies the viscoelastic liquid can only respond elastically and $G' > G''$. Thus, the relaxation timescale is obtained as the reciprocal of the frequency value at G' - G'' crossovers. The temperature dependence of the shear relaxation timescale can then be compared to the timescales obtained from dynamical NMR spectroscopic measurements for specific dynamical processes such as bond scission/renewal or chain reorientation in the liquid [10]. In this way, the dynamics responsible for the structural relaxation under shear can be investigated in supercooled glass-forming liquids with different network connectivity and topology. Consequently, a fundamental atomistic understanding of the viscous flow and structural relaxation can be established.

With these objectives in mind, the viscoelastic behavior and shear relaxation of chalcogenide and phosphate glass-forming liquids have been studied in Chapters 2, 3, 4 and 5. Particularly, in Chapter 2, small amplitude oscillatory shear (SAOS) parallel plate rheometry is

used to characterize the viscoelastic relaxation and its atomistic mechanism in As-Se and Ge-Se binary glass-forming liquids as a function of the network connectivity [32]. As the network connectivity increases upon addition of Ge/As to Se, the relaxation process corresponding to the segmental motion of Se chains gradually disappears as the structure becomes more crosslinked, displaying a dynamical rigidity transition. In Chapters 3, 4 and 5, the SAOS parallel plate rheometry is combined with dynamical NMR spectroscopy to characterize the structural mechanism for shear relaxation in phosphate glass-forming liquids where the structural connectivity is modified by varying the field strength of the modifier cations. The results of these works allow for a direct understanding of relationship between the network connectivity, conformational entropy and fragility of glass-forming liquids and suggest the need for significant revision to the corresponding theoretical models that exist in the literature.

1.3 Thermodynamic and Kinetic Transitions of Liquids under Nanoconfinement

The thermodynamic and kinetic processes involved in the flow, structural transitions, and freezing or melting behavior of nanoconfined liquids are central to the understanding and controlling of a wide range of processes and applications in biology, materials sciences, catalysis, nanofluidics, and geochemistry. Water is perhaps the most ubiquitous and intriguing liquid in this regard to study the melting/freezing point depression behavior. Though the physical nature of the dynamics and solidification process of water under nanoconfinement remains controversial, a structure consisting of distinct spatial regimes of water molecules is proposed in recent experimental and simulation studies [21,33–42]. The outermost layer bound to the pore surface is a statistical monolayer of water molecules (~ 0.3 nm thick). This layer is also known as the 'non-freezing' monolayer, which remain unfrozen even down to ~ 190 K. Beyond this layer, water molecules extending to ~ 1 nm from the pore wall are in the 'shell' regime and are strongly

structured by the surface. The 'shell' water is characterized with significantly lower mobility and higher density, compared to that of bulk water. The rest of the water molecules are in the 'core' region and are believed to be similar to those in bulk water. Therefore, a stepwise solidification of nanoconfined water may result from such pronounced spatial heterogeneity.

As noted above, in contrast to freezing/melting transition, glass-forming liquids bypass crystallization and undergo a dynamical slowdown upon cooling. The kinetic event of glass transition is observed to be strongly affected by nanoconfinement, which is typically manifested in calorimetric measurements as an increase or decrease in T_g with increasing confinement [23,41]. The structural relaxation in a supercooled liquid can be related to the dynamics within the cooperatively rearranging regions (CRR) in the structure. CRR is defined as a subset of atoms/molecules that can rearrange into alternative configurations independently of its environment. Thus, cooling results in an increase in the size of the CRRs and a concomitant lowering of the configurational entropy of the system. In this scenario the finite size and interfacial effects of confinement on the dynamics can be described as follows. First, when the confinement length scale becomes comparable to or smaller than the size of CRR, the cooperative molecular dynamics responsible for structural relaxation is greatly diminished, resulting in a drop in T_g. Second, as the confinement length scale decreases, a stronger interfacial effect is achieved by increased numbers of molecules interacting with pore walls. This fact may result in a change in the structure and density of the liquid, which in turn can lead to a different mechanism altogether for its structural relaxation. For example, a dynamical ^{13}C NMR spectroscopic study showed that the isotropic molecular tumbling motion associated with structural relaxation in bulk glycerol differs inherently from that in glycerol under extreme nanoconfinement [43]. *In situ* high-pressure ^{13}C NMR measurements revealed that such a behavior was related to the increasing molecular

packing and density of glycerol under strong confinement [44]. Thus, an atomistic investigation of the structure and dynamics is of great importance to understand the anomalous thermodynamic phase behavior and kinetic events of liquids under confinement.

To achieve these objectives, in Chapters 6 and 7, the dynamics of water and supercooled ortho-terphenyl (OTP) liquid confined in mesoporous silica matrices are characterized using a combination of differential scanning calorimetry and ^{2}H wideline NMR spectroscopy in order to investigate the freezing process of nanoconfined water and the glass transition of supercooled OTP liquid, respectively. Notably, extreme dynamical heterogeneity is observed for liquids confined in mesoporous silica with bimodal pore structures with interconnected pores of different size. This work reports the first observation of two distinct melting points of water, and two $T_g's$ of glass-forming liquids corresponding to two specific pore types and provide insights into the relation between the structural and dynamical heterogeneities in nanoconfined liquids.

The contents of this dissertation have been published in separate journal articles. Chapter 2 in the *Journal of Chemical Physics*, Chapter 3 in the *Journal of Non-Crystalline Solids*, Chapter 4 in the *Journal of Chemical Physics*, Chapter 6 in *Scientific Reports* and Chapter 7 in the *Frontiers in Physics* [45–49]. Chapter 5 is to be submitted to *Journal of Physical Chemistry B*.

References

[1] E.D. Zanotto, J.C. Mauro, The glassy state of matter: Its definition and ultimate fate, J. Non. Cryst. Solids. 471 (2017) 490–495.

[2] C.A. Angell, Perspective On the Glass Transition, J. Phys. Chem. Solids. 49 (1988) 863–871.

[3] C.A. Angell, Relaxation in Complex Systems, in: K.L. Ngai, G.B. Wright (Eds.), National Technical Center, U.S. Department of Commerce, Springfield, VA, 1985: pp. 3–12.

[4] P.W. Anderson, Through the Glass Lightly, Science (80-.). 267 (1995) 1615–1616.

[5] A.K. Varshneya, Fundamentals of inorganic glasses, 2003.

[6] J.C. Dyre, Colloquium: The Glass Transition and Elastic Models of Glass-Forming Liquids, Rev. Mod. Phys. 78 (2006) 953–972.

[7] S.A. Kivelson, G. Tarjus, In search of a theory of supercooled liquids, Nat. Mater. 7 (2008) 831–833.

[8] A. Cavagna, Supercooled Liquids for Pedestrians, Phys. Rep. 476 (2009) 51–124.

[9] M.I. Ojovan, Viscous Flow and the Viscosity of Melts and Glasses, Phys. Chem. Glas. Eur. J. Glas. Sci. Technol. B. 53 (2012) 143–150.

[10] S. Sen, Dynamics in inorganic glass-forming liquids by NMR spectroscopy, Prog. Nucl. Magn. Reson. Spectrosc. 116 (2020) 155–176.

[11] F. Du, B. Nojabaei, Estimating diffusion coefficients of shale oil, gas, and condensate with nano-confinement effect, J. Pet. Sci. Eng. 193 (2020) 107362.

[12] D. Majolino, C. Corsaro, V. Crupi, V. Venuti, U. Wanderlingh, Water diffusion in nanoporous glass: An NMR study at different hydration levels, J. Phys. Chem. B. 112 (2008) 3927–3930.

[13] T.X. Nguyen, S.K. Bhatia, Some anomalies in the self-diffusion of water in disordered carbons, J. Phys. Chem. C. 116 (2012) 3667–3676.

[14] C. Sendner, D. Horinek, L. Bocquet, R.R. Netz, Interfacial water at hydrophobic and hydrophilic surfaces: Slip, viscosity, and diffusion, Langmuir. 25 (2009) 10768–10781.

[15] E. Mohagheghian, H. Hassanzadeh, Z. Chen, Evaluation of Shale-Gas-Phase Behavior under Nanoconfinement in Multimechanistic Flow, Ind. Eng. Chem. Res. 59 (2020) 15048–15057.

[16] R. Guégan, Confinement effects on water structure in membrane lyotropic phases, J. Colloid Interface Sci. 358 (2011) 485–490.

[17] J.L. Skinner, P.A. Pieniazek, S.M. Gruenbaum, Vibrational spectroscopy of water at interfaces, Acc. Chem. Res. 45 (2012) 93–100.

[18] R.B. Schoch, J. Han, P. Renaud, Transport phenomena in nanofluidics, Rev. Mod. Phys. 80 (2008) 839–883.

[19] N. Alcantar, J. Israelachvili, J. Boles, Forces and ionic transport between mica surfaces:

Implications for pressure solution, Geochim. Cosmochim. Acta. 67 (2003) 1289–1304.

[20] I.C. Bourg, G. Sposito, Connecting the molecular scale to the continuum scale for diffusion processes in smectite-rich porous media, Environ. Sci. Technol. 44 (2010) 2085–2091.

[21] F. Mallamace, M. Broccio, C. Corsaro, A. Faraone, D. Majolino, V. Venuti, L. Liu, C.-Y. Mou, S.-H. Chen, Evidence of the existence of the low-density liquid phase in supercooled, confined water, Proc. Natl. Acad. Sci. 104 (2007) 424–428.

[22] K.S. Andrikopoulos, A.G. Kalampounias, S.N. Yannopoulos, Confinement effects on liquid-liquid transitions: pore size dependence of sulfur's living polymerization, (n.d.).

[23] M. Alcoutlabi, G.B. McKenna, Effects of confinement on material behaviour at the nanometre size scale, J. Phys. Condens. Matter. 17 (2005) R461–R524.

[24] O. Trofymluk, A.A. Levchenko, A. Navrotsky, Interfacial effects on vitrification of confined glass-forming liquids, J. Chem. Phys. 123 (2005) 8966.

[25] E.G. Solveyra, E. De La Llave, V. Molinero, G.J.A.A. Soler-Illia, D.A. Scherlis, Structure, dynamics, and phase behavior of water in TiO2 nanopores, J. Phys. Chem. C. 117 (2013) 3330–3342.

[26] C.I. Lynch, S. Rao, M.S.P. Sansom, Water in Nanopores and Biological Channels: A Molecular Simulation Perspective, Chem. Rev. 120 (2020) 10298–10335.

[27] D.L. Sidebottom, T.D. Tran, S.E. Schnell, Building up a weaker network: The effect of intermediate range glass structure on liquid fragility, J. Non. Cryst. Solids. 402 (2014) 16–20.

[28] D.L. Sidebottom, D. Vu, Assessing the network connectivity of modifier ions in metaphosphate glass melts : A dynamic light scattering study of Na-Zn mixtures, J. Chem. Phys. 145 (2016) 164503.

[29] T.D. Tran, D.L. Sidebottom, Glass-forming dynamics of aluminophosphate melts studied by photon correlation spectroscopy, J. Am. Ceram. Soc. 96 (2013) 2147–2154.

[30] D.L. Sidebottom, Fragility of network-forming glasses: A universal dependence on the topological connectivity, Phys. Rev. E - Stat. Nonlinear, Soft Matter Phys. 92 (2015) 1–9.

[31] D. Weitz, H. Wyss, R. Larsen, Oscillatory rheology: Measuring the viscoelastic behaviour of soft materials, GIT Lab. J. Eur. 11 (2007) 68–70.

[32] W. Zhu, M. Lockhart, B. Aitken, S. Sen, Dynamical rigidity transition in the viscoelastic properties of chalcogenide glass-forming liquids, J. Non. Cryst. Solids. 502 (2018) 244–248.

[33] F. Mallamace, M. Broccio, C. Corsaro, A. Faraone, U. Wanderlingh, L. Liu, C.Y. Mou, S.H. Chen, The fragile-to-strong dynamic crossover transition in confined water: Nuclear magnetic resonance results, J. Chem. Phys. 124 (2006) 161102.

[34] N. Kastelowitz, V. Molinero, Ice-liquid oscillations in nanoconfined water, ACS Nano. 12 (2018) 8234–8239.

[35] M. Vogel, NMR studies on simple liquids in confinement, Eur. Phys. J. Spec. Top. 189 (2010) 47–64.

[36] S.A. Lusceac, M.R. Vogel, C.R. Herbers, 2H and 13C NMR studies on the temperature-dependent water and protein dynamics in hydrated elastin, myoglobin and collagen, Biochim. Biophys. Acta. 1804 (2010) 41–48.

[37] I.C. Bourg, C.I. Steefel, Molecular dynamics simulations of water structure and diffusion in silica nanopores, J. Phys. Chem. C. 116 (2012) 11556–11564.

[38] A. Faraone, L. Liu, C.-Y. Mou, C.-W. Yen, S.-H. Chen, Fragile-to-strong liquid transition in deeply supercooled confined water, J. Chem. Phys. 121 (2004) 10843.

[39] L. Liu, S.-H. Chen, A. Faraone, C.-W. Yen, C.-Y. Mou, Pressure dependence of fragile-to-strong transition and a possible second critical point in supercooled confined water, Phys. Rev. Lett. 95 (2005) 117802.

[40] M. Vogel, Origins of apparent fragile-to-strong transitions of protein hydration waters, Phys. Rev. Lett. 101 (2008) 225701.

[41] S. Napolitano, E. Glynos, N.B. Tito, Glass Transition of Polymers in Bulk, Confined Geometries, and Near Interfaces, Rep. Prog. Phys. 80 (2017) 036602.

[42] V. Buch, J.P. Devlin, Water in confining geometries, Springer Science & Business Media, Berlin, 2013.

[43] A.A. Levchenko, P. Jain, O. Trofymluk, P. Yu, A. Navrotsky, S. Sen, Nature of molecular rotation in supercooled glycerol under nanoconfinement, J. Phys. Chem. B. 114 (2010) 3070–3074.

[44] S. Sen, S.H. Risbud, M.H. Bartl, Thermodynamic and Kinetic Transitions of Liquids in Nanoconfinement, Acc. Chem. Res. (2020).

[45] S. Sen, Y. Xia, W. Zhu, M. Lockhart, B. Aitken, Nature of the floppy-to-rigid transition in chalcogenide glass-forming liquids, J. Chem. Phys. 150 (2019) 144509.

[46] Y. Xia, W. Zhu, M. Lockhart, B. Aitken, S. Sen, Fragility and rheological behavior of metaphosphate liquids : Insights into their chain vs . network characters, J. Non. Cryst. Solids. 514 (2019) 77–82.

[47] Y. Xia, W. Zhu, J. Sen, S. Sen, Observation of polymer-like flow mechanism in a short-chain phosphate glass-forming liquid, J. Chem. Phys. 152 (2020).

[48] Y. Xia, H. Cho, M. Deo, S.H. Risbud, M.H. Bartl, S. Sen, Layer-by-Layer Freezing of Nanoconfined Water, Sci. Rep. 10 (2020) 5327.

[49] Y. Xia, H. Cho, S.H. Risbud, M.H. Bartl, S. Sen, Coexistence of Structural and Dynamical Heterogeneity in Liquids Under Nanoconfinement, Front. Phys. 8 (2020) 1–7.

Chapter 2

Nature of the Floppy-to-Rigid Transition in Chalcogenide Glass-Forming Liquids

2.1 Abstract

The viscoelastic properties of supercooled As_xSe_{100-x} and Ge_xSe_{100-x} ($0 \leq x \leq 30$) liquids are studied using oscillatory parallel plate rheometry. The liquids with average selenium chain segment length L longer than ~ 3 to 5 atoms or average coordination number <r> less than ~ 2.2 are characterized by the coexistence of a low-frequency bond scission/renewal-based relaxation process as well as high-frequency segmental chain dynamics. The latter process disappears for liquids with higher connectivity, thus implying a dynamical rigidity transition. The temporal decoupling of the high-frequency chain mode from that of the bond scission/renewal process as well as the shear modulus G_s associated with the low-frequency mode are shown to be unique functions of L or <r> and display strong similarity with the corresponding variation in the fragility m and the conformational entropy of the chain segments. When taken together, these results provide direct experimental support to the entropic rigidity argument originally proposed by Phillips [1], but suggest a floppy-to-rigid transition of the structural network at <r> ~ 2.2, instead of the conventional rigidity percolation threshold value of 2.4.

2.2 Introduction

The average connectivity of a random network controls its rigidity. Phillips and Thorpe were the first to point out that a random network undergoes a floppy-to-rigid transition when the average coordination number of the network <r> = 2.4 [1-4]. The original argument of Phillips [1] was based on the entropic contribution from the deformation of a network, which becomes negligible as the network becomes rigid and over-constrained with increasing connectivity or <r>. Thorpe argued entropy to be an "imprecise" measure of rigidity and related the latter to the number of zero-frequency modes available for a continuous deformation of the network without any significant energy penalty [2]. The fraction of these modes f becomes non-zero and increases rapidly as <r> decreases below the threshold value of 2.4, while $f = 0$ when <r> increases beyond 2.4 [2-4]. Since this transition in the behavior of f vs. <r> is rather sharp across the rigidity percolation threshold, substantial effort has been made over the last decades to understand how such a transition could be manifested in the physical properties of amorphous networks where the connectivity can be varied continuously over a wide range and across <r> = 2.4. In this regard, chalcogenide glassy networks are of significant interest as these materials, being characterized by energetically similar covalent bonds and by a wide range of network connectivity, provide model systems for studying the effects of rigidity percolation on various physical properties.

The rigidity percolation model is attractive in the sense that it hints at the possibility of the existence of an underlying universal behavior in the compositional variation of at least some physical properties of glasses irrespective of their chemical details. Nevertheless, a clear observation of the cause and effect relationship between rigidity percolation and the physical properties of glasses has remained elusive, even in chalcogenides [5-8]. However, several studies in the literature have reported a sharp change across <r> ~ 2.4 in the temperature dependence of

the viscous flow of a wide variety of glass-forming chalcogenide and phosphate liquids near the glass transition temperature T_g, as expressed by the fragility index $m = \frac{d\log_{10}\eta}{d(\frac{T_g}{T})}|_{T=T_g}$, where η is the viscosity [9-11]. For example, chalcogenide liquids with a chain-like structure, such as elemental Se, are characterized by <r> =2 and a rather high fragility index of $m \sim 80$. Addition of Ge and/or As leads to shortening of the Se chains and their cross-linking via $GeSe_{4/2}$ tetrahedra or $AsSe_{3/2}$ pyramids, which results in a progressive increase in <r>. As <r> increases from 2 and approaches 2.4, *m* rapidly decreases to ~ 30, beyond which further increase in <r> up to the point of the stochiometric compositions $GeSe_2$ or As_2Se_3 results in negligible change in *m*. In a previous study Sidebottom has shown such a variation in *m* vs. <r> to hold for more than 150 different network liquids including chalcogenides and phosphates [11].

It must be noted that the Phillips-Thorpe model of rigidity percolation is related to the Maxwell criterion of the mechanical stability or deformability of a network and, thus, it is strictly a model without any explicit temperature dependence [12]. Therefore, an apparently universal pattern of *m* vs. <r> with a relatively sharp transition in their relationship across <r> ~ 2.4 is not intuitively obvious, but implies a deep link between the average connectivity of a network and its fragility. Further insight into this problem can be gained from the consideration of an approximate but insightful model recently proposed by Sidebottom [11] that is based on a combination of the Adam-Gibbs configurational entropy model of relaxation and the self-avoiding walk (SAW) model of the conformational entropy of a polymer chain. According to the Adam-Gibbs model of structural relaxation, the temperature dependence of the viscosity η of a liquid depends on its configurational entropy $S_c(T)$ as $\log \eta = A + B/TS_c$, where *A* and *B* are material constants [13]. Hence, *m* of a liquid by definition is proportional to $\frac{dS_c}{dT}|_{T \to Tg} = \left(\frac{dS_c}{d<r>}\right)\left(\frac{d<r>}{dT}\right)|_{T \to Tg}$. The first term

in this product is a measure of the change in configurational entropy with the average connectivity of a network and the second term corresponds to the temperature dependence of the average connectivity of the network. Sidebottom used the thermodynamics of a two-level system of broken vs. intact bonds to show that $\left(\frac{d<r>}{dT}\right) \propto \left(\frac{dS_c}{d<r>}\right)$ and hence, $m \propto \left(\frac{dS_c}{d<r>}\right)^2$. Finally, the quantity $\left(\frac{dS_c}{d<r>}\right)$ and, hence, *m* was estimated for a polymer chain performing a SAW, via a calculation of the variation in the number of its possible conformations with progressive increase in the crosslink density, to show that the variation in *m* with <r> indeed mimics the experimentally observed pattern. However, the change in entropy with increasing crosslinking was observed to become rather small at <r> = 2.2 and to vanish at <r> = 2.3. These average connectivities are significantly different from <r> = 2.4, corresponding to the appearance of the floppy modes in Thorpe's model.

In a recent study Zhu *et al.* have reported the viscoelastic properties of supercooled As_xSe_{100-x} ($0 \leq x \leq 30$) and $As_xSe_{100-x-y}I_y$ (x =20, 30 and y=10, 20) liquids [14]. The results of this study indicated the coexistence of a fast and a slow relaxation mode in these liquids with average selenium chain lengths of more than three Se atoms. The temporal decoupling between these two relaxation modes was found to be a unique function of the chain length. One of these relaxation modes abruptly disappears in liquids with shorter chain lengths or higher degree of crosslinking, which then behave as simple liquids with a single α-relaxation timescale. This relatively abrupt transition in the shear relaxation behavior of these liquids as a function of the average selenium chain length was argued to be a manifestation of rigidity percolation. In this chapter, I extend such studies to Ge_xSe_{100-x} ($0 \leq x \leq 22.5$) liquids, as well as to a more extensive set of compositions in the As_xSe_{100-x} ($0 \leq x \leq 30$) system, to demonstrate the existence of a remarkably universal relationship

in these chalcogenide systems between <r> and their viscoelastic behavior. The implications of these results are discussed within the context of rigidity percolation.

2.3 Experimental Methods

2.3.1 Sample synthesis

The Ge_xSe_{100-x} ($0 \leq x \leq 22.5$) and As_xSe_{100-x} ($0 \leq x \leq 30$) glasses were synthesized from the constituent elements (≥99.999% purity, metal basis) that were melted in evacuated (10^{-6} Torr) and flame sealed fused silica ampoules (8 mm inside diameter, 12 mm outside diameter) in a rocking furnace at temperatures that, depending on composition, ranged between 700 and 1100 K, for at least 24 h. Finally, the melts were quenched by dipping the ampoule in water to form glasses.

2.3.2 Parallel plate rheometry

The rheological spectra of all compositions were measured by oscillatory parallel plate rheometry, using two rheometers: MCR 92 (Anton Paar) and ARES G2 (TA Instruments). The temperature control was achieved by either a surrounding Peltier heater (MCR 92) or a forced convection oven (ARES G2), under a flowing nitrogen gas environment. Both rheometers were operated under oscillatory mode with an 8 mm plate and a gap of ~ 1 mm. In these rheometers, sinusoidal strain at desired angular frequency ω is applied and the corresponding stress response is obtained via the measurement of the torque, which allows the determination of the storage shear modulus G′, loss shear modulus G", and viscosity η as a function of ω. Before the rheometry measurements, all samples were heated above their softening point, pressed and then trimmed to form a sandwich-like geometry between the plates. During each measurement, the samples were allowed to equilibrate at each temperature for 5 minutes before the application of oscillating strain,

which was controlled within a predetermined linear viscoelastic region. Multiple measurements covering a frequency range of 1 to 600 rad/s were carried out at various temperatures for each sample and master curves of G′(ω) and G"(ω) were constructed using time-temperature superposition (TTS).

2.4 Results and Discussion

The master curves of G′(ω) and of G"(ω) for all As_xSe_{100-x} and Ge_xSe_{100-x} glass-forming liquids investigated in this chapter are shown in Figs. 2-1 and 2-2. TTS for each system is carried out at iso-viscous temperatures corresponding to ~10^6 Pa.s (~10^8 Pa.s) for the As-Se (Ge-Se) liquids. It can be readily observed that G′(ω) < G"(ω) in the low-frequency, viscous regime and these quantities approximately follow the Maxwell scaling of ~ ω^n, where $n \approx 2$ and 1 for G′ and G", respectively. On the other hand, in the high-frequency elastic regime, G′(ω) > G"(ω) and G′(ω) approaches its glassy limit G_∞, while G"(ω) decreases with increasing frequency. The corresponding viscosity spectrum $\eta(\omega) = \frac{\sqrt{G'^2+G''^2}}{\omega}$ shows a transition from a frequency-independent behavior at the lowest frequencies to a frequency-dependent behavior at higher frequencies. The region between these two regimes, for As_xSe_{100-x} liquids with $x \leq 15$ and for Ge_xSe_{100-x} liquids with $x \leq 7.5$, is marked by two crossovers between G′(ω) and G"(ω) and, correspondingly, two transitions in the frequency dependence of $\eta(\omega)$, which suggest the presence of two relaxation processes with characteristic frequencies marked by the locations of the two crossovers (Figs. 2-1, 2-2). Each G′- G" crossover is associated with a G′ plateau corresponding to the shear modulus for the relaxation process. The timescales for the slow and fast processes are

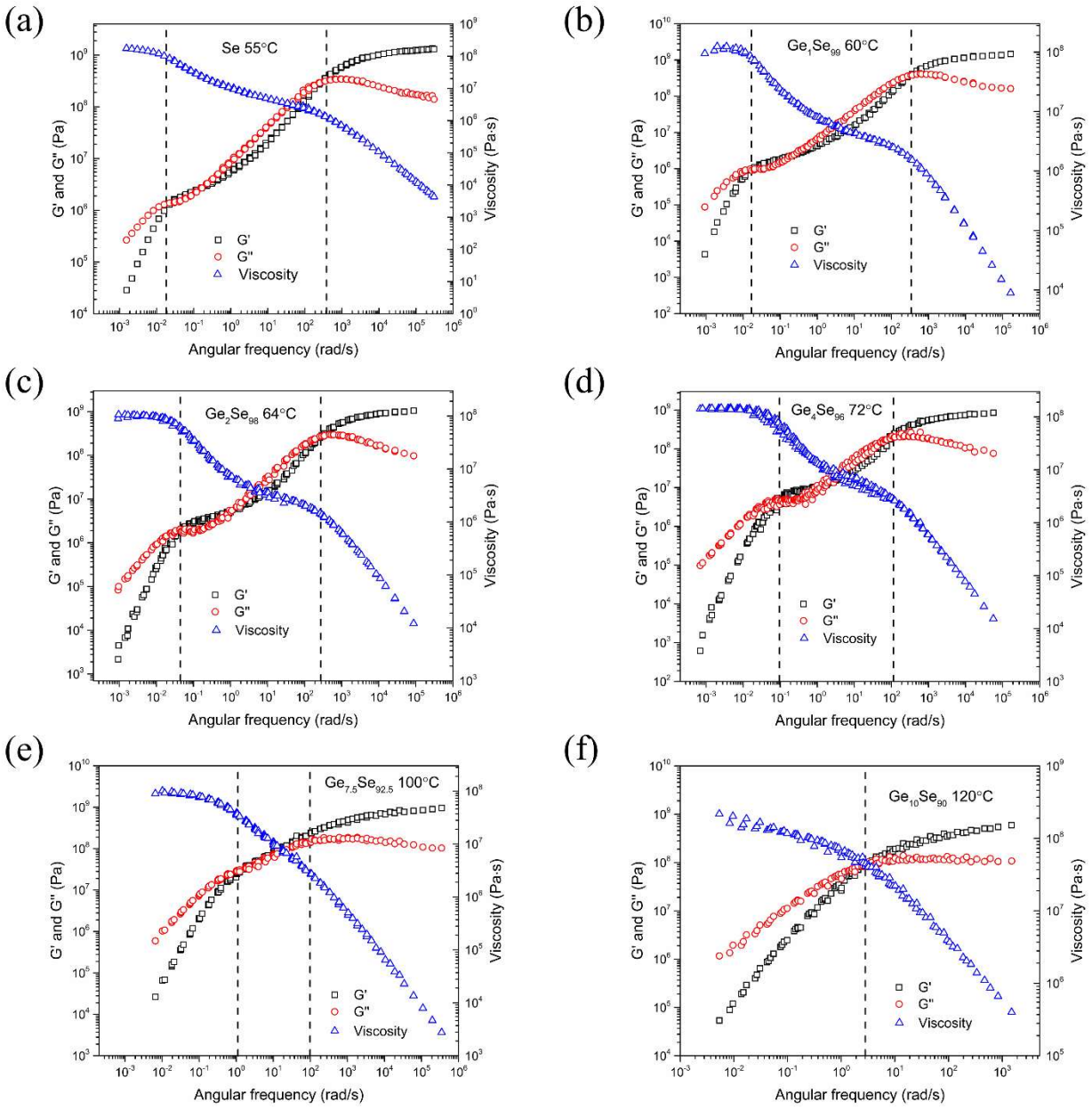
(a)
Se 55°C
(b)
Ge1Se99 60°C
(c)
Ge2Se98 64°C
(d)
Ge4Se96 72°C
(e)
Ge7.5Se92.5 100°C
(f)
Ge10Se90 120°C
G' and G'' (Pa)
Viscosity (Pa·s)
Angular frequency (rad/s)
G'
G''
Viscosity

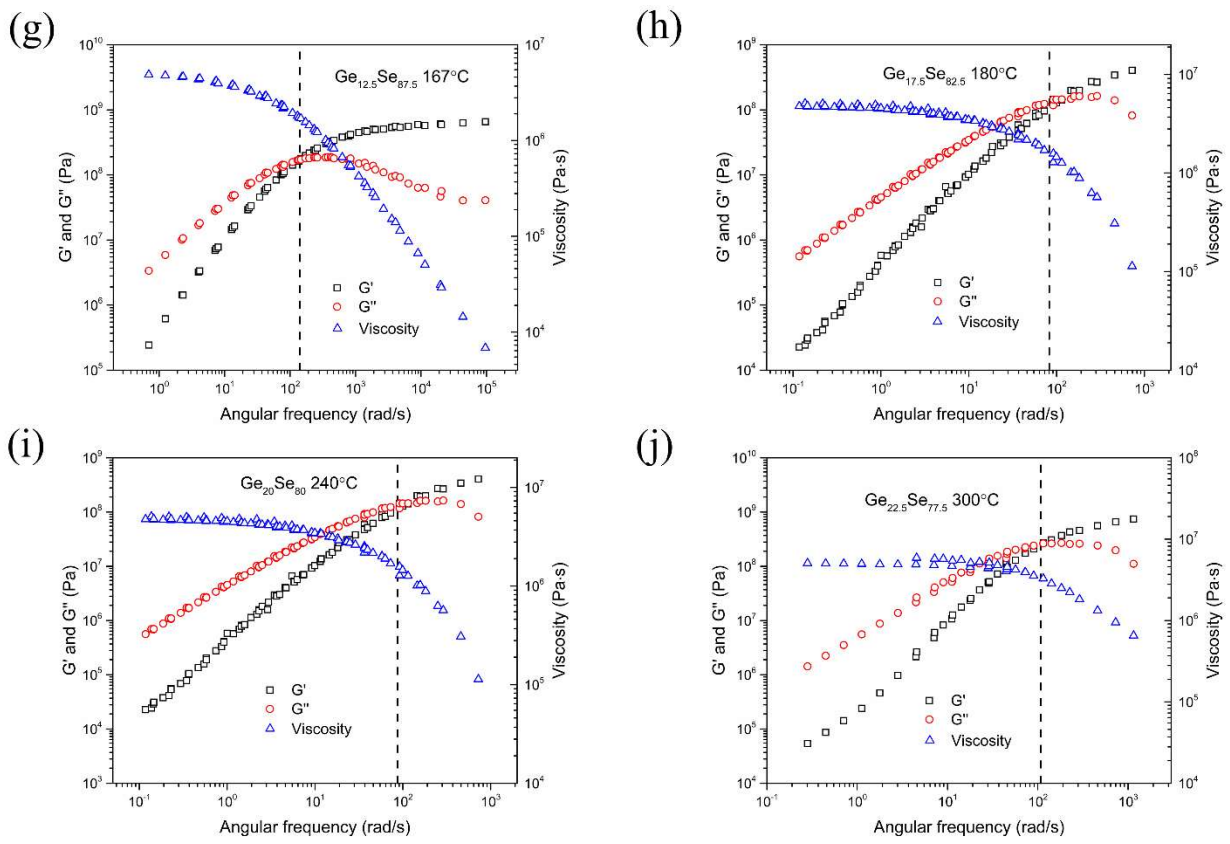

Figure 2-1 Master curves of storage modulus G' (black squares), loss modulus G" (red circles) and viscosity (blue triangles) spectra of Se and Ge_xSe_{100-x} liquids. The TTS reference temperature is listed alongside each composition. Locations of G'- G" crossovers are marked by dashed vertical lines.

(a)

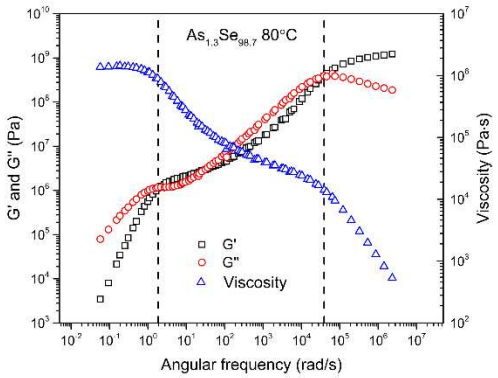
As1.3Se98.7 80°C
G' and G'' (Pa)
Viscosity (Pa·s)
Angular frequency (rad/s)
G'
G''
Viscosity

(b)

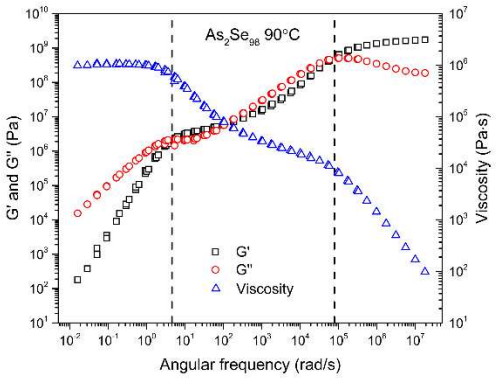
As2Se98 90°C
G' and G'' (Pa)
Viscosity (Pa·s)
Angular frequency (rad/s)
G'
G''
Viscosity

(c)

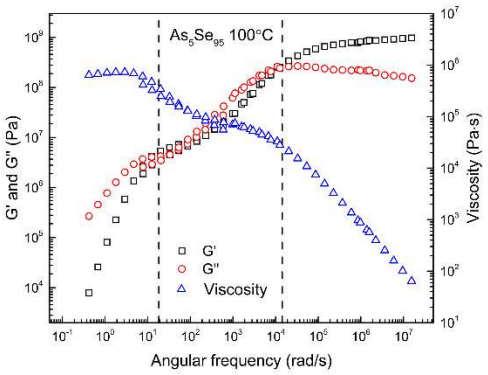
As5Se95 100°C
G' and G'' (Pa)
Viscosity (Pa·s)
Angular frequency (rad/s)
G'
G''
Viscosity

(d)

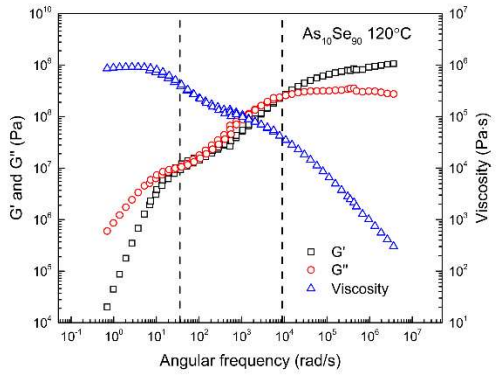
As10Se90 120°C
G' and G'' (Pa)
Viscosity (Pa·s)
Angular frequency (rad/s)
G'
G''
Viscosity

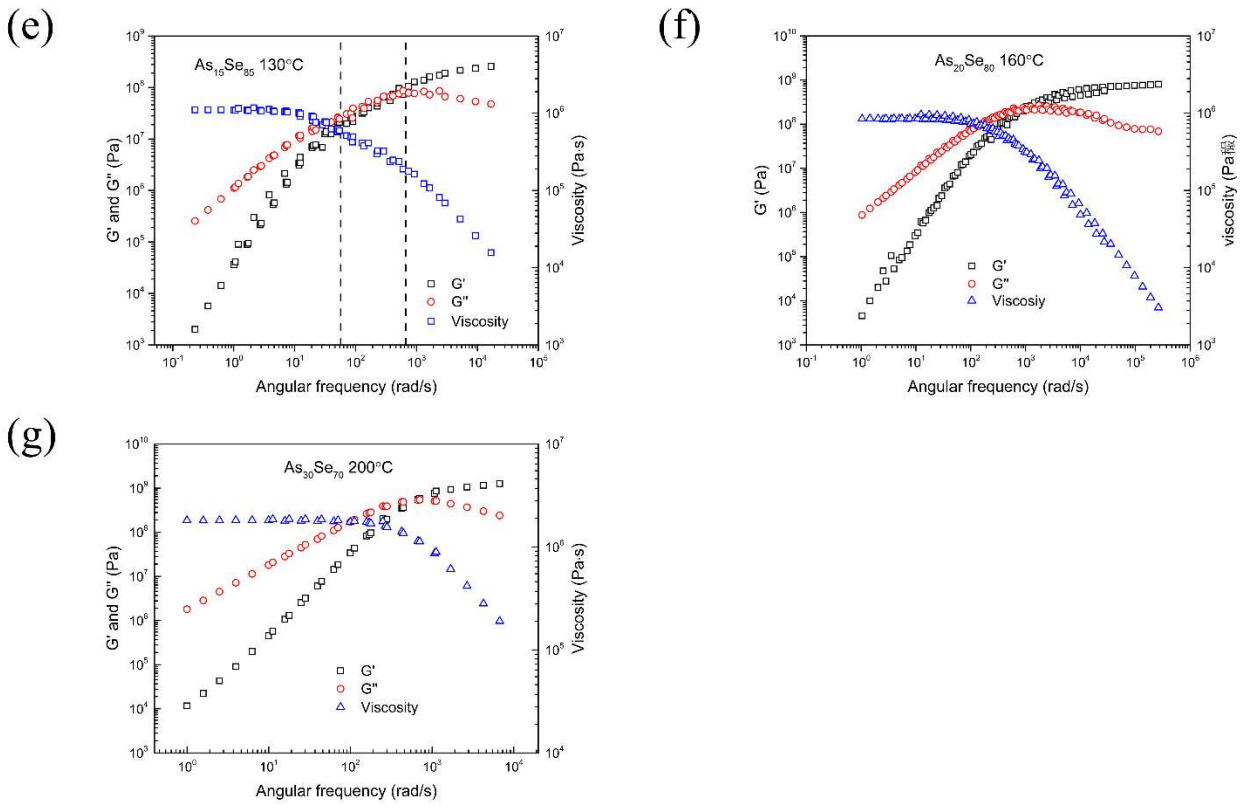

Figure 2-2 Master curves of storage modulus G' (black squares), loss modulus G" (red circles) and viscosity (blue triangles) spectra of Se and As_xSe_{100-x} liquids. The TTS reference temperature is listed alongside each composition. Locations of G'- G" crossovers are marked by dashed vertical lines.

denoted τ_s and τ_f, and the corresponding moduli G_s and G_f, in the subsequent discussion. A recent study of the temperature dependence of τ_s and τ_f in supercooled selenium liquid has enabled an unequivocal assignment of the slow and fast processes to the bond scission/renewal dynamics and the local segmental motion of selenium chain moieties, respectively [15]. This study also demonstrated that the slow process is coupled to viscous flow at all temperatures i.e. $\eta \approx \tau_s * G_s$, while the fast process becomes a major contributor to viscosity only near T_g. The decoupling of the fast process from viscous flow at high temperatures was also observed in a previous high-temperature ^{77}Se NMR study of supercooled Ge-Se liquids [16], which indicated that the timescale

of selenium chain motion was nearly two orders of magnitude faster than the shear relaxation timescale at T_g/T ~ 0.85.

In contrast with this multi-timescale relaxation behavior of liquids with relatively high Se content, Ge_xSe_{100-x} liquids with x ≥10 and As_xSe_{100-x} liquids with x ≥20 display a single and sharp G′-G" crossing (Figs. 2-1, 2-2), characteristic of simple network liquids with a single α-relaxation timescale [17-20]. It is well known that the progressive addition of Ge or As to Se results in increasing crosslinking of the selenium chains via $GeSe_{4/2}$ tetrahedra or $AsSe_{3/2}$ pyramids, and a rapid decrease in the average length L of the selenium chain segments, expressed in terms of the number of Se atoms between these crosslinking points. The corresponding changes in the viscoelastic behavior of these liquids with increasing Ge or As content, as shown in Figs. 2-1 and 2-2, include: (i) a progressive decrease in the separation of the timescales of the two relaxation processes i.e. ($\tau_s - \tau_f$), as τ_s becomes progressively shorter, (ii) an increase in G_s at an iso-viscous temperature, and (iii) the disappearance of the fast relaxation mode as x increases beyond ~ 10-15 atom% (Figs. 2-1, 2-2). As the fast relaxation mode disappears, the network relaxation is entirely controlled by the bond scission/renewal dynamics at all temperatures. This hypothesis is consistent with the results obtained in previous studies of the aging dynamics of $Ge_{20}Se_{80}$ and $Si_{25}Se_{75}$ glasses [21,22], which indicated that the activation energy and the timescale of shear relaxation in these glasses near T_g were similar to those of the conversion reaction between the edge- and the corner- shared $(Ge,Si)Se_{4/2}$ tetrahedra that must involve bond scission and renewal.

The separation Δ between the logarithm of the frequencies of the bond scission/renewal and the segmental chain dynamics, i.e. ($\log \tau_s^{-1} - \log \tau_f^{-1}$), is a measure of the degree of coupling between these two relaxation processes. The compositional variation of Δ for both Ge-Se and As-

Se liquids is shown in Fig. 2-3 as a function of L and <r> and compared with the corresponding variation in m. Here L is calculated on the basis of the Flory model of polymerization, which was shown by ^{77}Se NMR spectroscopic measurements to be approximately obeyed by the glasses in the Ge-Se and As-Se systems, and the Se atoms directly bonded to the Ge or As atoms are included in the evaluation of L [23-25]. L for pure Se is taken to be 200, in accordance with recent estimates reported in the literature [14,26]. It is clear from Fig. 2-2 that Δ is the largest in pure selenium liquid where the timescale of the segmental chain motion is nearly 4 orders of magnitude faster than that of the bond scission/renewal timescale, i.e. these selenium chains are "persistent" in the sense that they undergo many conformational changes before breaking and reforming. Progressive crosslinking of these chains with $GeSe_{4/2}$ tetrahedra or $AsSe_{3/2}$ pyramids results in a decrease in L and in a loss in their conformational flexibility or "floppiness". As a consequence, the coupling between the local high-frequency chain motion and the low-frequency conformational change associated with bond scission/renewal increases and Δ decreases. As L approaches a value of ~ 3-5, these selenium chains become too short to perform segmental dynamics and only bond scission/renewal is observed. Consequently, $\Delta = 0$ for both Ge_xSe_{100-x} and As_xSe_{100-x} systems as <r> approaches a value of ~ 2.2 (Fig. 2-2). The conformational entropy of a progressively cross-linked chain has also been shown to nearly vanish at this point [11].

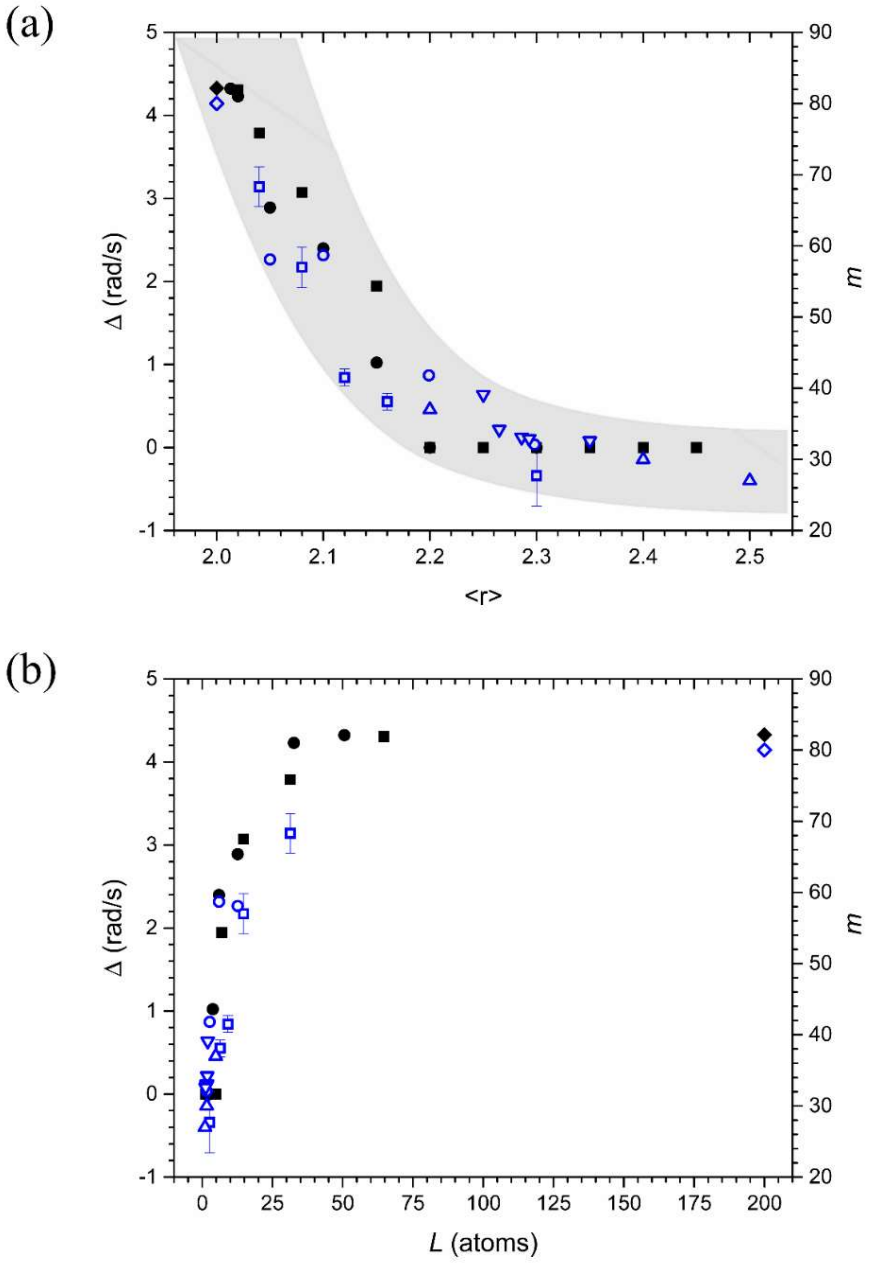

Figure 2-3 Temporal decoupling parameter Δ (filled symbols) and fragility *m* (open symbols) of Ge_xSe_{100-x} and As_xSe_{100-x} liquids as a function of (a) average coordination number <r>, and (b) average length of selenium chain segments *L*. For Δ, the filled circles and squares correspond to As-Se and Ge-Se liquids, respectively, while filled diamond represents the data point for pure Se. For Ge-Se liquids: open squares correspond to *m* determined from viscosity [28] and open triangles represent *m* determined by calorimetry [29]. For As-Se liquids *m* is obtained from viscosity: open circles and inverted triangles correspond to data from [26] and [30], respectively, while filled triangles are from [32]. The *m* for pure Se is shown by the open diamond symbol, as obtained from the viscosity data reported by [31]. The shaded band is a guide to the eyes.

Plazek and Frund have argued that the steady-state recoverable compliance J_s in chain polymers marks the point where the molecules have reached their limiting conformational change per unit stress and, thus, the difference between J_s and the glassy compliance J_g is a measure of the change in conformational entropy from the elastic (glassy) to the viscous state [27]. This change in the conformational entropy is simply a measure of the fragility of a glass-forming liquid. Thus, J_g being nearly constant, a decrease in m should correspond to a lowering of J_s. It may be noted that J_s and J_g are, respectively, the reciprocals of G_s and G_f as defined in the present study. The compositional variation in G_s, as observed in the present study, is indeed in agreement with the compositional dependence of the steady state recoverable creep compliance J_s in As-Se liquids at comparable temperatures, as reported in a previous study by Bernatz *et al*. [26]. Therefore, G_s should show a trend with L or <r> that is inverse of that of m. This expectation is indeed borne out in Fig. 2-4. With increasing Ge or As concentration and cross-linking of the Se chains, the onset of a rapid decrease in G_s and a concomitant rise in m are observed as <r> becomes ≤ 2.2 (Fig. 2-4). To the best of my knowledge, this is the first direct observation of a floppy-to-rigid transformation of the shear modulus of a network as a function of its connectivity. Although Thorpe's model [2-4] conjectured the existence of such a manifestation of rigidity percolation in the elastic properties of a network, previous studies focused on the compositional variation of the high-frequency "glassy" shear modulus G_f of chalcogenide networks, which shows only a small variation with <r> [5,6]. On the other hand, the low-frequency modulus G_s indeed displays a rigid to floppy transition across <r> ≈ 2.2. However, it must be noted that G_s is not a purely elastic modulus but rather provides a measure of the conformational entropy of selenium chain elements as they are progressively cross-linked. To further test this hypothesis, the SAW model proposed

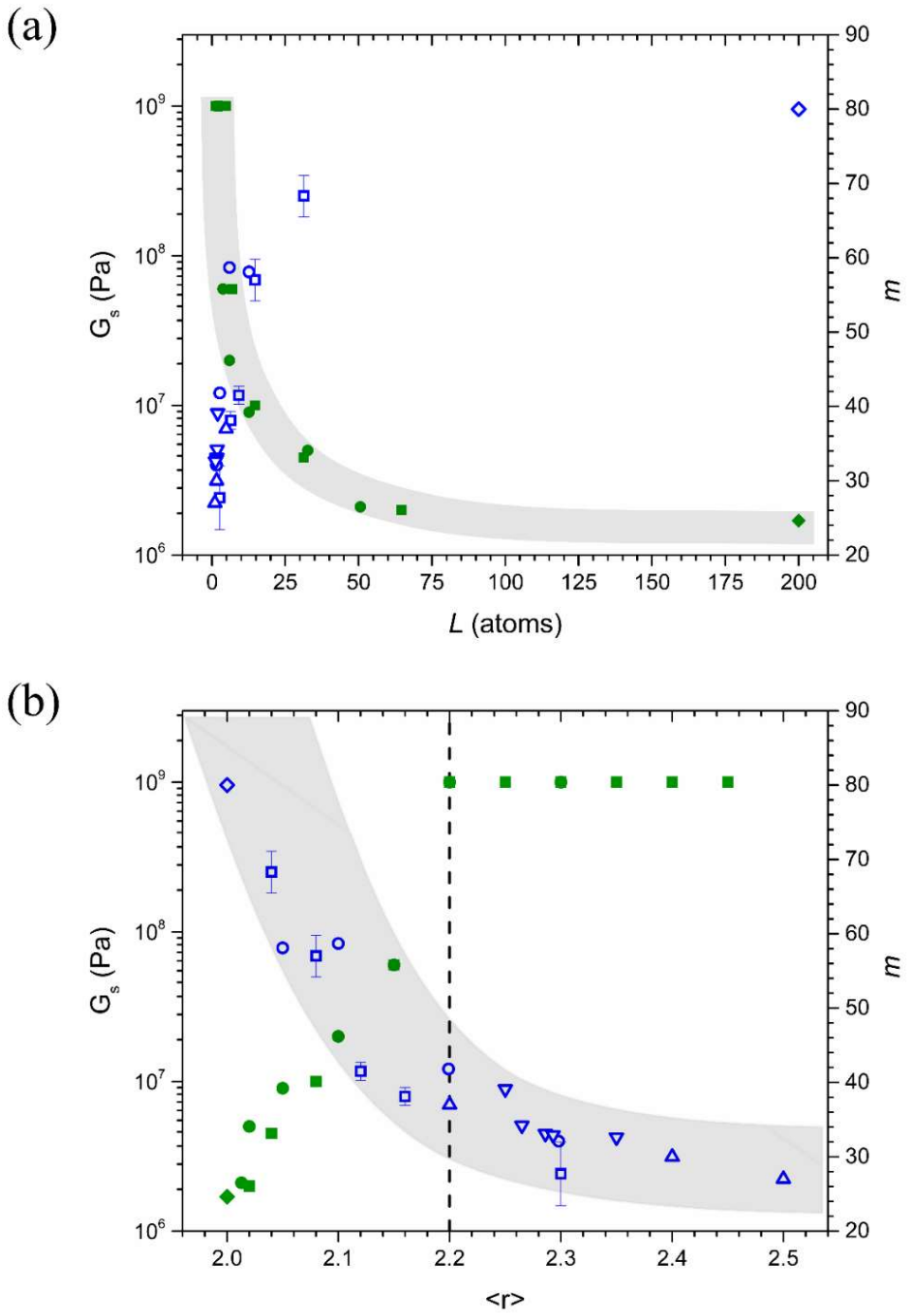

Figure 2-4 Shear modulus G_s (filled symbols) and fragility m (open symbols) of Ge_xSe_{100-x} and As_xSe_{100-x} liquids as a function of (a) average length of selenium chain segments L, and (b) average coordination number <r>. For G_s, the filled circles and squares correspond to As-Se and Ge-Se liquids, respectively, while filled diamond represents the data point for pure Se. For m all symbols have the same meaning as in Fig. 2-3. The shaded band is a guide to the eyes.

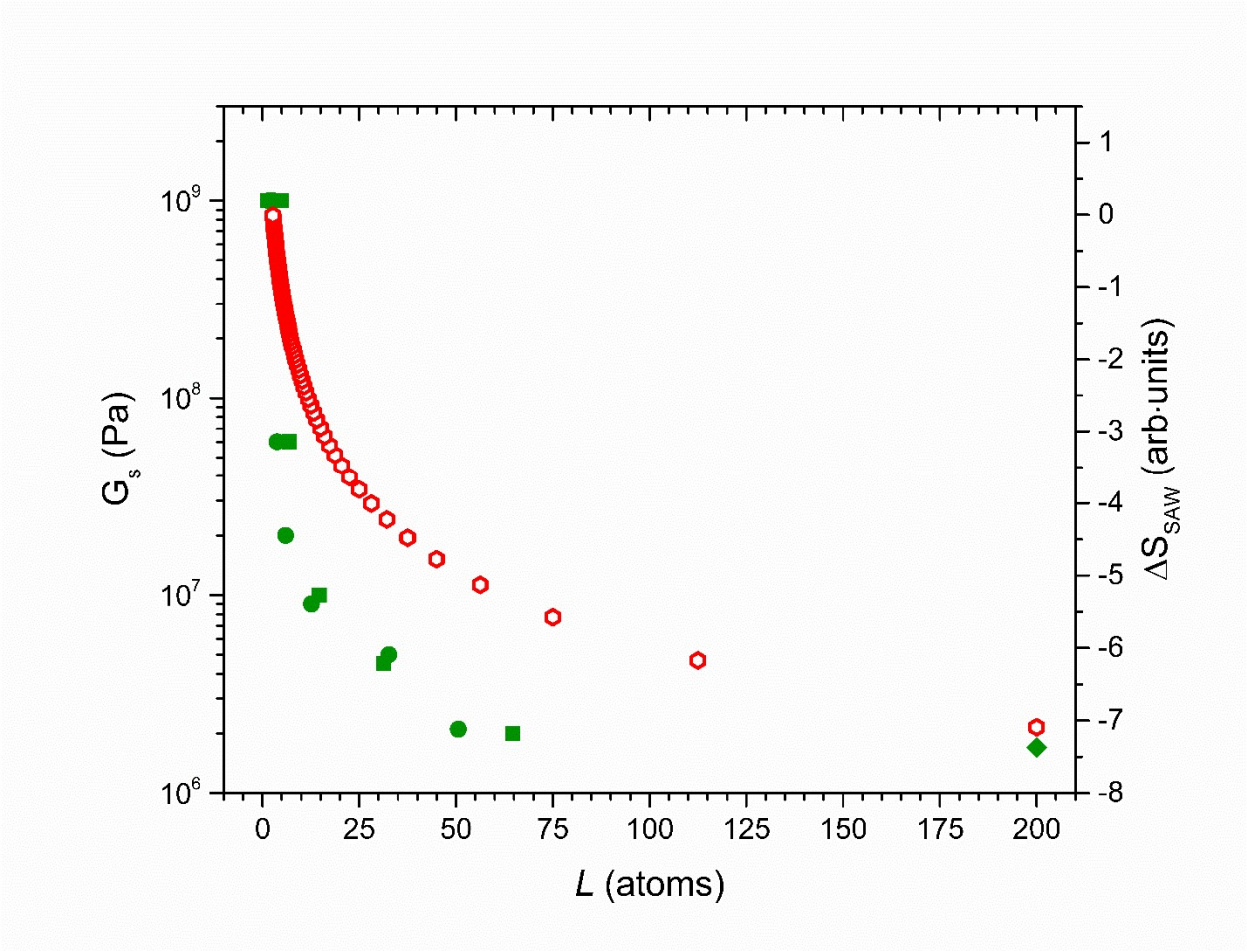

Figure 2-5 Shear modulus G_s (filled symbols) of Ge_xSe_{100-x} (filled squares) and As_xSe_{100-x} (filled circles) liquids and conformational entropy ΔS_{SAW} (open symbols) estimated from the SAW model (see text for details) as a function of average length of selenium chain segments L.

by Sidebottom [11] is used to estimate the change in the conformational entropy ΔS_{SAW} of a chain of N monomers, upon progressive addition of $j-1$ crosslinks, as a function of the length L of the chain segments in between consecutive crosslinks, where $L = 200/j$. Here we have used a simplified expression for ΔS_{SAW} given by: $\Delta S_{SAW} = -j\delta ln\left(\frac{j}{j+1}\right) - \delta ln\left(\frac{N}{j+1}\right)$, where $\delta \approx 1.76$ for SAW in three dimensions and N is taken to be 200. Although, as noted by Sidebottom [11], this expression is only approximate and may cease to be valid as L becomes small, a comparison between the variations of G_s and ΔS_{SAW} *vs.* L (Fig. 2-5) reveals intriguing similarity, thus providing

support to the abovementioned hypothesis. These results, when taken together, suggest that as L approaches a value between ~3 and 5, and correspondingly $\langle r \rangle \approx 2.2$, the network becomes rigid as the short selenium chain segments cannot generate significant entropy via conformation change. Therefore, I argue that Phillips' original proposal [1] of the floppy-to-rigid transition of a network based on an entropic definition of rigidity is "precise" and consistent with the experimental results reported in this study.

2.5 Conclusion

The viscoelastic properties of supercooled As_xSe_{100-x} and Ge_xSe_{100-x} liquids show universal patterns of variation as a function of L or $\langle r \rangle$. The abrupt appearance of the "floppy" high-frequency dynamics of selenium chain segments, as $\langle r \rangle$ decreases below 2.2, coincides with the rapid drop in the low-frequency shear modulus G_s corresponding to the primary relaxation via bond scission/renewal process, as well as the abrupt increase in the fragility m of these liquids. The shear modulus G_s is shown to be a measure of the conformational entropy of the chain elements. These results directly support the entropic rigidity hypothesis proposed by Phillips [1], which argues that the floppy-to-rigid transition of a network should coincide with the disappearance of the entropic contribution from the deformation of the network. However, this transition is observed at $\langle r \rangle \sim 2.2$, and not at the widely quoted value of 2.4, derived from the consideration of constraint counting and the Maxwell stability criterion [2-4].

References

[1] J.C. Phillips, Topology of covalent non-crystalline solids: Short-range order in chalcogenide alloys, J. Non. Cryst. Solids. 34 (1979) 153–181.

[2] M.F. Thorpe, Continuous deformations in random networks, J. Non. Cryst. Solids. 57 (1983) 355–370.

[3] H. He, M.F. Thorpe, Elastic properties of glasses, Phys. Rev. Lett. 54 (1985) 2107–2110.

[4] M.F. Thorpe, D.J. Jacobs, N.B. Chubynsky, A.J. Rader, Generic rigidity of networks glasses, in: M.F. Thorpe, P.M. Duxbury (Eds.), Rigidity Theory Appl., Kluwer Academic/Plenum, New York, 1999: pp. 239–277.

[5] G. Yang, Y. Gueguen, J.C. Sangleboeuf, T. Rouxel, C. Boussard-Plédel, J. Troles, P. Lucas, B. Bureau, Physical properties of the Ge_xSe_{1-x} glasses in the correlation with their structure, J. Non. Cryst. Solids. 377 (2013) 54–59.

[6] T. Wang, O. Gulbiten, R. Wang, Z. Yang, A. Smith, B. Luther-Davies, P. Lucas, Relative contribution of stoichiometry and mean coordination to the fragility of Ge-As-Se glass forming liquids, J. Phys. Chem. B. 118 (2014) 1436–1442.

[7] G. Yang, B. Bureau, T. Rouxel, Y. Gueguen, O. Gulbiten, C. Roiland, E. Soignard, J.L. Yarger, J. Troles, J.C. Sangleboeuf, P. Lucas, Correlation between structure and physical properties of chalcogenide glasses in the As_xSe_{1-x} system, Phys. Rev. B. 82 (2010) 195206.

[8] K. Tanaka, Structural phase transitions in chalcogenide glasses, Phys. Rev. B. 39 (1989) 1270–1279.

[9] D.L. Sidebottom, T.D. Tran, S.E. Schnell, Building up a weaker network: The effect of intermediate range glass structure on liquid fragility, J. Non. Cryst. Solids. 402 (2014) 16–20.

[10] D.L. Sidebottom, D. Vu, Assessing the network connectivity of modifier ions in metaphosphate glass melts : A dynamic light scattering study of Na-Zn mixtures, J. Chem. Phys. 145 (2016) 164503.

[11] D.L. Sidebottom, Fragility of network-forming glasses: A universal dependence on the topological connectivity, Phys. Rev. E - Stat. Nonlinear, Soft Matter Phys. 92 (2015) 1–9.

[12] J.C. Mauro, Topological constraint theory of glass, Am. Ceram. Soc. Bull. 90 (2011) 31–37.

[13] G. Adam, J.H. Gibbs, On the temperature dependence of cooperative relaxation properties in glass-forming liquids, J. Chem. Phys. 43 (1965) 139–146.

[14] W. Zhu, M. Lockhart, B. Aitken, S. Sen, Dynamical rigidity transition in the viscoelastic properties of chalcogenide glass-forming liquids, J. Non. Cryst. Solids. 502 (2018) 244–248.

[15] W. Zhu, B.G. Aitken, S. Sen, Observation of a dynamical crossover in the shear relaxation processes in supercooled selenium near the glass transition, J. Chem. Phys. 150 (2019) 094502.

[16] E.L. Gjersing, S. Sen, R.E. Youngman, Mechanistic understanding of the effect of rigidity percolation on structural relaxation in supercooled germanium selenide liquids, Phys. Rev. B. 82 (2010) 014203.

[17] J.J. Mills, Low frequency storage and loss moduli of soda-silica glasses in the transfoilmation range, J. Non. Cryst. Solids. 14 (1974) 255–268.

[18] J. Tauke, T.A. Litovitz, P.B. Macedo, Viscous relaxation and non-Arrhenius behavior in B_2O_3, J. Am. Ceram. Soc. 51 (1968) 158–163.

[19] R.L. Sammler, J.U. Otaigbe, M.L. Lapham, N.L. Bradley, B.C. Monahan, C.J. Quinn, Melt rheology of zinc alkali phosphate glasses, J. Rheol. (N. Y. N. Y). 40 (1996) 285.

[20] W. Zhu, M.J. Lockhart, B.G. Aitken, S. Sen, Rheology of the λ transition in liquid sulfur: Insights from arsenic sulfide liquids, J. Chem. Phys. 148 (2018) 244506.

[21] T.G. Edwards, S. Sen, Structure and relaxation in germanium selenide glasses and supercooled liquids: A raman spectroscopic study, J. Phys. Chem. B. 115 (2011) 4307–4314.

[22] M.A.T. Marple, V. Yong, S. Sen, Fragility and aging behavior of Si_xSe_{1-x} glasses and liquids, J. Chem. Phys. 150 (2019) 044506.

[23] P.J. Flory, Molecular size distribution in linear condensation polymers, J. Am. Chem. Soc. 58 (1936) 1877–1885.

[24] D.C. Kaseman, K.M. Oliveira, T. Palazzo, S. Sen, Selenium chain length distribution in Ge_xSe_{100-x} Glasses: Insights from ^{77}Se NMR spectroscopy and quantum chemical calculations, J. Phys. Chem. B. 120 (2016) 4513–4521.

[25] M. Deschamps, C. Genevois, S. Cui, C. Roiland, L. Lepollès, E. Furet, D. Massiot, B. Bureau, Structure of arsenic selenide glasses studied by NMR: Selenium chain length distributions and the flory model, J. Phys. Chem. C. 119 (2015) 11852–11857.

[26] K.M. Bernatz, I. Echeverría, S.L. Simon, D.J. Plazek, Characterization of the molecular structure of amorphous selenium using recoverable creep compliance measurements, J. Non. Cryst. Solids. 307 (2002) 790–801.

[27] D.J. Plazek, Z.N. Frund, Recoverable creep compliance properties of associative model polymer and polyoxyethylene solutions, J. Rheol. (N. Y. N. Y). 44 (2000) 929–946.

[28] Y. Gueguen, T. Rouxel, P. Gadaud, C. Bernard, V. Keryvin, J.C. Sangleboeuf, High-temperature elasticity and viscosity of Ge_xSe_{1-x} glasses in the transition range, Phys. Rev. B. 84 (2011) 064201.

[29] R. Svoboda, J. Málek, Kinetic fragility of Se-based binary chalcogenide glasses, J. Non. Cryst. Solids. 419 (2015) 39–44.

[30] S. V. Nemilov, G.T. Petrovskii, A study of the viscosity of selenium-arsenic glasses, Zn. Prikl. Khim. 36 (1963) 977–981.

[31] P. Koštál, J. Málek, Viscosity of selenium melt, J. Non. Cryst. Solids. 356 (2010) 2803–2806.

[32] J.D. Musgraves, P. Wachtel, S. Novak, J. Wilkinson, K. Richardson, Composition dependence of the viscosity and other physical properties in the arsenic selenide glass system, J. Appl. Phys. 110 (2011) 063503.

Chapter 3

Fragility and Rheological Behavior of Metaphosphate Liquids: Insights into their Chain vs. Network Characters

3.1 Abstract

The viscosity and the shear relaxation behavior of supercooled Ag- and Sn-metaphosphate liquids are measured using parallel plate techniques. The fragility index *m* of these liquids, when taken together with that of other metaphosphate liquids, shows variation over a rather large range spanning from ~ 30 to 90 and is found to be a sensitive function of the strength and extent of connectivity or coupling between the phosphate chains provided by the modifier-oxygen coordination polyhedra. The high fragility of the Ag-metaphosphate liquid ($m \approx 90$) is a result of the weak inter-chain coupling which is manifested in a polymer-like rheological behavior that is in contrast with the network-liquid like behavior of the metaphosphate liquids with lower fragility.

3.2 Introduction

Phosphate glasses, characterized by their compositional flexibility for glass formation and their unique properties, including low processing temperature, high solubility of rare earth and other high field strength cations, moderately high refractive index and low optic dispersion, high thermal expansion coefficient and bioactivity, are of significant importance in a wide range of technological applications.[1–6] Besides their technological importance, however, phosphate glass-forming liquids have drawn great attention in recent years as interesting model systems for understanding the fundamental connection between the structural connectivity of a glassy network and the glass transition and viscosity of the corresponding supercooled liquid.[7–12]

Recent studies by Sidebottom and coworkers [7,9,11,12] have shown the existence of an interesting trend of the fragility index *m*, a measure of the rate of change in viscosity $\eta(T)$ with temperature near and above T_g, defined as $m = \left.\frac{d\log\eta(T)}{d(T_g/T)}\right|_{T=T_g}$ as a function of structural connectivity <n> in alkali phosphate liquids with ≥ 50 mol% P_2O_5. Here, the structural connectivity <n> is defined as the average number of bridging oxygen per PO_4 tetrahedron in the glass structure, which varies from 2 in metaphosphates with 50% P_2O_5 to 3 in pure P_2O_5. The alkali metaphosphate liquids, containing chains (and possibly rings) of corner-sharing PO_4 tetrahedra, are characterized by high fragility (*m* ~ 80) [9]. Progressive addition of P_2O_5 results in an increasingly connected network with lower *m*, until <n> reaches its maximum value of 3 for pure P_2O_5 and concomitantly *m* reaches its minimum value of ~ 20 [9]. Most interestingly, *m*, when plotted as a function of <n>, shows a relatively abrupt transition at <n> ranging between 2.2 and 2.4, similar to that shown by the fragility of a wide variety of chalcogenide glass-forming liquids as a function of the connectivity of the structural network expressed in the form of the

average coordination number <r> [11]. Sidebottom and coworkers conjectured this similarity to be indicative of a fundamental connection between the connectivity of the structural network of glass-forming liquids and their fragility.[11] Such dependence of *m* on the connectivity of the phosphate network in alkali phosphates is indicative of only weak coupling of the modifier alkali ions with shear relaxation and viscous flow in these liquids. Hermansen *et al.*[8] , on the other hand, noted the need for considering alkali-oxygen bonds as a temperature dependent constraint that is broken above T_g in order to explain the composition dependent variation of *m* and T_g in alkali phosphate liquids. Muñoz-Senovilla *et al.*[10] reported that metaphosphate glasses with high field strength alkaline-earth and Zn modifier ions are characterized by lower *m* compared to their low field strength alkali counterparts, although no clear trend was observed within each group of metaphosphates. The field strength of the modifier alkali or alkaline-earth cation was expressed in this study as *Z/a*, where *Z* and *a* represent the nominal charge and the radius of the ion, respectively. The same study reported a clear linear trend in the variation in T_g of these glasses with the product of the field strength of the modifier cation and its coordination number *N*. Such a trend is, however, consistent with the expectation that the T_g of a metaphosphate liquid is linked to the strength of the modifier-oxygen (M-O) bonds and the connectivity of the network provided by the M-O coordination polyhedra.

The difference between the monovalent alkalis and the divalent alkaline-earth and Zn modifiers in their interaction with the phosphate network and their role in controlling the fragility is particularly apparent in the variation of *m* along the Na-Zn metaphosphate join.[12] For these liquids, *m* spans an impressive range from ~70 for the Na-metaphosphate liquid to ~28 for its Zn counterpart. The remarkably low fragility of the Zn-metaphosphate liquid has been attributed to an unusual network-forming role of Zn, where the ZnO_4 tetrahedra crosslink the $[PO_3]_n^{-1}$ chains

to form a 3-dimensional rigid network. Therefore, the fragility and T_g of metaphosphate liquids can vary over a relatively large range depending on the nature of the modifier cation and the degree of crosslinking between the $[PO_3]_n^{-1}$ chains via the M-O polyhedra. Here we present the viscosity, fragility and shear relaxation results for Sn and Ag metaphosphate liquids and probe the importance of the field strength and the coordination number of modifier cations in controlling the dynamical behavior of metaphosphate liquids. In this study we have used the more traditional definition of the field strength of a modifier (M) ion: Z/r^2, where r is the average M-O distance in the nearest-neighbor coordination shell. The Sn and Ag metaphosphate compositions are chosen for this purpose as both Sn^{2+} and Ag^+ have similar coordination number (~ 3.0-3.5) but rather different field strengths (Z/r^2 ~0.35 for Sn^{2+} vs. 0.16 for Ag^+).[13–16] The results indicate that the degree and strength of crosslinking between the $[PO_3]_n^{-1}$ chains, as provided by the M-O polyhedra, is the dominant factor that controls the fragility of these metaphosphate liquids. The most extreme behavior is observed in the Ag-metaphosphate liquid where, owing to their lowest field strength and coordination number, the Ag^+ cations do not provide any significant crosslinking of the $[PO_3]_n^{-1}$ chains. Consequently, the viscoelastic relaxation behavior of this metaphosphate liquid resembles that of low-molecular-weight chain polymers.

3.3 Experimental Methods

3.3.1 Sample preparation and physical characterization

The metaphosphate glasses SnP_2O_6 and $AgPO_3$ were prepared by conventional melt-quenching method.[13,15] The Sn-metaphosphate glass was synthesized from $Sn_2P_2O_7$ (Alfa) and P_2O_5 (J.T. Baker). The $Sn_2P_2O_7$ was first heated and held for an hour at 200°C, to remove any water. P_2O_5 was then added and the mixture was transferred into a fused silica ampoule that was

evacuated and the batch was melted in a rocking furnace at 1000°C for 30 minutes. The melt was subsequently quenched by dipping the ampoule in water. The as-made glass samples were annealed at temperature 20°C lower than T_g for 1 hour. The $AgPO_3$ glass was synthesized using reagent grade $NH_4H_2PO_4$ (Fisher) and $AgNO_3$ (J.T. Baker). The mixture was first loaded into a quartz crucible and calcined at 350°C for 17 hours to drive off water and ammonia. Subsequently, the calcined batch was melted at 600°C for 15 minutes. The glass was made by quenching the melt onto a steel plate. Both glass samples were stored in a desiccator to avoid exposure to atmospheric moisture.

The T_g of these metaphosphate glasses was determined using differential scanning calorimetry (Mettler Toledo DSC1). Samples of mass ~15-20 mg were taken in hermetically sealed Al pans and were heated to 50 °C above T_g to erase any thermal history. The samples were then cooled in the calorimeter at a rate of 10 K/min and subsequently reheated at the same rate. $T_g$was determined to within ± 2 °C as the onset of the glass transition endotherm.

3.3.2 Viscosity and shear relaxation measurements

The shear relaxation behavior of SnP_2O_6 and $AgPO_3$ liquids and their viscosity in the range of ~10^8-10^3 Pa.s were measured using a parallel plate rheometer (ARES G2, TA Instruments) under oscillatory mode in an environment of flowing nitrogen gas. In this rheometer, sinusoidal strain at desired angular frequency ω was applied by the lower plate. Corresponding stress response was obtained via the torque transducer through the upper plate (~8 mm diameter), which allows the determination of the storage shear modulus G', loss shear modulus G'', phase angle difference δ, and viscosity η as a function of ω. Before rheometry measurements, all glass samples were softened and trimmed between the plates to form a sandwich-like geometry with a thickness

of ~1 mm. The temperature was controlled with a forced-convection oven. Multiple frequency sweeps within the range of 1 to 628 rad/s were carried out at various temperatures with 10 K intervals where the strain was controlled within the linear viscoelastic region. The Newtonian viscosity η $(\omega = 0)$ was recovered at high-temperature and low-frequency region where the viscosity value was frequency-independent. More details on the rheometry experiments and data processing can be found in previous publications.[17,18]

The low-temperature viscosity of these liquids in the range of ~ 10^9-10^{11} Pa.s was measured using a thermo-mechanical analyzer (TMA; Setsys Evolution, SETARAM) under non-oscillating load. In this setup, the temporal variation of the height $h(t)$ of a cylindrical sample is measured with a resolution of 0.004 μm, while it is subjected to a desired load, using a differential transformer displacement sensor. The temperature was controlled with a T-type thermocouple placed next to the sample. The measurements were carried out on glass samples that were cut and polished into cylindrical shape with a diameter less than that of the probe (~5 mm) and a height of ~2 mm. These glass samples were placed between two silica plates (~5mm diameter, ~1.5mm height) in order to avoid any surface interaction with the alumina sample holder and probe head. For each measurement the sample was first heated to the desired temperature at a rate of 10 K/min and held at the temperature for 5 min to reach thermal equilibrium under a load of 5 gf. The load was then increased to 50 gf prior to carrying out the viscosity measurement. The time derivative of displacement $\frac{dh}{dt}$ was observed to reach equilibrium after a typical initial transient period. The corresponding equilibrium viscosity η was only calculated when $\frac{dh}{dt}$ no longer changed more than 0.01 μm/s within a period of 2 min, using the following relation [19]:

$$\eta = \frac{196\pi F h^5(t)}{3V * \frac{dh}{dt} * [2\pi h^3(t) + V]} \quad (1)$$

where η is the viscosity in Pa·s, F is the applied force in gf, $h(t)$ is the sample thickness at time t in cm and V is the sample volume in cm^3. V was measured at room temperature and any temperature dependent change in V was considered to have negligible effect on viscosity in the temperature range of these measurements.

3.4 Results and Discussion

The Ag-O coordination number in glassy $AgPO_3$ was reported by Musino *et al.* on the basis of X-ray diffraction studies to be ~ 3.4, while Rodrigues and Wondraczek reported a literature average of ~ 2.7. [20,21]. On the other hand, a recent ^{119}Sn nuclear magnetic resonance spectroscopic study [13] indicated that the Sn-O coordination number in the SnP_2O_6 glass is between 3 and 4. Here I have approximated the Ag-O and Sn-O coordination numbers N to be 3.2±0.2 and 3.5±0.5, respectively, and used the Z/r^2 values of 0.35 for Sn^{2+} vs. 0.16 for Ag^+ to show the T_g values of the SnP_2O_6 and $AgPO_3$ glasses obtained in this study in Fig. 3-1 as a function of $(Z/r^2)*N$, and compared with those reported in the literature for other metaphosphate glasses [10,22–25] (Table 3-1). These T_g values follow an approximately linear trend with $(Z/r^2)*N$ (Fig. 3-1). Since the phosphate network in all metaphosphate glasses is rather similar, the increasing trend of T_g with $(Z/r^2)*N$ is consistent with the increasingly strong and extensive inter-chain connectivity provided by the M-O polyhedra.

Table 3-1

T_g, average values of modifier-oxygen bond distance r, cationic field strength Z/r^2, modifier-oxygen coordination number N and fragility m for MO-P_2O_5 (M=Ba, Sr, Ca, Zn, Mg, Sn) and M^*_2O-P_2O_5 (M^*=Na, Li, Ag) glasses.

	T_g (K)	r (Å)	Z/r^2 (Å^{-2})	N	m
Ba	756[27]	2.79[28]	0.26	8.9[28]	47.4[10]
Sr	753[29]	2.55[28]	0.31	8.2[28]	45.9[10]
Ca	806[30]	2.39[28]	0.35	7.0±0.4[28]	46.8[10]
Zn	691[31]	1.95[32]	0.53	4.3±0.2[28]	28.5[10]
Mg	838[27]	2.03[32]	0.49	5.5±0.4[28]	45.6[10]
Na	560[33]	2.38[28]	0.18	5.0±0.4[28]	64.6[10]
Li	597[34]	2.03[35]	0.24	4.0±0.4[35]	77.9[10]
Sn	533	2.40[36]	0.35	3.5±0.5[13]	53±3
Ag	449	2.36[20]	0.18	3.2±0.2[20,21]	90±3

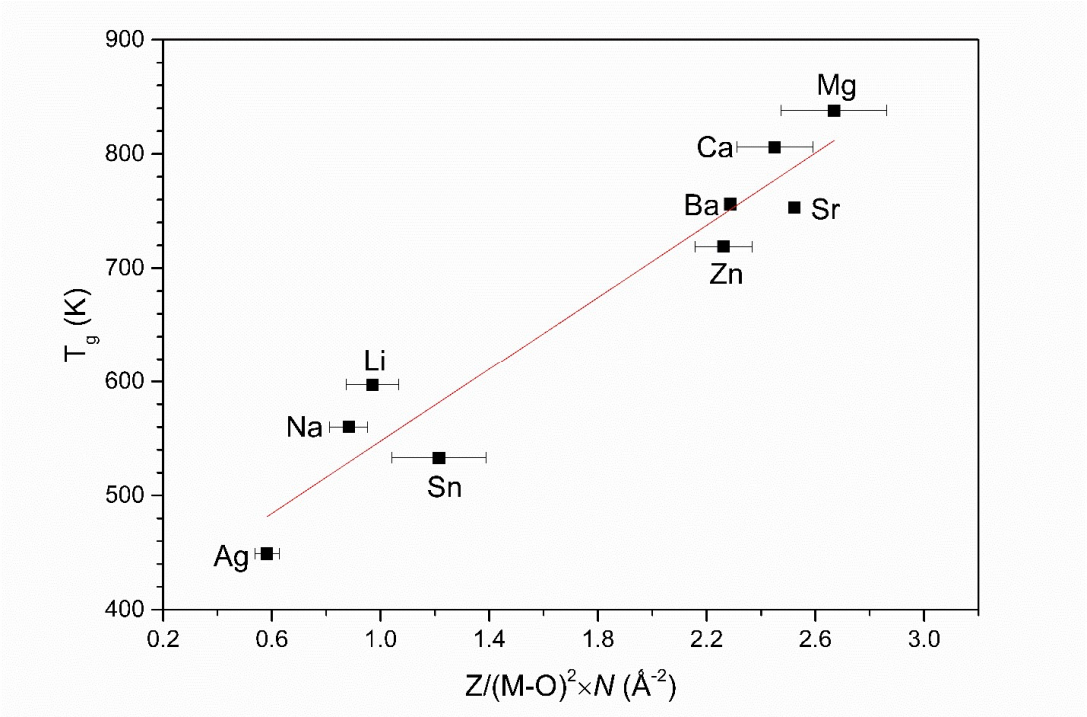

Figure 3-1 Glass transition temperature of MO-P_2O_5 (M=Ba, Sr, Ca, Zn, Mg, Sn) and M^*_2O-P_2O_5 (M^*=Na, Li, Ag) metaphosphate glasses measured in present study and reported in the literature, as a function of $(Z/r^2)*N$. The line is drawn as a guide to the eye. See Table 3-1 for source of literature data.

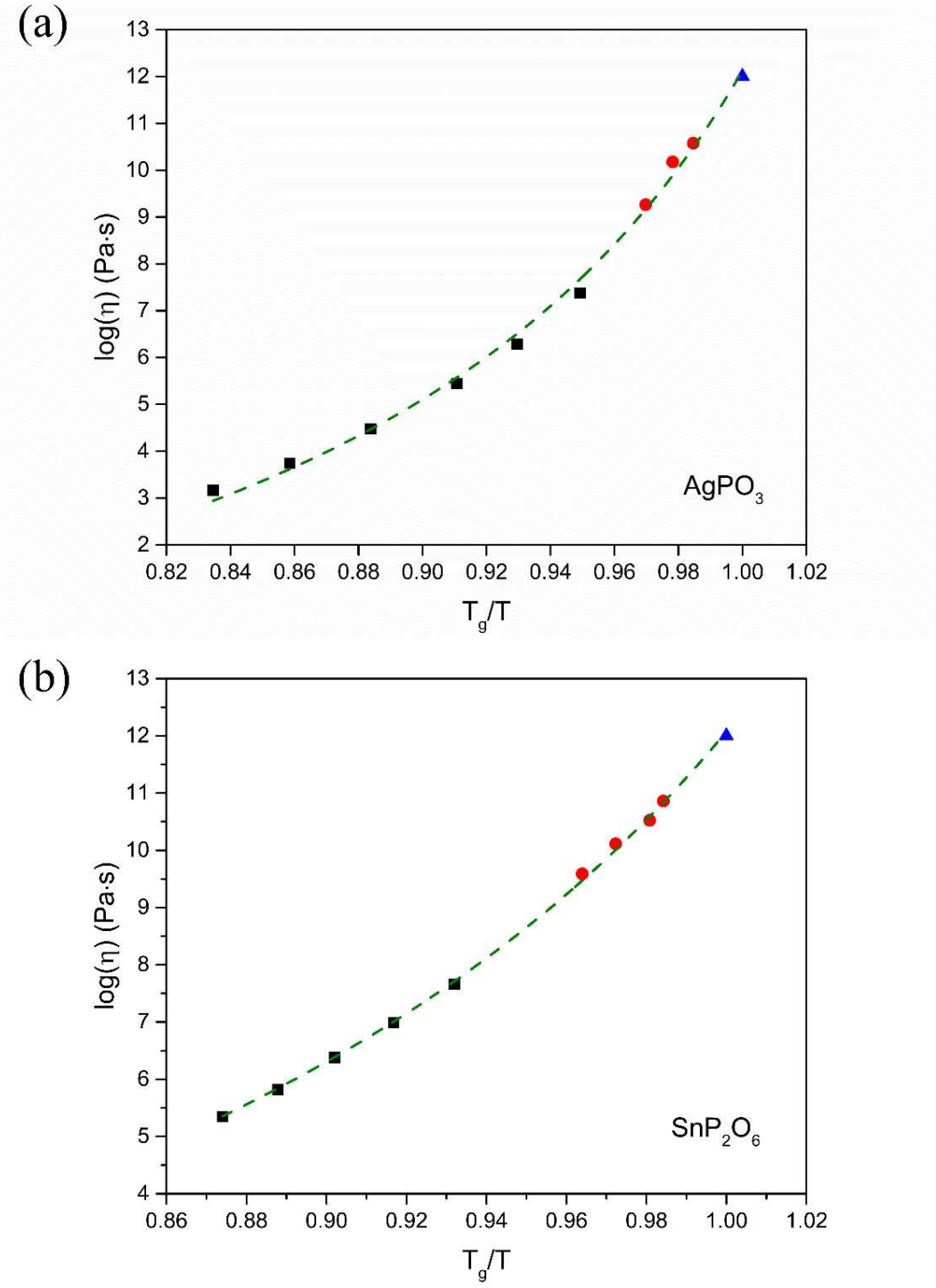

Figure 3-2 Temperature dependence of the viscosity of (a) $AgPO_3$ and (b) SnP_2O_6 liquids measured using a rheometer (squares) and a TMA (circles). Dashed lines through the data correspond to least squares fits to the VFT equation. The viscosity at T_g is taken to be 10^{12} Pa.s and is denoted by the triangle in each plot.

The viscosity η of Ag- and Sn-metaphosphate liquids, measured using parallel-plate techniques, is shown in Fig. 3-2 as a function of reduced temperature T_g/T. The temperature dependence of the viscosity for both liquids can be expressed using the Vogel-Fulcher-Tammann (VFT) equation:

$$log\eta(T) = A + \frac{B}{T - T_0} \qquad (2)$$

where *A*, *B* and T_0 are material-dependent constants. The fragility *m* of these liquids is obtained from the activation energy of viscous flow *E* near T_g using the relation[26]:

$$m = \frac{E}{RT_g \ln 10} \qquad (3)$$

This procedure yields $m \approx 53\pm3$ and 90 ± 3, respectively, for SnP_2O_6 and $AgPO_3$ (Table 3-1). Similar to T_g, the fragility parameter *m* of the Sn and Ag –metaphosphate liquids, when taken together with those of other metaphosphate liquids, shows a systematic variation with $(Z/r^2)*N$, as shown in Fig. 3-3. As noted earlier, this observation is consistent with the proposal by Sidebottom and coworkers that fragility of a network liquid is fundamentally linked to its connectivity.[7,9,11,12] These authors primarily focused on the systematic variation of *m* with the connectivity <n> of the phosphate network. However, the phosphate network in all metaphosphate liquids considered in this chapter has the same degree of connectivity between the PO_4 tetrahedra that result in $[PO_3]_n^{-1}$ chains. Therefore, the fragility variation in Fig. 3-3 is expected to be controlled by both the degree and strength of crosslinking between these chains. Since this crosslinking is provided by the modifier-oxygen polyhedra, the product of the M-O coordination number *N* and the field strength of the M cation i.e. $(Z/r^2)*N$ serves as a measure of

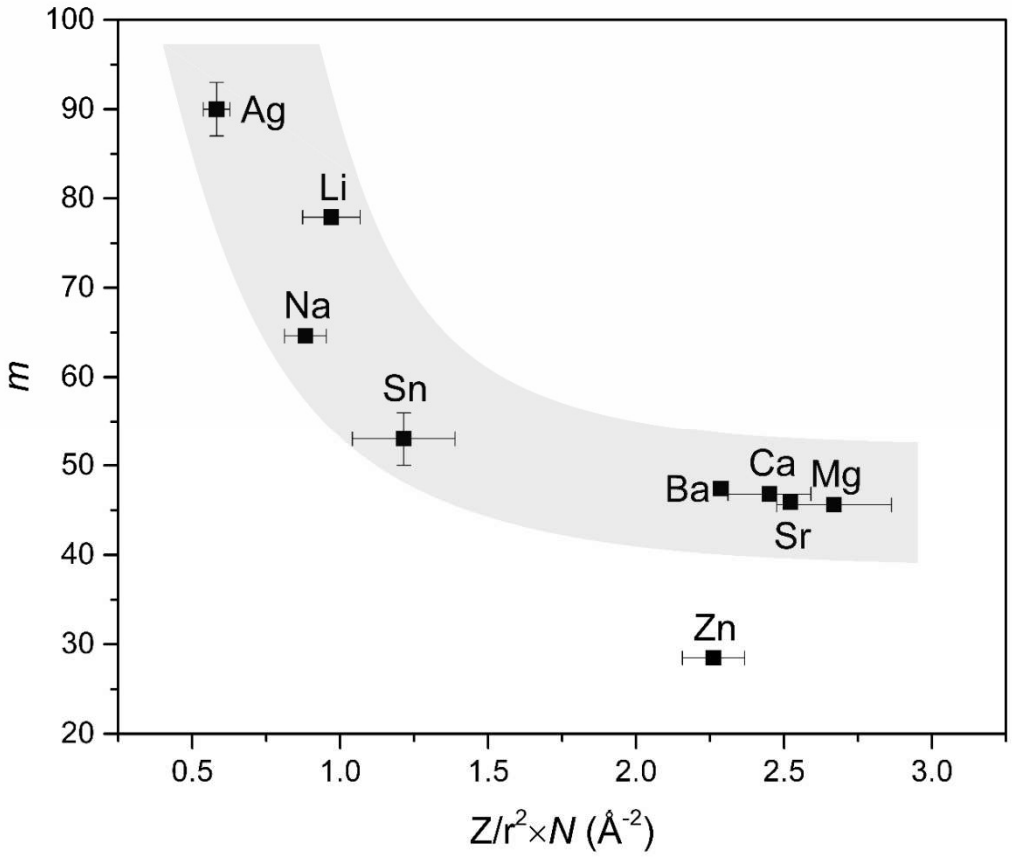

Figure 3-3 Fragility index *m* of MO-P_2O_5 (M=Ba, Sr, Ca, Zn, Mg, Sn) and M^*_2O-P_2O_5 (M^*=Na, Li, Ag) liquids measured in present study and reported in the literature, as a function of $(Z/r^2)*N$. See Table 3-1 for source of literature data.

the strength and extent of inter-chain connectivity. Fragility drops rapidly on increasing $(Z/r^2)*N$ from ~ 0.5 to 1.5 and remains nearly constant thereafter (Fig. 3-3). It may be noted that Zn shows a small but significant departure from this trend with an unusually low *m* of ~ 30 (Fig. 3-3). The highest fragility of the $AgPO_3$ liquid indicates the weakest crosslinking between the phosphate chains in this liquid and hence, the Ag ions are strongly decoupled from the structural network. This hypothesis is consistent with the fact that, among the metaphosphates, the Ag-metaphosphate glass displays the highest ionic conductivity. For example, the ionic conductivity for the $AgPO_3$ glass at 423 K is ~10^{-4} $\Omega^{-1}cm^{-1}$, an order of magnitude higher than that of the $LiPO_3$ glass,[37,38]

which suggests that, for a comparable carrier density, the mobility of Ag ions is an order of magnitude higher than that of Li ions. Therefore, the weakest crosslinking between the phosphate chains is expected in the Ag-metaphosphate, which is indeed manifested in its highest fragility (Fig. 3-3). Consequently, one may expect a rheological behavior for the $AgPO_3$ liquid that, among all metaphosphate liquids, would be most akin to that of a low-molecular-weight chain polymer. This hypothesis is tested by investigating the shear relaxation behavior of SnP_2O_6 and $AgPO_3$ liquids and comparing it with the previously published results by Sammler *et al.* on the relaxation behavior of an alkali-zinc phosphate liquid with relatively low fragility ($m \sim 40$).[39] The master plots of the angular frequency ω dependence of the storage modulus G' and the loss modulus G″ of these supercooled liquids are shown in Fig. 3-4 after performing time-temperature superposition (TTS).[17] At low frequencies all liquids display G' < G″. It is particularly instructive to note the frequency dependence of G′(ω). Maxwell's theory of viscoelasticity predicts frequency scaling relations: $G' \sim \omega^2$ and $G'' \sim \omega$ in the terminal regime where $\omega\tau << 1$, τ being the characteristic relaxation time. While G″ for all phosphate liquids in Fig. 3-4 follows this prediction, G′ follows the predicted scaling only for the alkali-zinc phosphate liquid. In contrast, G′(ω) for the Sn and Ag –metaphosphate liquids with higher fragility shows departure from the predicted scaling in the terminal regime, displaying a frequency scaling $G'(\omega) \sim \omega^{1.6}$. Such departure of the scaling of G′(ω) in the terminal regime has previously been reported for low-molecular-weight or short-chain polymer melts.[40] Moreover, for the $AgPO_3$ liquid, the frequency dependence of G′(ω) changes at higher frequencies to a linear scaling i.e. $G'(\omega) \sim \omega^{1.0}$, which continues until the G′- G″ crossover (Fig. 3-4). Similar scaling behavior was reported in the literature for several supramolecular polymeric liquids that consist of short chains of a few molecules, as well as for glass-forming As-Se liquids with short Se chains.[18,41,42]

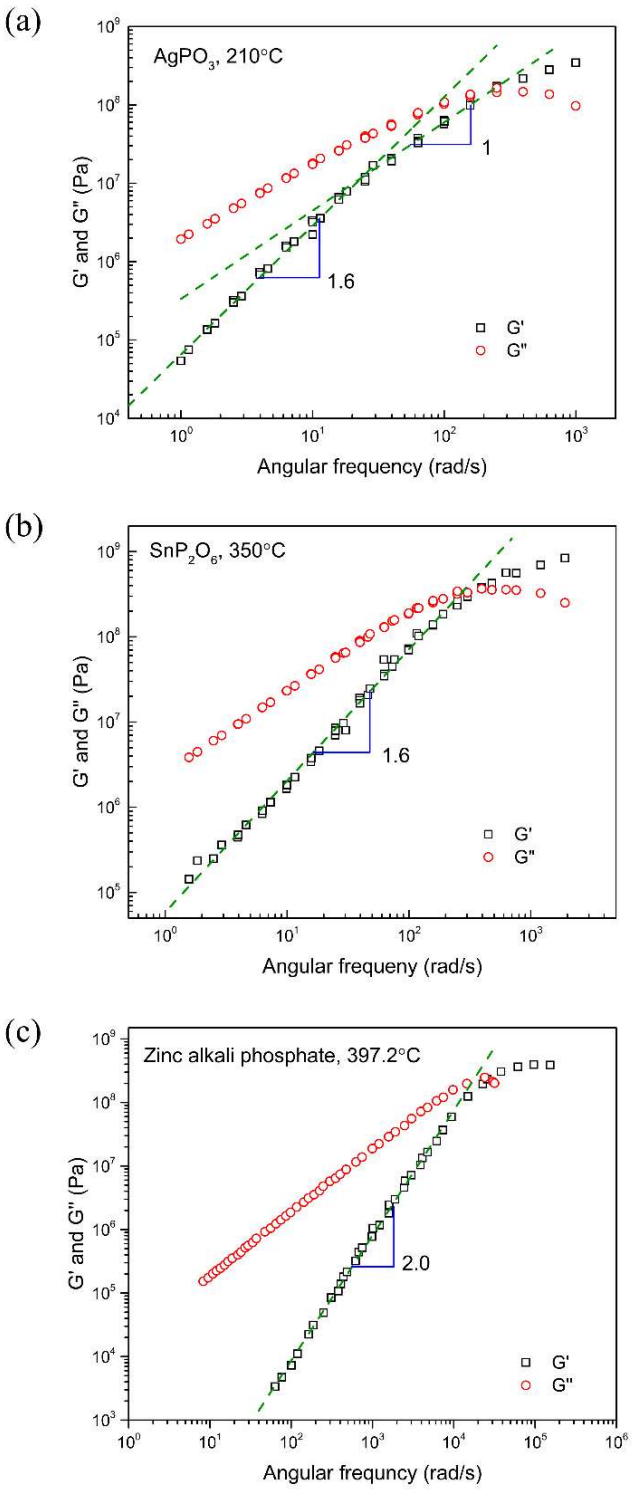

Figure 3-4 Master plots of angular frequency dependence of storage modulus G' (squares) and loss modulus G″ (circles) for (a) $AgPO_3$, (b) SnP_2O_6 and (c) alkali-zinc phosphate liquids. Corresponding temperatures for TTS are shown in the inset. Data for the alkali-zinc phosphate liquid is from Ref. 29.

Thus, when taken together, the shear relaxation results suggest that the phosphate chains in the $AgPO_3$ liquid are the least constrained and can perform segmental motion much like the unentangled low-molecular-weight chain polymers. On the other hand, the phosphate chains are dynamically more constrained in the alkali-zinc metaphosphate liquid, which is likely responsible for its lower fragility. The strongest crosslinking of these chains is probably achieved in the Zn-metaphosphate liquid, in view of its lowest fragility among all metaphosphate liquids. In a recent study Kunal *et al.*[43] proposed that polymers with identical backbones are more fragile when the side groups are more flexible. It may be argued that the M-O polyhedra in metaphosphate liquids play the role of side groups, which are then less flexible for modifiers characterized by high coordination number and strong M-O bonding (e.g. Zn or Mg with high $(Z/r^2)*N$, see Table 3-1) and thus, give rise to lower fragility.

It is important to note that the mechanisms for the structural relaxation in supercooled phosphate liquids that have been proposed in the literature range from local P-O bond breaking to segmental chain dynamics.[1,44] We argue that, while both processes could be operative in a phosphate liquid, the relaxation in a highly fragile metaphosphate liquid is likely dominated by the $[PO_3]_n^{-1}$ chain dynamics. On the other hand, the short-range process of P-O bond breaking becomes increasingly important in less fragile and more polymerized ultraphosphate (>50 mol% P_2O_5) liquids[44] or when strong crosslinking of the chains by the M-O polyhedra in metaphosphate liquids effectively turns the structure into a 3-dimensional network. The presence of multiple relaxation mechanisms with different activation energy may render a glass-forming liquid fragile as well as thermorheologically complex, i.e. the TTS principle is not strictly obeyed. In order to explore this issue further, the variation of the phase angle δ ($= \tan^{-1} G''/ G'$) vs. the absolute value of the complex modulus $|G^*| = \sqrt{G'^2 + G''^2}$ is shown in Fig. 3-5 in the form

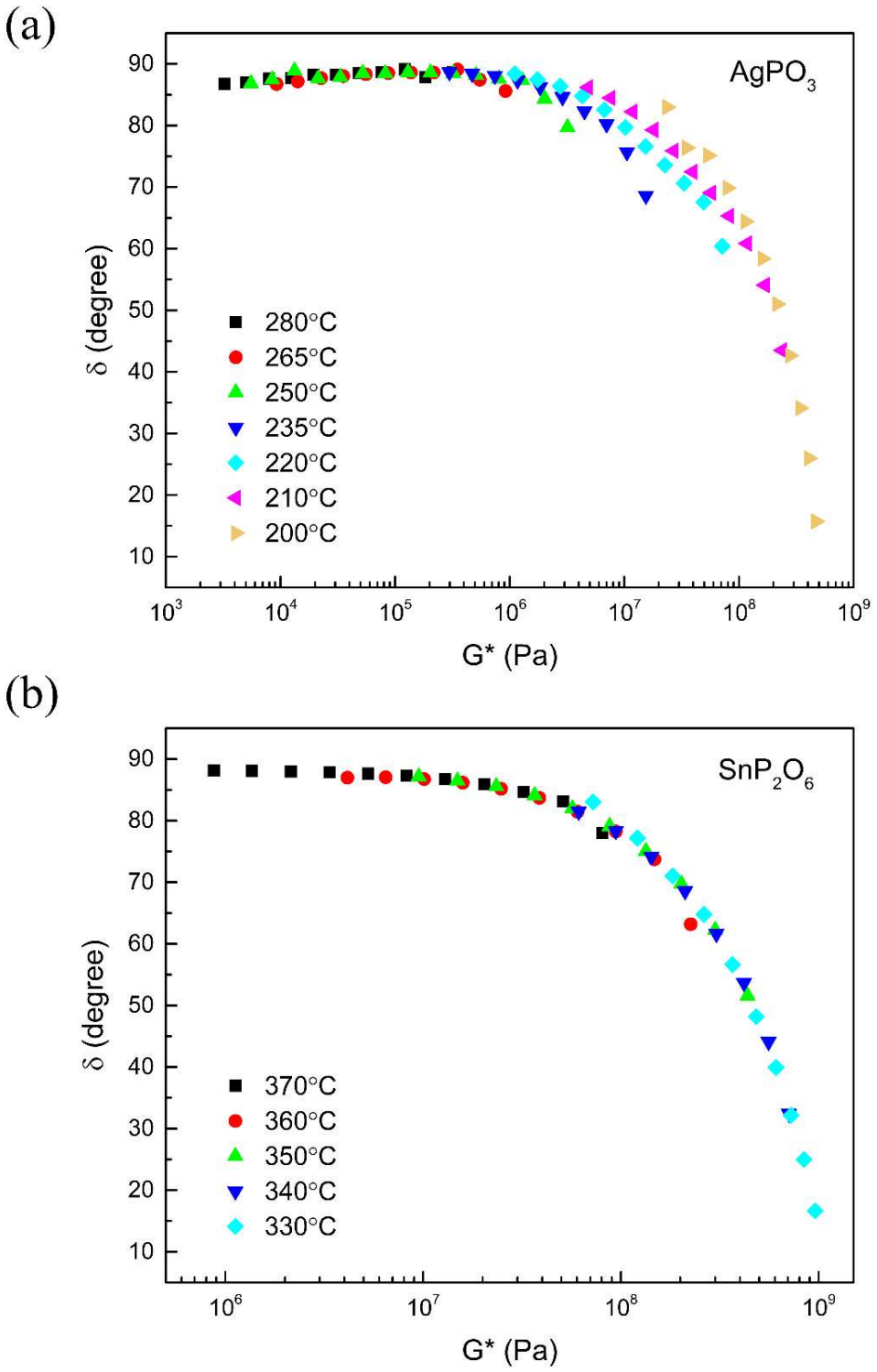

Figure 3-5 The van Gurp-Palmen plot of phase angle δ versus G^* for (a) $AgPO_3$ and (b) SnP_2O_6 liquids.

of a van Gurp – Palmen (vGP) plot for the Ag- and Sn- metaphosphate liquids.[45] This way of plotting is typically used to verify the TTS principle. If a liquid is thermorheologically simple, then the data in a vGP plot at different temperatures are expected to fall on a single curve without any frequency shift.[45,46] In their previous work Sammler *et al.* have shown the thermorheological simplicity of the alkali-zinc phosphate liquid.[39] Moreover, previous studies have shown that borate and silicate glass-forming liquids with low fragility are also thermorheologically simple and follow the Maxwell scaling of $G' \sim \omega^2$ and $G'' \sim \omega$ in the terminal regime.[47,48] The results obtained in the present study, on the other hand, indicate that while the SnP_2O_6 liquid is thermorheologically simple, the most fragile $AgPO_3$ liquid is a thermorheologically complex liquid (Fig. 3-5). Such violation of thermorheological simplicity is likely indicative of the existence of multiple relaxation processes with different activation energies in the $AgPO_3$ liquid.

3.5 Conclusion

The fragility index *m* of supercooled metaphosphate liquids shows a systematic trend with the modifier-oxygen coordination number *N* and decreases rapidly from its highest value of ~90 for the $AgPO_3$ liquid to ~40, as $(Z/r^2)*N$ increases from ~ 0.5 to 1.5. Further increase in $(Z/r^2)*N$ up to ~ 2.5 does not appear to significantly affect *m*. This trend in *m* can be related to the extent and the strength of crosslinking of the $[PO_3]_n^{-1}$ chains in the structure by the modifier cations. The weak inter-chain linking in the highly fragile Ag- metaphosphate liquid results in shear relaxation via segmental motion of $[PO_3]_n^{-1}$ chains, similar to the rheological behavior of low-molecular-weight chain polymers. This liquid is also found to be thermorheologically complex, violating the time-temperature superposition. In contrast, strong phosphate liquids with low *m* display thermorheological simplicity and follow the Maxwell behavior in the terminal regime. Shear relaxation in these liquids is likely controlled by the local P-O bond breaking.

References

[1] R.K. Brow, Review: the structure of simple phosphate glasses, J. Non. Cryst. Solids. 263 (2000) 1–28.

[2] J.A. Wilder, Glasses and glass ceramics for sealing to aluminum alloys, J. Non. Cryst. Solids. 38–39 (1980) 879–884.

[3] C. Hönninger, F. Morier-Genoud, M. Moser, U. Keller, L.R. Brovelli, C. Harder, Efficient and tunable diode-pumped femtosecond Yb:glass lasers, Opt. Lett. 23 (1998) 126.

[4] E.H. Oelkers, J. Montel, Waste Storage, Elements. 4 (2008) 113–116.

[5] L.L. Hench, R.J. Splinter, W.C. Allen, T.K. Greenlee, Bonding mechanisms at the interface of ceramic prosthetic materials, J. Biomed. Mater. Res. 5 (1971) 117–141.

[6] C. Bergmann, M. Lindner, W. Zhang, K. Koczur, A. Kirsten, R. Telle, H. Fischer, 3D printing of bone substitute implants using calcium phosphate and bioactive glasses, J. Eur. Ceram. Soc. 30 (2010) 2563–2567.

[7] T.D. Tran, D.L. Sidebottom, Glass-forming dynamics of aluminophosphate melts studied by photon correlation spectroscopy, J. Am. Ceram. Soc. 96 (2013) 2147–2154.

[8] C. Hermansen, J.C. Mauro, Y. Yue, A model for phosphate glass topology considering the modifying ion sub-network, J. Chem. Phys. 140 (2014).

[9] D.L. Sidebottom, T.D. Tran, S.E. Schnell, Building up a weaker network: The effect of intermediate range glass structure on liquid fragility, J. Non. Cryst. Solids. 402 (2014) 16–20.

[10] L. Muñoz-senovilla, F. Muñoz, Behaviour of viscosity in metaphosphate glasses, J. Non. Cryst. Solids. 385 (2014) 9–16.

[11] D.L. Sidebottom, Fragility of network-forming glasses: A universal dependence on the topological connectivity, Phys. Rev. E - Stat. Nonlinear, Soft Matter Phys. 92 (2015) 1–9.

[12] D.L. Sidebottom, D. Vu, Assessing the network connectivity of modifier ions in metaphosphate glass melts: A dynamic light scattering study of Na-Zn mixtures, J. Chem. Phys. 145 (2016).

[13] Y. Xia, M.A.T. Marple, I. Hung, Z. Gan, S. Sen, Network Structure and Connectivity in $SnO{-}P_2O_5$ Glasses : Results from 2D ^{31}P and ^{119}Sn NMR Spectroscopy, J. Non Cryst. Solids. 122 (2018) 7416–7425.

[14] M. Tachez, R. Mercier, J.P. Malugani, Structure determination of $AgPO_3$ and $(AgPO_3)_{0.5}(AgI)_{0.5}$ glasses by neutron diffraction and small angle neutron scattering, Solid State Commun. 25 (1987) 263–270.

[15] G. El-damrawi, A. Hassan, H. Doweidar, A. Shaboub, Structural Studies on Ag_2O-P_2O_5 Glasses, New J. Glas. Ceram. 7 (2017) 77–89.

[16] J.D. Wicks, L. Borjesson, G. Bushnell-Wye, W.S. Howells, R.L. McGreevy, Structure and Ionic Conduction in $(AgI)_x(AgPO_3)_{1-x}$ Glasses, Phys. Rev. Lett. 74 (1995) 726.

[17] S. Sen, W. Zhu, B.G. Aitken, Behavior of a supercooled chalcogenide liquid in the non-

Newtonian regime under steady vs . oscillatory shear, J. Chem. Phys. 147 (2017) 034508.

[18] W. Zhu, M. Lockhart, B. Aitken, S. Sen, Dynamical rigidity transition in the viscoelastic properties of chalcogenide glass-forming liquids, J. Non. Cryst. Solids. 502 (2018) 244–248.

[19] J. Wang, Glass viscosity and structural relaxation by parallel plate rheometry using a thermo-mechanical analyser, Mater. Lett. 31 (1997) 99–103.

[20] A. Musinu, G. Paschina, G. Piccaluga, G. Pinna, Short range order of metaphosphate glasses by X-ray diffraction, J. Non. Cryst. Solids. 177 (1994) 97–102.

[21] B.P. Rodrigues, L. Wondraczek, Cationic constraint effects in metaphosphate glasses, J. Chem. Phys. 140 (2014) 214501.

[22] A. Hayashi, T. Konishi, K. Tadanaga, T. Minami, M. Tatsumisago, Preparation and characterization of SnO-P_2O_5 glasses as anode materials for lithium secondary batteries, J. Non. Cryst. Solids. 345–346 (2004) 478–483.

[23] J.W. Lim, S.W. Yung, R.K. Brow, Properties and structure of binary tin phosphate glasses, J. Non. Cryst. Solids. 357 (2011) 2690–2694.

[24] W. Pascheto, M.G. Parthun, A. Hallbrucker, G.P. Johari, Calorimetric studies of structural relaxation in AgI-$AgPO_3$ glasses, J. Non. Cryst. Solids. 171 (1994) 182–190.

[25] H. Kobayashi, H. Takahashi, Y. Hiki, Viscosity of glasses near and below the glass transition temperature, J. Appl. Phys. 88 (2000) 3776–3778.

[26] K.F. Kelton, Kinetic and structural fragility - A correlation between structures and dynamics in metallic liquids and glasses, J. Phys. Condens. Matter. 29 (2017) 023002.

[27] C.B. Bragatto, D.R. Cassar, O. Peitl, J.L. Souquet, A.C.M. Rodrigues, Structural relaxation in $AgPO_3$ glass followed by in situ ionic conductivity measurements, J. Non. Cryst. Solids. 437 (2016) 43–47.

[28] S.W. Martin, C.A. Angell, DC and AC Conductivity in Wide Comparison Range Li_2O-P_2O_5 Glasses, J. Non. Cryst. Solids. 83 (1986) 185–207.

[29] R.L. Sammler, J.U. Otaigbe, M.L. Lapham, N.L. Bradley, B.C. Monahan, C.J. Quinn, Melt rheology of zinc alkali phosphate glasses, J. Rheol. 40 (1996) 285.

[30] V.R. Raju, G.G. Smith, G. Marin, J.R. Knox, W.W. Graessley, Properties of Amorphous and Crystallizable Hydrocarbon Polymers. I. Melt Rheology of Fractions of Linear Polyethylene*, J. Polym. Sci. Polym. Phys. Ed. 17 (1979) 1183–1195.

[31] C. Gainaru, R. Figuli, T. Hecksher, B. Jakobsen, J.C. Dyre, M. Wilhelm, R. Böhmer, Shear-Modulus investigations of monohydroxy alcohols: Evidence for a short-chain-polymer rheological response, Phys. Rev. Lett. 112 (2014) 1–4.

[32] N. Lou, Y. Wang, X. Li, H. Li, P. Wang, C. Wesdemiotis, A.P. Sokolov, H. Xiong, Dielectric relaxation and rheological behavior of supramolecular polymeric liquid, Macromolecules. 46 (2013) 3160–3166.

[33] K. Kunal, C.G. Robertson, S. Pawlus, S.F. Hahn, A.P. Sokolov, Role of Chemical Structure in Fragility of Polymers : A Qualitative Picture, Macromolecules. 41 (2008) 7232–7238.

[34] S. Wegner, L. Van Wüllen, G. Tricot, Network dynamics and species exchange processes in aluminophosphate glasses: An in situ high temperature magic angle spinning NMR view, J. Phys. Chem. B. 113 (2009) 416–425.

[35] S. Trinkle, C. Friedrich, Van Gurp-Palmen-plot : a way to characterize polydispersity of linear polymers, Rheol. Acta. 40 (2001) 322–328.

[36] W. Zhu, B.G. Aitken, S. Sen, Communication: Observation of ultra-slow relaxation in supercooled selenium and related glass-forming liquids, J. Chem. Phys. 148 (2018) 111101.

[37] J.J. Mills, Low frequency storage and loss moduli of soda-silica glasses in the transfoilmation range, J. Non. Cryst. Solids. 14 (1974) 255–268.

[38] J. Tauke, T.A. Litovitz, P.B. Macedo, Viscous Relaxation and Non-Arrhenius Behavior in B_2O_3, J. Am. Ceram. Soc. 51 (1968) 158–163.

[39] E. Metwalli, R.K. Brow, Modifier effects on the properties and structures of aluminophosphate glasses, J. Non Cryst. Solids. 289 (2001) 113–122.

[40] U. Hoppe, G. Walter, R. Kranold, D. Stachel, Structural specifics of phosphate glasses probed by diffraction methods: a review, J. Non. Cryst. Solids. 263–264 (2000) 29–47.

[41] I. Konidakis, C.P.E. Varsamis, E.I. Kamitsos, D. Möncke, D. Ehrt, Structure and properties of mixed strontium-manganese metaphosphate glasses, J. Phys. Chem. C. 114 (2010) 9125–9138.

[42] P. Prokupkova, P. Mosner, L. Koudelka, M. Vlcek, Preparation and study of $Ca_{1-x}Mg_x(PO_3)_2$ glassy and crystalline phases, J. Mater. Sci. 33 (1998) 743–748.

[43] G. Walter, U. Hoppe, J. Vogel, G. Carl, P. Hartmann, The structure of zinc polyphosphate glass studied by diffraction methods and ^{31}P NMR, J. Non. Cryst. Solids. 356 (2010) 252–262.

[44] U. Hoppe, D. Stache, D. Beyer, The oxygen coordination of metal ions in phosphate and silicate glasses studied by a combination of x-ray and neutron diffraction, Phys. Scr. 1995 (1995) 122–126.

[45] J.J. Hudgens, R.K. Brow, D.R. Tallant, S.W. Martin, Raman spectroscopy study of the structure of lithium and sodium ultraphosphate glasses, J. Non. Cryst. Solids. 223 (1998) 21–31.

[46] L. Van Wüllen, H. Eckert, G. Schwering, Structure-property correlations in lithium phosphate glasses: New insights from ^{31}P mutually implies ^{7}Li double-resonance NMR, Chem. Mater. 12 (2000) 1840–1846.

[47] J. Swenson, A. Matic, A. Brodin, L. Borjesson, W.S. Howells, Structure of mixed alkali phosphate glasses by neutron diffraction and Raman spectroscopy, Phys. Rev. B. 58 (1999) 11331–11337.

[48] V. Martin, U. Werner-Zwanziger, J.W. Zwanziger, R.A. Dunlap, Correlation of Structure and Photoelastic Response in Tin Phosphate Glass, Int. J. Appl. Glas. Sci. 2 (2011) 282–289.

Chapter 4

Observation of Polymer-like Flow Mechanism in a Short-chain Phosphate Glass-forming Liquid

4.1 Abstract

The dynamics of the phosphate chains and the attendant shear relaxation in a short-chain silver phosphate glass-forming liquid of composition 51.5%Ag_2O-48.5% P_2O_5 are studied using a combination of high-temperature ^{31}P NMR spectroscopy and parallel plate rheometry. The temperature-dependent evolution of the ^{31}P NMR spectral line shapes indicates that the constituent PO_4 tetrahedral chains in this liquid undergo rapid rotational reorientation. The timescale of this dynamics is in complete agreement with that of shear relaxation and thus, must be responsible for the viscous flow of this liquid. These results demonstrate for the first time that although the shear relaxation of the network oxide glass-forming liquids are controlled by the scission and renewal of bonds between the network-forming cations and oxygen atoms, such a scenario may not be tenable for liquids with low-dimensional structures consisting of chains.

4.2 Introduction

An atomistic understanding of the mechanism of viscous flow and related dynamical processes in a glass-forming liquid associated with its structural relaxation is of great importance in testing various theoretical models of glass transition [1,2]. Previous dynamical studies of supercooled oxide network liquids have suggested a close mechanistic association between the breaking and reforming of the network and viscous flow[3]. For example, high-temperature ^{29}Si, ^{11}B and ^{17}O NMR spectroscopic studies have shown that in borate or silicate liquids the average time scale of the local Si-O or B-O bond breaking and chemical exchange between Si atoms belonging to different silicate tetrahedra, i.e. Q^n species where n corresponds to the number of bridging oxygen atoms per tetrahedron, or between B atoms in BO_3 and BO_4 species correspond very well with the shear relaxation time scale derived from the viscosity data [3–10]. The flow mechanism appears to be facilitated by the ability of oxygen ions to reconfigure between bridging and non-bridging arrangements, with attendant changes in silicon or boron configurations. It may be noted here that although these studies provided a tremendous wealth of structural and dynamical information, they have so far been restricted largely to 3-dimensional networks. On the other hand, little is known regarding the structural relaxation mechanisms in sparsely connected oxide networks with low-dimensional topological characteristics such as those dominated by chain-like moieties.

In this regard, the phosphate glass-forming liquids, characterized by their wide composition range for glass formation, can serve as important and unique model oxide systems for understanding the fundamental connection between the structural connectivity of a liquid and the temperature dependence of its viscosity $\eta(T)$ [11–14]. Particularly interesting in this regard are the metaphosphate liquids characterized by a structure consisting predominantly of long chains of

PO_4 tetrahedra with two P-O-P linkages per PO_4 tetrahedron i.e. the Q^2 species. Depending on the nature of the network-modifier cation, the viscosity vs. T_g/T behavior of metaphosphate liquids can span nearly the entire range covered by all inorganic glass-forming liquids, where T_g represents the glass transition temperature [12,14]. Recent rheological studies have suggested that the sharp drop in viscosity with increasing temperature above T_g, characteristic of metaphosphate liquids with low field-strength modifiers such as Ag, can be related to the weak inter-chain coupling and the viscous flow of these liquids is likely controlled by the segmental motion of the Q^2 chains [14]. On the other hand, the metaphosphate liquids with high field-strength modifiers such as Zn are characterized by rather low fragility due to the strong inter-chain cross-linking provided by the ZnO_4 tetrahedra [14]. The viscous flow of these latter liquids would likely be controlled by local P-O-P bond breaking, as in their silicate and borate analogues.

Previous high-temperature ^{31}P magic-angle-spinning nuclear magnetic resonance (MAS NMR) spectroscopic studies of binary K_2O-P_2O_5 and ternary K_2O-Al_2O_3-P_2O_5 liquids provided unequivocal evidence in favor of chemical exchange between various phosphate Q-species and aluminate species, while similar studies on ternary xLi_2O-(50-x) ZnO-$50P_2O_5$ metaphosphate liquids have indicated isotropic orientational averaging of the ^{31}P NMR chemical shift anisotropy (CSA) of the Q^2 phosphorus sites [8–10]. The authors of these studies related such processes to the P-O-P and P-O-Al bond scission-renewal dynamics and the corresponding timescale was shown to be consistent with τ_α in all liquids. However, the orientational averaging of the ^{31}P CSA in Q^2 chains in the metaphosphate liquids may also result from the segmental and/or rotational dynamics of these chains, without any P-O bond scission/renewal. However, an unequivocal distinction between the two possible dynamical scenarios of viscous flow in chain phosphate liquids remains to be made. In fact, the connection between viscosity and the motion of polymer

chains in dilute or concentrated solutions or in polymer melts is well established in the literature [15]. Thus, the reorientational motion of Q^2 chains may indeed dominate the viscous flow and structural relaxation in phosphate liquids with Q^2 chain lengths shorter than or equal to those characteristic of metaphosphate liquids with 50 mol% P_2O_5. In this chapter, the results of a variable temperature ^{31}P NMR spectroscopic study of the dynamical processes in a binary Ag_2O-P_2O_5 liquid with 51.5% Ag_2O are reported, in order to test this hypothesis. A liquid of this composition is expected to have ~94% Q^2 and 6% Q^1 species, which would imply an average chain length of 32.33 tetrahedra with the assumption that all Q^1 species terminate the Q^2 chains and do not participate in dimer formation.

4.3 Experimental Methods

4.3.1 Sample synthesis and characterization

The Ag-phosphate glass was prepared by the conventional melt-quenching method. The mixture of $NH_4H_2PO_4$ (99.9%, Acros Organics) and $AgNO_3$ (99.9%, Alfa Aesar) was loaded into a quartz crucible and was calcined at 623 K for 17 hours to remove any water and ammonia. Then the as-treated batch was melted at 873 K for 15 minutes and subsequently quenched by dipping the crucible in water. The as-made glass was stored in a desiccator to avoid exposure to atmospheric moisture. The chemical composition of this glass was determined via electron probe micro-analysis (Cameca SX-100) and the Ag_2O and P_2O_5 concentrations were found to be within ±0.2 mol% of their nominal values. The T_g of this glass was determined using differential scanning calorimetry (Mettler Toledo DSC1). Samples of mass ~20-30 mg were taken in hermetically sealed Al pans and were heated at a rate of 10 K/min. T_g was determined to within

±2 K to be 436 K as the onset of the glass transition endotherm. As expected, this T_g is somewhat lower than that (449 K) of the $AgPO_3$ metaphosphate glass reported in a previous study [14].

4.3.2 Viscosity measurement

The shear viscosity of the supercooled $51.5Ag_2O$-$48.5P_2O_5$ liquid was measured using a parallel plate rheometer (MCR302, Anton Paar USA) in an environment of flowing nitrogen gas. Before rheometry measurements, the glass sample was softened and trimmed between the plates to form a sandwich-like geometry with a thickness of ~1 mm. For viscosity up to ~10^7 Pa·s, a steady shear strain was applied at a fixed rate and the corresponding stress response was measured via the torque transducer through the upper plate (~8 mm diameter), which allowed the determination of viscosity η as the ratio of stress and strain rate. The details of the experimental setup for steady shear measurement can be found in a previous publication[16]. For viscosity higher than 10^8 Pa·s near glass transition, a creep test was carried out by applying a constant shear stress τ_{shear} until the creep compliance reached a steady state with a constant slope, corresponding to linear viscous response. This slope is equal to the strain rate $\dot{\gamma}$ and thus the viscosity was obtained from the relation: $\eta = \frac{\tau_{shear}}{\dot{\gamma}}$ [17].

4.3.3 ^{31}P NMR

The ^{31}P MAS spectra of the Ag-phosphate glass were collected at multiple spinning speeds using a Bruker Avance500 spectrometer operating at 11.74 T (^{31}P Larmor frequency 202.4 MHz) and a Bruker 4mm triple-resonance MAS probe. Crushed glass was packed in zirconia rotor and was spun at speeds ranging from 8 kHz to 12 kHz. The ^{31}P MAS spectra at all spinning speeds were collected using a single pulse with a pulse length of 1.4 μs (tip angle = 45 degree) and a

recycle delay of 15 s. Each spectrum was obtained by Fourier transforming an average of 32 free induction decays.

The high-temperature ^{31}P static NMR spectra of the supercooled Ag-phosphate liquid were acquired using the same magnet and spectrometer as noted above and a Bruker wideline probe. Crushed glass was packed and flame-sealed in an evacuated Pyrex ampoule and heated using nitrogen gas. Temperature of the probe was calibrated externally using the well-known temperature dependence of the ^{63}Cu chemical shift of CuBr[18]. The ^{31}P static spectra at all temperatures were collected using a single pulse with a pulse length of 2.5 μs (tip angle = 60 degree) The recycle delay was varied from a maximum of 15 s at room temperature and near the highest temperature of ~ 500 K to a minimum of 5 s near 430 K. Each spectrum was obtained by Fourier transforming the average of 32 free induction decays.

4.4 Results and Discussion

The MAS spectra of the Ag-phosphate glass collected at spinning speeds of 10 kHz and 12 kHz are shown in Fig. 4-1. These spectra display two isotropic resonances centered at isotropic shifts of −17.6 and −3.2 ppm and the corresponding spinning sidebands. These two resonances can be readily assigned, respectively, to the Q^2 and Q^1 phosphorus sites in the glass structure on the basis of their isotropic shifts as reported on similar phosphate glass compositions in previous studies [19,20]. These spectra are simulated simultaneously to obtain a consistent set of chemical shift tensor parameters for the Q^2 and Q^1 environments, as listed in Table 4-1. The relative ratio of these two Q-species (~ 92:8) is also consistent with that expected from the nominal composition of this glass, as has been noted above. These ^{31}P MAS NMR spectra also show the presence of a third weak resonance centered at 6.5 ppm with similar CSA parameters as the Q^1 environment.

The structural assignment of this resonance remains unclear at this stage. The isotropic chemical shift could correspond to either a Q^1 or a Q^0 species [19,21]. However, integration of the peak areas indicate that only ~ 1.5% P atoms reside in this environment. Hence, its effect on the high-temperature static NMR line shapes and consequently on the dynamics is expected to be negligible, and thus ignored in this chapter.

Table 4-1

^{31}P MAS NMR Line Shape Simulation Parameters for $51.5Ag_2O \cdot 48.5P_2O_5$ glass.

Peak No.	Relative Amplitude	Isotropic shift δ_{iso} (ppm)	Full width at half-maximum (± 0.5 ppm)	Reduced anisotropy δ (ppm) ± 5%	Asymmetry parameter η (± 0.05)
1	0.98	–17.60	9.50	–135.0	0.50
2	0.11	–3.16	8.03	–108.7	0.40
3	0.04	6.48	5.62	–108.7	0.50

The temperature dependent evolution of the ^{31}P static NMR line shape of the Ag-phosphate supercooled liquid at temperatures ranging between 293 and 513 K is shown in Fig. 4-2. The ^{31}P NMR spectra at the lowest temperatures between 293 and 453 K do not display significant change in the line shape, indicating that the frequency of the dynamics in this temperature range is significantly lower than the line-broadening effect associated with the CSA. Indeed, these line shapes can be simulated well with the chemical shift tensor parameters listed in Table 4-1, that were obtained from the simulation of the ^{31}P MAS NMR spectra (Fig. 4-3). As expected, the presence of ~8% of the Q^1 species is not immediately apparent from the broad static line shapes at low temperatures. However, its presence becomes apparent as the effect of line narrowing due to the dynamical averaging of the CSA becomes appreciable with increasing temperature and

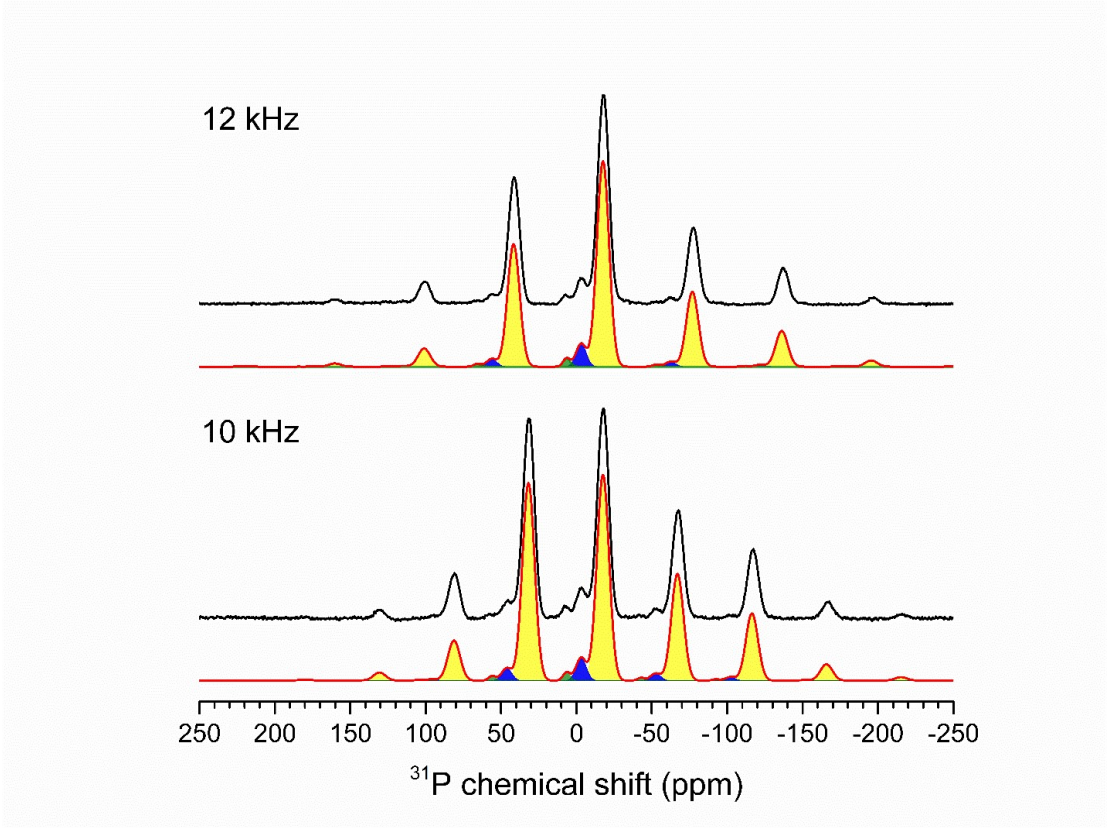

Figure 4-1 Simulations (red lines) of experimental (black lines) ^{31}P MAS NMR spectral line shapes of $51.5Ag_2O \cdot 48.5P_2O_5$ glass obtained at spinning speeds of 10 kHz (bottom) and 12 kHz (top). Also shown are the Gaussian simulation components corresponding to Q^2 (yellow), Q^1 (blue) and (likely) Q^0 species (green).

consequently the spectral resolution increases rapidly at the highest temperatures (Fig. 4-2). This result is also indicative of the clear absence of any chemical exchange between the two Q-species, which would require P-O bond scission and renewal. Such a process, if present, would have to be significantly slower than the separation frequency (~ 3 kHz) of the Q^2 and Q^1 resonances, even at the highest temperatures. Instead, the two resonances undergo line narrowing via individual averaging of their CSA. This result is a clear indication that the CSA averaging results from a rotational reorientation motion of the Q^2-chains as a whole. Additionally, with increasing temperature, the CSAs of both Q-species appear to average at a similar rate (Figs 4-2, 4-3). This observation is consistent with the hypothesis that the majority of the Q^1-species in this Ag-phosphate liquid indeed terminate the Q^2-chains rather than forming dimers.

In the absence of any motion, an NMR powder pattern for a specific structural moiety can be thought to consist of an infinite number of sharp resonances, each corresponding to a unique orientation of the moiety with respect to the external magnetic field. Various dynamical processes may result in the reorientation of these structural moieties, i.e. an orientational exchange, that can lead to an elimination of the orientation dependence of various line-broadening effects in the NMR spectra and consequent line narrowing. Therefore, the timescale of dynamical averaging of the ^{31}P CSA in the static NMR line shapes in Fig. 4-2 via rotation of Q^2-chains can be simulated using a model of orientational exchange. Here a random reorientational exchange model is used, where exchange between any pair of orientations is equally probable and, thus, for each Q-species all orientational exchange events are characterized by the same timescale. The analytic expression for the resulting line shape is given by the real part of *g(ω)*, where $g(\omega) = \frac{1}{N}\frac{L}{1-(L/\tau_{NMR})}$ and $L = \sum_{j=1,N}\left[i(\omega-\omega_j)+\frac{1}{T_{2j}}+N/\tau_{NMR}\right]^{-1}$ [22]. In these expressions N is the total number of

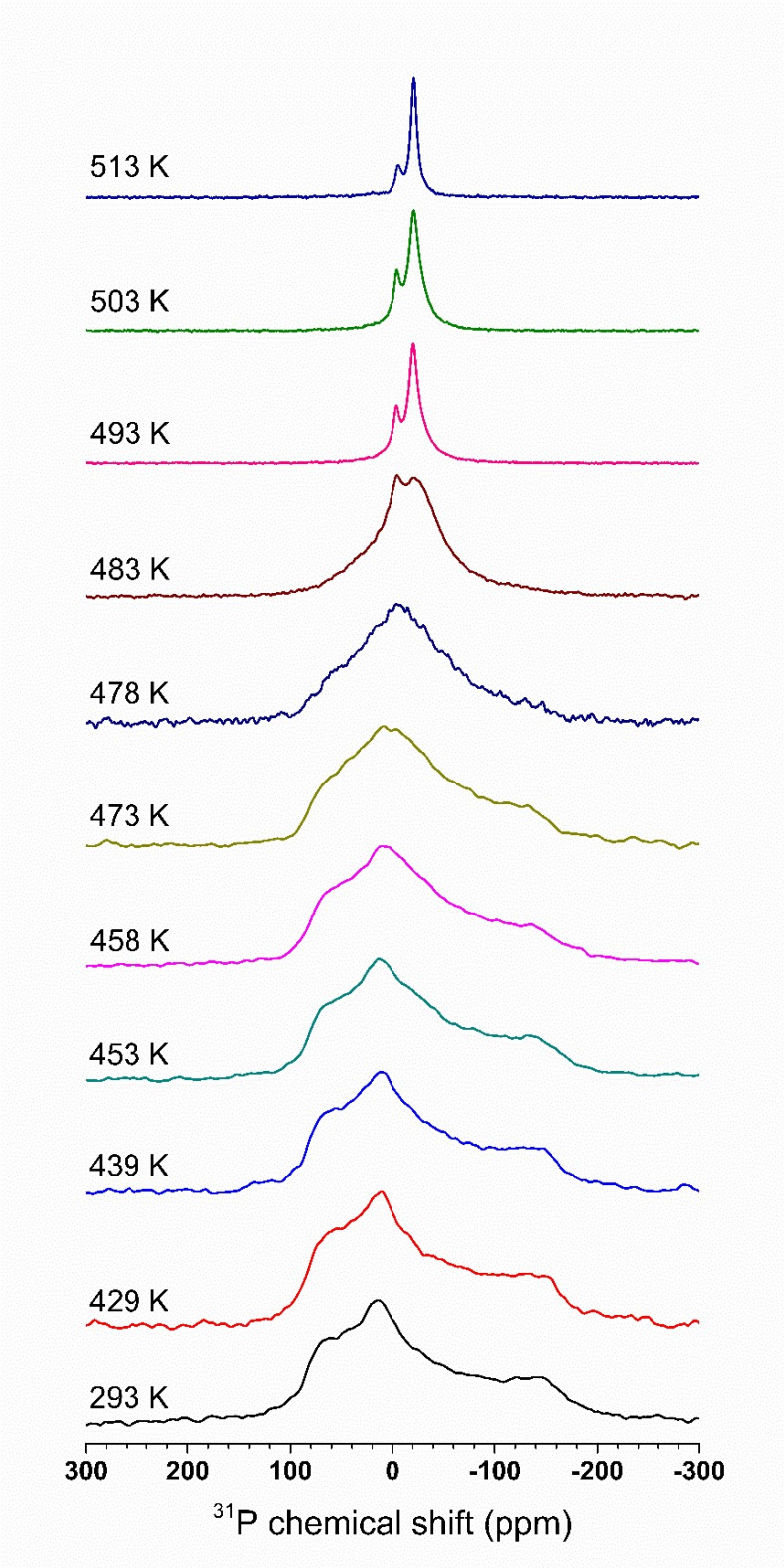

Figure 4-2 Variable-temperature ^{31}P NMR wideline spectra of $51.5Ag_2O{\cdot}48.5P_2O_5$ glass and supercooled liquid. Temperature is indicated alongside the spectra.

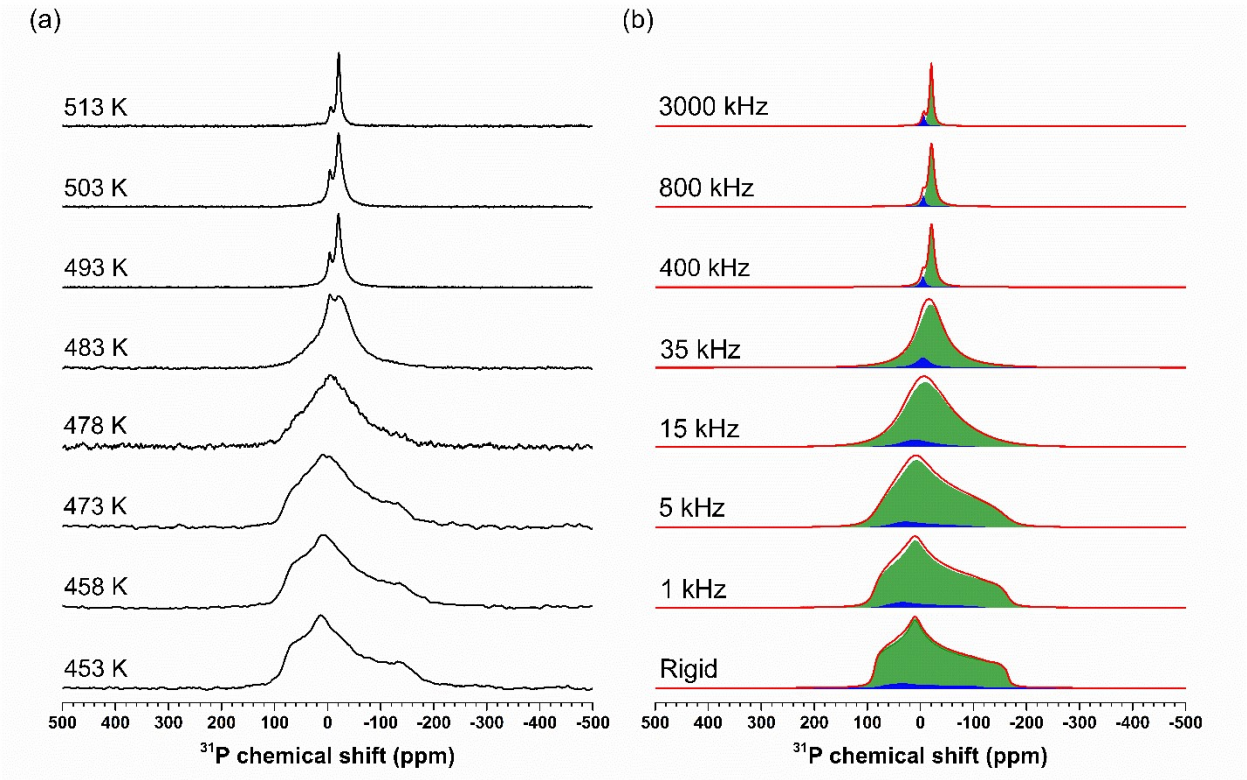

Figure 4-3 Comparison between ^{31}P NMR wideline spectra (left) and simulations using random reorientational exchange model (right). Simulated line shapes (red lines) are shown along with the Gaussian simulation components corresponding to Q^2 (green) and Q^1 (blue) species. Temperature and exchange frequencies are indicated alongside the spectra. For details of simulation see text.

orientations (taken to be 10^4 for the present simulations), ω_j is the frequency and T_{2j} is the reciprocal of the intrinsic linewidth corresponding to each orientation, and $(\tau_{NMR})^{-1}$ is the rate of exchange between any pair of orientations for either Q^2 or Q^1 species. The value of T_{2j} has been kept constant at 1 ms for all sites in all of the simulations and only τ_{NMR} is varied as a function of temperature. It is clear from Fig. 4-3 that this simple model of the orientational exchange via chain rotation is able to reproduce the experimental ^{31}P NMR line shapes of this supercooled Ag-phosphate liquid well. However, we also note that the simulation of these line shapes at the highest temperatures required the consideration of an increased relative fraction of the Q^1 species

from 8% (± 0.5%) to up to 12% (± 0.5%). This change in Q-speciation may be indicative of a temperature dependent disproportionation reaction in the melt.

The shear viscosity η of the Ag-phosphate liquid, measured using parallel-plate rheometry, is shown in Fig. 4-4a. The temperature dependence of the viscosity can be fitted to the Vogel-Fulcher-Tammann (VFT) equation: $log\,\eta(T) = A + \frac{B}{T-T_0}$, where $A = -1.35 \pm 0.34$, $B = 611.67 \pm 46.89$ and $T_0 = 388.41 \pm 2.39$ are material-dependent constants. The corresponding shear relaxation timescale τ_{shear} can be obtained from the viscosity data using the Maxwell relation: $\tau_{shear} = \eta/G_\infty$, where G_∞ is the high-frequency glassy shear modulus, taken to be a temperature-independent constant with a value of 10^{10} Pa, typical of a wide variety of oxide glass-forming liquids (Fig. 4-4b). The temperature dependence of the ^{31}P CSA averaging timescale τ_{NMR} is compared to τ_{shear} in Fig. 4-4b. The close agreement between τ_{NMR} and τ_{shear} readily indicates that indeed the rotational reorientation of the Q^2-chains is responsible for viscous flow of this short-chain phosphate liquid.

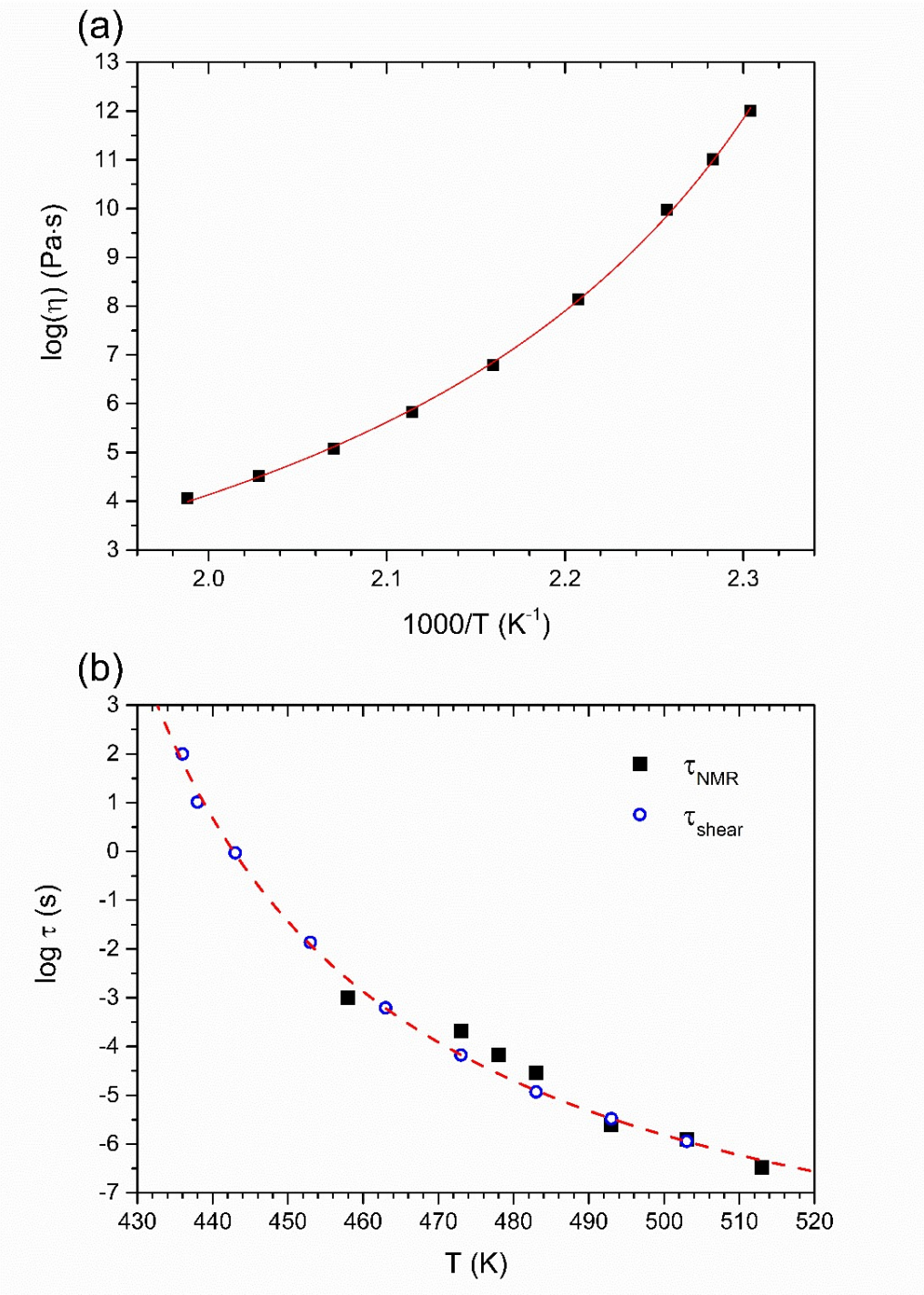

Figure 4-4 (a) Temperature dependence of viscosity of $51.5Ag_2O{\cdot}48.5P_2O_5$ liquid measured by parallel plate rheometry. Experimental uncertainties are within the size of the symbols. Solid line through data points correspond to least squares fit to the VFT equation. The viscosity at T_g is taken to be 10^{12} Pa·s. (b) Comparison between temperature dependence of ^{31}P CSA averaging timescale τ_{NMR} (black square) and shear relaxation timescale τ_{shear} (blue circle) for this liquid. Dashed line through data points is guide to eyes.

It is also instructive to compare the viscosity of the 51.5%Ag_2O-48.5% P_2O_5 liquid studied here with that of the $AgPO_3$ metaphosphate liquid (Fig. 4-5) reported in a previous study [14]. It is evident from Fig. 4-5 that the viscosity of the 51.5%Ag_2O-48.5% P_2O_5 liquid in this temperature range is lower than that of the $AgPO_3$ liquid by one to two orders of magnitude. Although the average chain length of the $AgPO_3$ liquid is not known a priori, typically the chain length of metaphosphate liquids are limited by the presence of water as an impurity which terminates the Q^2 chains via the cleaving of the P-O-P linkages. However, considering that previous ^{31}P MAS NMR spectroscopic studies of the $AgPO_3$ glass could not detect any Q^1 species and the detection limit of such species as evident in the MAS NMR spectra in Fig. 4-1 is ~1-2%, one can obtain a

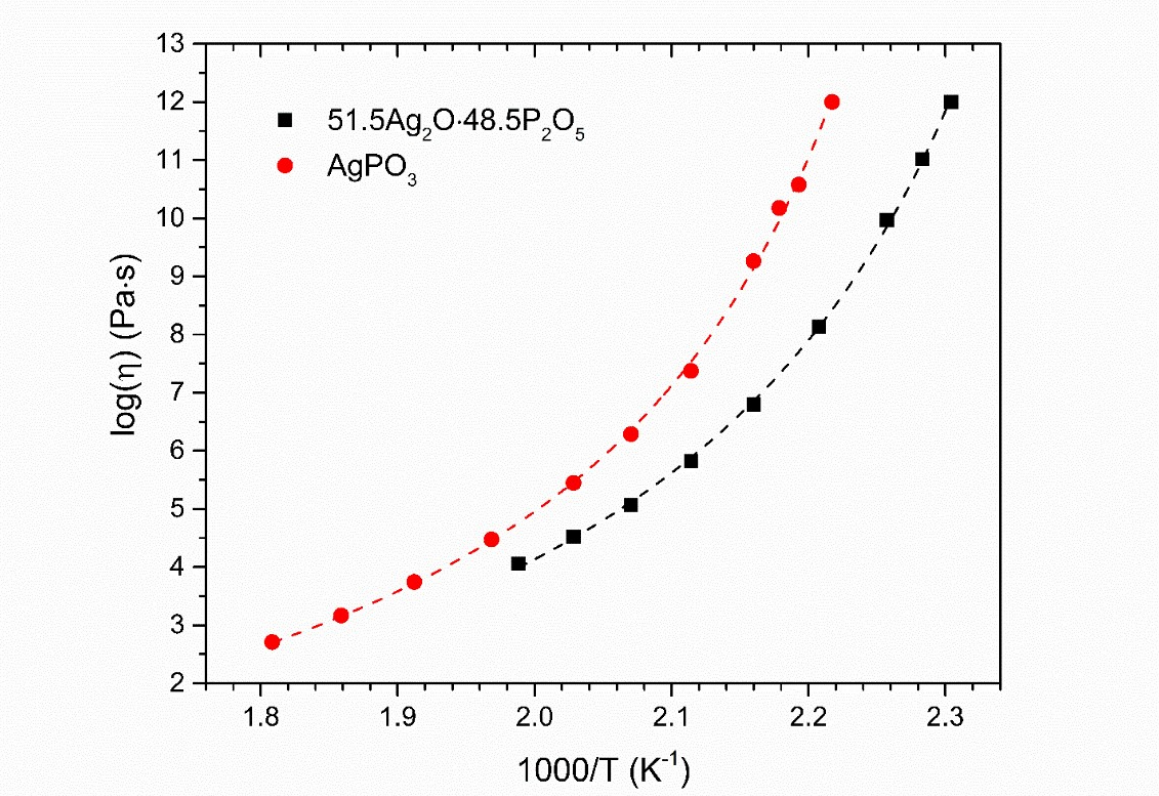

Figure 4-5 Comparison between temperature dependence of viscosity of $51.5Ag_2O{\cdot}48.5P_2O_5$ (black square) and $AgPO_3$ (red circle) liquids. Data for $AgPO_3$ liquid are taken from a previous study [14]. Experimental uncertainties are within the size of the symbols. Dashed lines through data correspond to least squares fits to the VFT equation. Viscosity at T_g is taken to be 10^{12} Pa·s.

minimum average chain length of ~ 100-200 tetrahedra for this liquid. Hence, the average chain length of the 51.5%Ag_2O-48.5% P_2O_5 liquid is at least a factor of ~3 to 6 lower than that of the $AgPO_3$ liquid. Thus, it appears that if the viscosity η of these liquids is a stronger-than-linear function of chain length. Such a strong dependence of viscosity on chain length is quite different from the linear dependence expected for the Rouse motion of short chain polymers, which is a single chain diffusion represented by spring-beads model [15]. Thus, it is possible that the chain length in metaphosphate liquids is large enough for reptation process to become relevant.

4.5 Conclusion

When taken together, the rheometric and ^{31}P NMR spectroscopic results reveal a remarkable agreement between the timescale of the rotational reorientation of the Q^2 chains and that of shear relaxation in the 51.5%Ag_2O-48.5% P_2O_5 liquid over several orders of magnitude. This agreement indicates that the chain reorientation process controls the viscous flow of this short-chain liquid. Moreover, unlike network oxide liquids, the bond scission/renewal dynamics and chemical exchange between different Q-species do not appear to control the shear relaxation in liquids containing low-dimensional structural elements. If present in the Ag-phosphate liquid, such a dynamical process would be characterized by a timescale that is several orders of magnitude slower than that of chain rotation, even at the highest temperatures of measurement. It will be interesting to investigate in future whether such dynamical transition associated with the dimensionality or connectivity of the network is a feature that is shared by other inorganic glass-forming systems.

References

[1] A. Cavagna, Supercooled Liquids for Pedestrians, Phys. Rep. 476 (2009) 51–124.

[2] G.N. Greaves, S. Sen, Inorganic glasses, glass-forming liquids and amorphizing solids, Adv. Phys. 56 (2007) 1–166.

[3] S. Sen, Dynamics in inorganic glass-forming liquids by NMR spectroscopy, Prog. Nucl. Magn. Reson. Spectrosc. 116 (2020) 155–176.

[4] I. Farnan, J.F. Stebbins, The nature of the glass transition in a silica-rich oxide melt, Science (80-.). 265 (1994) 1206–1209.

[5] J.F. Stebbins, S. Sen, I. Farnan, Silicate species exchange, viscosity, and crystallization in a low-silica melt: In situ high-temperature MAS NMR spectroscopy, 1995.

[6] J.F. Stebbins, S. Sen, Borate Glasses, Crystlas and Melts, in: A. Wright, S. Feller, A. Hannon (Eds.), 2nd Int. Conf., Society of Glass Technology, Sheffield, UK, 1997, n.d.

[7] J.F. Stebbins, NMR at High Temperature, in: P. Hodgkinson (Ed.), Mod. Methods Solid-State NMR A Pract. Guid., Royal Society of Chemistry, 2018, n.d.

[8] S. Wegner, L. Van Wu, G. Tricot, Network Dynamics and Species Exchange Processes in Aluminophosphate Glasses : An in situ High Temperature Magic Angle Spinning NMR View, J. Phys. Chem. B. 113 (2009) 416–425.

[9] L. Van Wüllen, H. Eckert, G. Schwering, Structure-property correlations in lithium phosphate glasses: New insights from 31P mutually implies 7Li double-resonance NMR, Chem. Mater. 12 (2000) 1840–1846.

[10] L. Muñoz-Senovilla, S. Venkatachalam, F. Muñoz, L. Van Wüllen, Relationships between fragility and structure through viscosity and high temperature NMR measurements in Li_2O-ZnO-P_2O_5 phosphate glasses, J. Non. Cryst. Solids. 428 (2015) 54–61.

[11] T.D. Tran, D.L. Sidebottom, Glass-forming dynamics of aluminophosphate melts studied by photon correlation spectroscopy, J. Am. Ceram. Soc. 96 (2013) 2147–2154.

[12] D.L. Sidebottom, D. Vu, Assessing the network connectivity of modifier ions in metaphosphate glass melts : A dynamic light scattering study of Na-Zn mixtures, J. Chem. Phys. 145 (2016) 164503.

[13] D.L. Sidebottom, T.D. Tran, S.E. Schnell, Building up a weaker network: The effect of intermediate range glass structure on liquid fragility, J. Non. Cryst. Solids. 402 (2014) 16–20.

[14] Y. Xia, W. Zhu, M. Lockhart, B. Aitken, S. Sen, Fragility and rheological behavior of metaphosphate liquids : Insights into their chain vs . network characters, J. Non. Cryst. Solids. 514 (2019) 77–82.

[15] M. Doi, S.F. Edwards, Theory of Polymer Dynamics, Clarendon Press, Oxford, 1986.

[16] S. Sen, W. Zhu, B.G. Aitken, Behavior of a supercooled chalcogenide liquid in the non-Newtonian regime under steady vs . oscillatory shear, J. Chem. Phys. 147 (2017) 034508.

[17] D.J. Plazek, Magnetic bearing torsional creep apparatus, J. Polym. Sci. Part A-2. 6 (1968)

621–638.

[18] S. Hayashi, K. Hayamizu, Nuclear magnetic resonance chemical shifts in alkali iodides, cuprous halides and silver halides, J. Phys. Chem. Solids. 53 (1992) 239–248.

[19] R.K. Brow, R.J. Kirkpatrick, G.L. Turner, The short range structure of sodium phosphate glasses I. MAS NMR studies, J. Non. Cryst. Solids. 116 (1990) 39–45.

[20] R.K. Brow, Review: the structure of simple phosphate glasses, J. Non. Cryst. Solids. 263&264 (2000) 1–28.

[21] M. Villa, G. Chiodelli, M. Scagliotti, P2O5 based vitreous electrolytes: Structural characterization by 31P NMR and Raman spectroscopies, Solid State Ionics. 18–19 (1986) 382–387.

[22] M. Mehring, Principles of high resolution NMR in solids, Springer Science & Business Media., 2012.

Chapter 5

Rheological Characterization of Complex Dynamics in Na-Zn Metaphosphate Glass-Forming Liquids

5.1 Abstract

The viscoelastic behavior and shear relaxation in supercooled $[NaPO_3]_x[Zn(PO_3)_2]_{1-x}$ metaphosphate liquids with $0.2 \leq x \leq 1.0$ are investigated using a combination of small amplitude oscillatory and steady shear parallel plate rheometry, resonant ultrasound spectroscopy and differential scanning calorimetry. The results demonstrate that these liquids are thermorheologically complex with the coexistence of a fast and slow relaxation process in these liquids, which could be attributed to the segmental motion of the phosphate chains and the P−O bond scission/renewal dynamics, respectively. The segmental motion of the phosphate chains is found to be the dominant process associated with the shear relaxation for all metaphosphate liquids. The compositional evolution of the calorimetric fragility of these liquids is shown to be related to the conformational entropy of the constituent phosphate chains that is manifested in the width of the relaxation time distribution for the segmental chain motion. This entropy decreases and the temporal coupling between the chain dynamics and P-O bond scission-renewal increases with increasing Zn content as, compared to the low field strength Na modifiers, the high field strength Zn ions provide stronger effective cross-linking between the phosphate chains.

5.2 Introduction

The technological importance of phosphate glasses originates primarily from their unique properties including large composition range for glass formation, low glass transition temperature T_g, large solubility of rare earth and other high-field strength cations, high thermal expansion coefficient and strong bioactivity [1–9]. Consequently, the atomic structure-property relationships in these glasses have been investigated in detail over the last decades [10–15]. However, in comparison, relatively little is known regarding the structural control on the viscoelastic behavior of the parent supercooled liquids from which these glasses are derived. The viscoelastic behavior of a supercooled glass-forming liquid is intimately linked to the material's viability for all stages of industrial processing including melting, forming and annealing and therefore, is of key significance in the optimization of corresponding processing parameters [16].

Analyses of the temperature-dependent viscosity data $\eta(T)$ of alkali phosphate liquids with ≥ 50 mol% P_2O_5 available in the literature has shown that the fragility index $m = \left.\frac{d\log\eta(T)}{d(T_g/T)}\right|_{T=T_g}$ is a sensitive function of the structural connectivity <n> of the phosphate network, where <n> is defined as the average number of bridging oxygen per PO_4 tetrahedron in the glass structure, which varies from 2 in metaphosphates with 50% P_2O_5 to 3 in pure P_2O_5 [17,18]. The phosphate network of alkali metaphosphate liquids is characterized predominantly by chains of corner-sharing PO_4 tetrahedra and the high conformational entropy of these chains is believed to be responsible for the relatively high fragility (m ~ 80) of these liquids [9]. As <n> increases on progressive addition of P_2O_5, these chains get increasingly cross-linked and the conformational entropy of the network decreases with a concomitant lowering of m. Finally, m reaches its minimum value of ~ 20 as <n> becomes 3 for pure P_2O_5. Strong similarity in the variation in m with <n> among different alkali

phosphate liquids suggests that shear relaxation and viscous flow in these liquids are primarily controlled by the phosphate network, which is only weakly coupled to the modifier ions. On the other hand, recent studies have shown that *m* can vary over a rather large range spanning from ~ 30 to 90 even in metaphosphate liquids with the same nominal connectivity of the phosphate network, as a function of the field strength of the modifier cation [19,20]. Metaphosphates with high field strength modifier cations such as alkaline-earth and Zn are characterized by low *m*, while those with low-field strength modifiers such as alkalis and Ag are characterized by rather large *m*. This variation was hypothesized to be related to the fact that the extent and the strength of the effective crosslinking of the phosphate chains by the modifier cation-oxygen polyhedra in the structure of metaphosphate liquids increases with increasing field strength of the modifiers [19]. Such a role of the modifier cation in controlling the fragility of metaphosphates can be clearly evidenced in the variation of *m* along the Na-Zn metaphosphate join, where *m* decreases monotonically from ~70 for the Na-metaphosphate to ~28 for the Zn-metaphosphate [21].

In Chapter 4, the rheological and variable-temperature ^{31}P magic-angle-spinning nuclear magnetic resonance (MAS NMR) spectroscopic studies have indicated that, similar to the low molecular weight chain polymers, the viscous flow and shear relaxation of highly fragile Ag-metaphosphate liquid is closely associated with the segmental motion of constituent phosphate chains [22]. Additionally, this liquid was found to be thermorheologically complex, violating the time-temperature superposition. In contrast, the shear relaxation of phosphate networks with higher degree of connectivity such as ultraphosphates appear to be controlled by the chemical exchange between the constituent PO_4 species via P-O bond scission-renewal dynamics [23,24]. Interestingly, an analogous transition from fragile liquids with shear relaxation controlled by segmental Se chain motion to strong liquids with relaxation predominantly controlled by bond

scission-renewal dynamics was observed in binary As-Se liquids with progressive addition of As to Se and associated cross-linking of Se chains [25,26]. However, it remains to be seen whether a similar transition in the shear relaxation mechanism can also be observed in metaphosphate liquids with progressive increase in the effective crosslinking of the phosphate chains as a low field strength modifier cation (e.g. Na) is replaced by a high field strength one (e.g. Zn) [19,27]. In this chapter, the results of a detailed rheological study of the viscoelastic properties and the shear relaxation behavior of $[NaPO_3]_x[Zn(PO_3)_2]_{1-x}$ supercooled liquids with varying Na:Zn ratios using a combination of small amplitude oscillatory shear (SAOS) and calorimetric measurements are reported. The relationships between fragility, structure and the various relaxational modes and their timescale distributions in these liquids are established.

5.3 Experimental Methods

5.3.1 Sample preparation and physical characterization

The $[NaPO_3]_x[Zn(PO_3)_2]_{1-x}$ metaphosphate glasses were prepared by conventional melt-quenching method. Appropriate amounts of $NH_4H_2PO_4$ (99.9%, Acros Organics), Na_2CO_3 (ACS grade, MilliporeSigma) and ZnO (99.99%, Alfa Aesar) were mixed and loaded in a quartz crucible. The mixtures were first calcined at 450°C for 17h to remove any water and ammonia. Subsequently, the calcined batches were melted at 1100°C for 1h. These melts were then quenched onto a graphite plate. Resulting glass samples were immediately transferred into a desiccator for storage to avoid exposure to atmospheric moisture.

The T_g of these Na-Zn metaphosphate glasses was determined using differential scanning calorimetry (Mettler Toledo DSC1). Samples of mass ~15-25 mg were taken in hermetically sealed Al pans and heated at a rate of 10 K/min in a flowing nitrogen environment above T_g to

remove thermal history. The fictive temperature T_f was taken as the peak of the endothermic glass transition signal while heating the sample at a specific rate q K/min ranging from 0.5 K/min to 30 K/min, subsequent to cooling at the same rate from T_g+30 K to T_g−50 K. T_g was determined to within ± 2 °C as the onset of the glass transition endotherm at a heating rate of 10 K/min. The fictive temperature T_f of $[NaPO_3]_x[Zn(PO_3)_2]_{1-x}$ liquids was determined as a function of the heating rate q varying from 0.5 K/min to 30 K/min, following the method of Wei et al. and the fragility index m was subsequently determined from the activation energy E of enthalpy relaxation according to the relation $m = \frac{E}{RT_g \ln 10}$ [28,29].

Density of these glasses was measured using a gas expansion pycnometer (Micromeritics AccuPyc II 1340) at 20°C using helium (6N purity) as the displacement gas. For each measurement, approximately 0.5 g of glass sample was loaded into a 1 cm^3 cup. All reported density values are averages of 10 consecutive measurements of each sample. The shear modulus of these samples was determined at room temperature using a Resonant Ultrasound Spectrometer (ACE-RUS008). The resonant ultrasound spectroscopy (RUS) technique uses the free-body mechanical resonances of ~ mm sized samples to determine their complete elastic modulus matrix. Each glass sample was cut into a rectangular parallelepiped geometry (~ 7mm x 5mm x 3mm) and the surfaces were polished flat and parallel. The as-prepared sample was mounted on opposing corners between two piezoelectric transducers. In the RUS system, an elastic wave of constant amplitude and varying sweeping frequency is generated by the drive transducer and the corresponding resonances are measured by the pickup transducer. The resonant frequency spectra in the frequency range between 50 kHz and 400 kHz were measured. The resonances were subsequently fitted to Lorentzian peaks and the RUS frequency data were analyzed using the Lagrangian minimization

code developed at the Los Alamos National Laboratory in conjunction with the mass density of the sample to obtain the elastic moduli. More details on the RUS experiments and data analysis can be found in literature [30,31].

5.3.2 Parallel plate rheometry

The viscoelastic behavior of the $[NaPO_3]_x[Zn(PO_3)_2]_{1-x}$ metaphosphate liquids were measured using a parallel plate rheometer (MCR 302, Anton-Paar) under oscillatory shear mode in an environment of flowing nitrogen gas, respectively. In this rheometer, the temperature was controlled by a convection oven. Before the rheometry measurements the glass samples were heated above the softening point to reach a viscosity of ~10^5 Pa·s and trimmed between the two plates to form a sandwich-like geometry with a gap of ~ 1 mm. At each desired measurement temperature, the samples were allowed to equilibrate for 5 minutes followed by the application of a sinusoidal strain with varying angular frequency ω between 1 to 628 rad/s and the induced torque was recorded to calculate the storage and loss moduli G′and G″ as a function of ω. The upper plate (8 mm diameter, stainless steel) was used to apply the sinusoidal strain while the non-removable lower plate (25 mm diameter, stainless steel) remained stationary. The corresponding stress response was recorded using a torque transducer. The applied strain of all oscillatory shear measurements was controlled within a predetermined linear viscoelastic region. Master curves of G' and G'' were obtained using time-temperature superposition (TTS). The systematic errors for G' and G'', introduced by the torsional instrument compliance was considered and corrected using the following equations [32]:

$$G_c' = \frac{G_m'\left(1-\frac{J_i}{k_g}G_m'\right)-\frac{J_i}{k_g}G_m''^{\,2}}{\left(1-\frac{J_i}{k_g}G_m'\right)^2+\left(\frac{J_i}{k_g}G_m''\right)^2} \qquad (1)$$

$$G_c'' = \frac{G_m''}{\left(1-\frac{J_i}{k_g}G_m'\right)^2+\left(\frac{J_i}{k_g}G_m''\right)^2} \qquad (2)$$

G_c' and G_c'' denotes the corrected storage modulus and loss modulus values while G_m' and G_m'' are the measured values. J_i is the torsional instrument compliance and k_g is the geometry factor given by $k_g = \frac{2h}{\pi R^4}$ where h is the sample thickness and R is the plate radius (4 mm). The instrument compliance of the rheometer setup was measured by the gluing method where the upper (8 mm, stainless steel) and lower plates (25 mm, stainless steel) were fixed together with a very thin layer (<20 μm) of cyanoacrylate glue [33]. After 24h drying time, a torque sweep was carried out to measure the corresponding deflection angle and the slope of the corresponding linear relationship was used to determine the instrument compliance J_i to be 0.000715 rad/Nm. All reported storage shear modulus G' and loss shear modulus G'' in this chapter are corrected values. The Newtonian viscosity of the $[NaPO_3]_{0.8}[Zn(PO_3)_2]_{0.2}$ liquid in the range ~ 10^5-10^8 Pa.s was measured using steady shear, where the viscosity was determined as the ratio of stress and strain rate at various shear rates $\dot{\gamma}$ ranging between 0.01 s^{-1} and 1 s^{-1} at each temperature.

5.4 Results and Discussion

The T_g of the $[NaPO_3]_x[Zn(PO_3)_2]_{1-x}$ metaphosphate glasses measured in this chapter display a nonlinear compositional variation as it steeply decreases with the initial replacement of Zn with Na as x increases from 0 to 0.2 beyond which a more gradual linear decrease is observed for $0.2 \leq x \leq 1.0$ (Fig. 5-1). Such a variation is consistent with the expectation that the lower field strength of the Na cations compared to that of Zn would result in weaker effective cross-linking of the constituent phosphate chains. In this scenario the sharp drop in T_g with the initial addition of Na to up to x = 0.2 is likely indicative of the percolation of these weakly linked regions in the glass

structure. The increasingly weaker interchain coupling upon progressive replacement of Zn with Na in these metaphosphate glasses is also evident in their compositional variation of the shear modulus *G*, which displays a sharp drop from ~19 GPa to ~ 7 GPa as x increases from 0 to 0.6 (Fig. 5-2). Further increase in Na content results in negligible change in *G*. On the other hand, the molar volume of these $[NaPO_3]_x[Zn(PO_3)_2]_{1-x}$ glasses decreases in a linear fashion with x over the entire composition range implying a corresponding increase in the atomic packing (Fig. 5-3). The highest molar volume of the $Zn(PO_3)_2$ glass may be indicative of an open tetrahedral network of corner shared ZnO_4 and PO_4 tetrahedra.

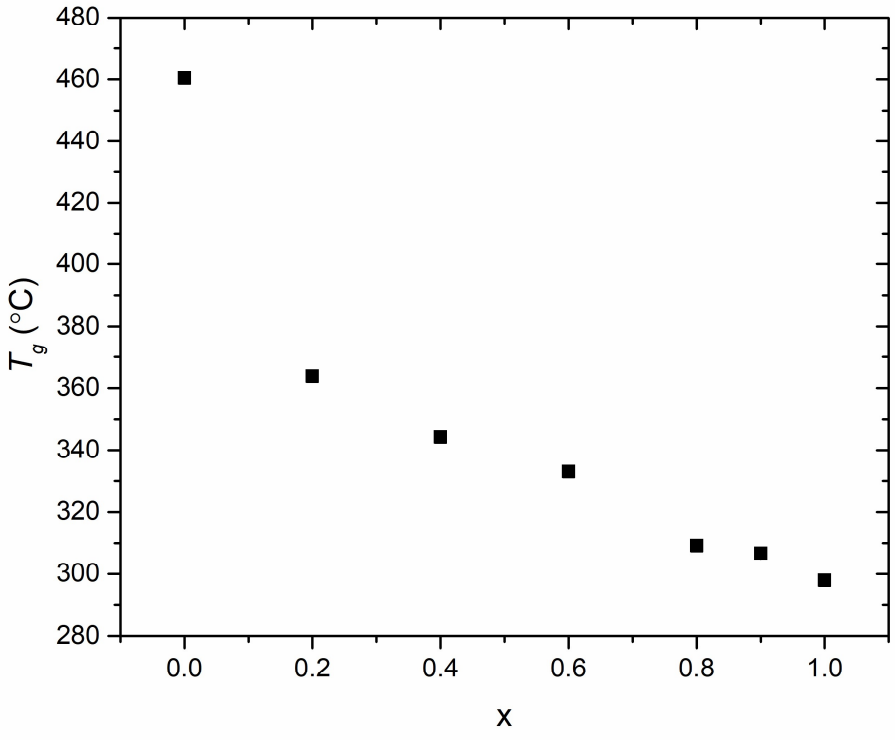

Figure 5-1 Glass transition temperature of $[NaPO_3]_x[Zn(PO_3)_2]_{1-x}$ glasses obtained in this dissertation. Experimental uncertainties are within the size of the symbols.

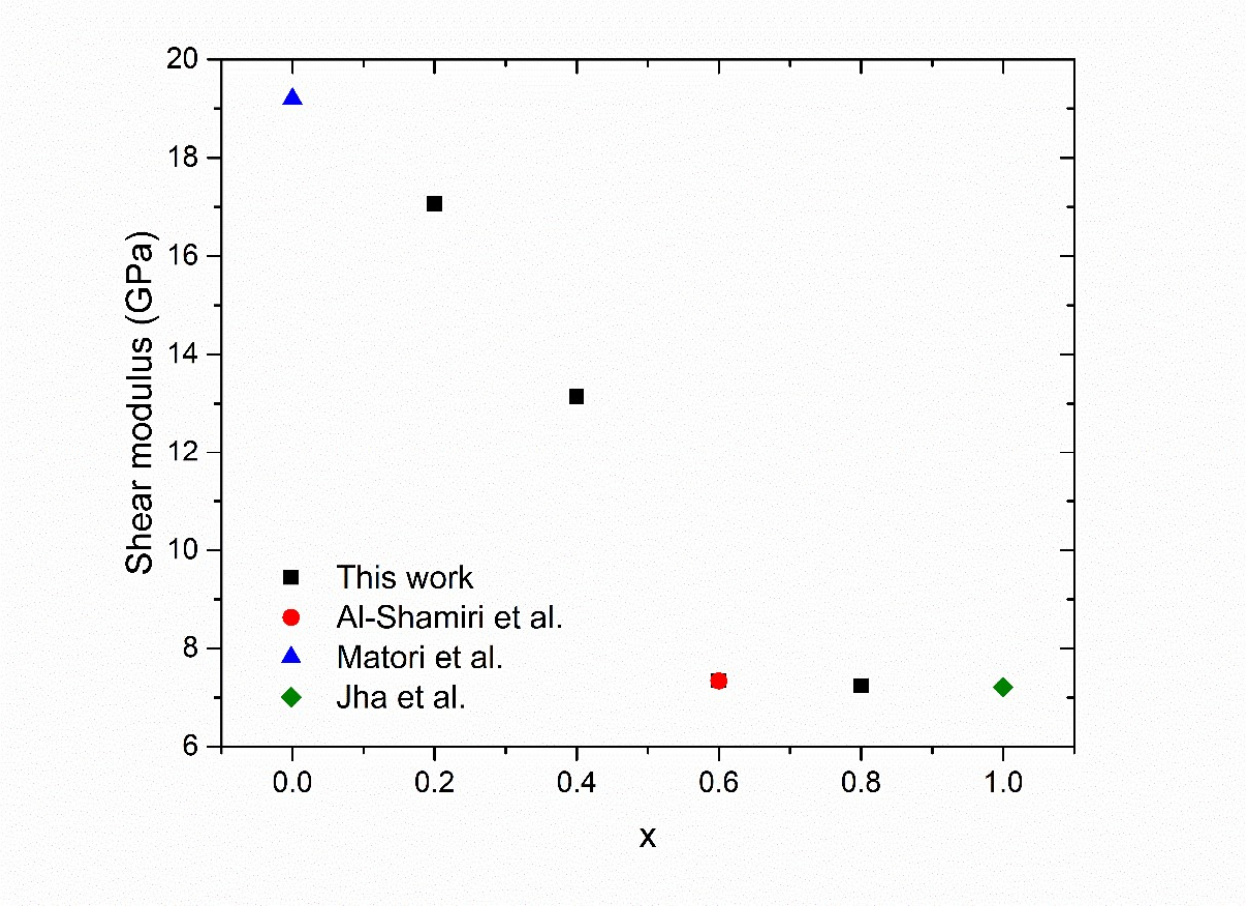

Figure 5-2 Shear modulus of $[NaPO_3]_x[Zn(PO_3)_2]_{1-x}$ glasses measured in the present study (black squares). Results reported by Al-Shamiri *et al.* [43] (red circle), Matori *et al.* [44] (blue triangle) and Jha *et al.* [45] (green diamond) are shown for comparison. Experimental uncertainties are within the size of the symbols.

The master plots of the angular frequency ω dependence of the storage modulus G' and the loss modulus G'' of all $[NaPO_3]_x[Zn(PO_3)_2]_{1-x}$ supercooled liquids investigated in this study obtained by performing TTS at an iso-viscous (~10^7 Pa·s) temperature are shown in Fig. 5-4. Although TTS is not strictly obeyed by these liquids (see below), here I have approximated TTS solely for the convenience of visualization of the data over the entire frequency range, and therefore, the master curves shown in Fig. 5-4 should be treated as only "approximate". It can be observed that in the low frequency viscous regime G' and G'' follow Maxwell scaling of ~ ω^2 and ~ ω respectively, while with increasing ω beyond the G'- G''crossover the storage modulus G'

reaches the glassy plateau value of G_∞ (~10 GPa) and G'' decreases. The G_∞ values of these liquids thus obtained are found to be consistent with the shear modulus of the corresponding glasses determined at ambient temperature by RUS measurements, which validates the torsional instrument compliance correction methodology adopted in this chapter. Perhaps most interestingly the frequency dependence of storage modulus $G'(\omega)$ changes from Maxwell scaling of $\sim \omega^2$ in the terminal regime to a nearly linear scaling of $\sim \omega^1$, which continues until the crossover of G' and G''. Such a scaling behavior has been reported in the literature for several supramolecular polymeric liquids that consist of short chains of a few molecules, as well as for As-Se and Ag-

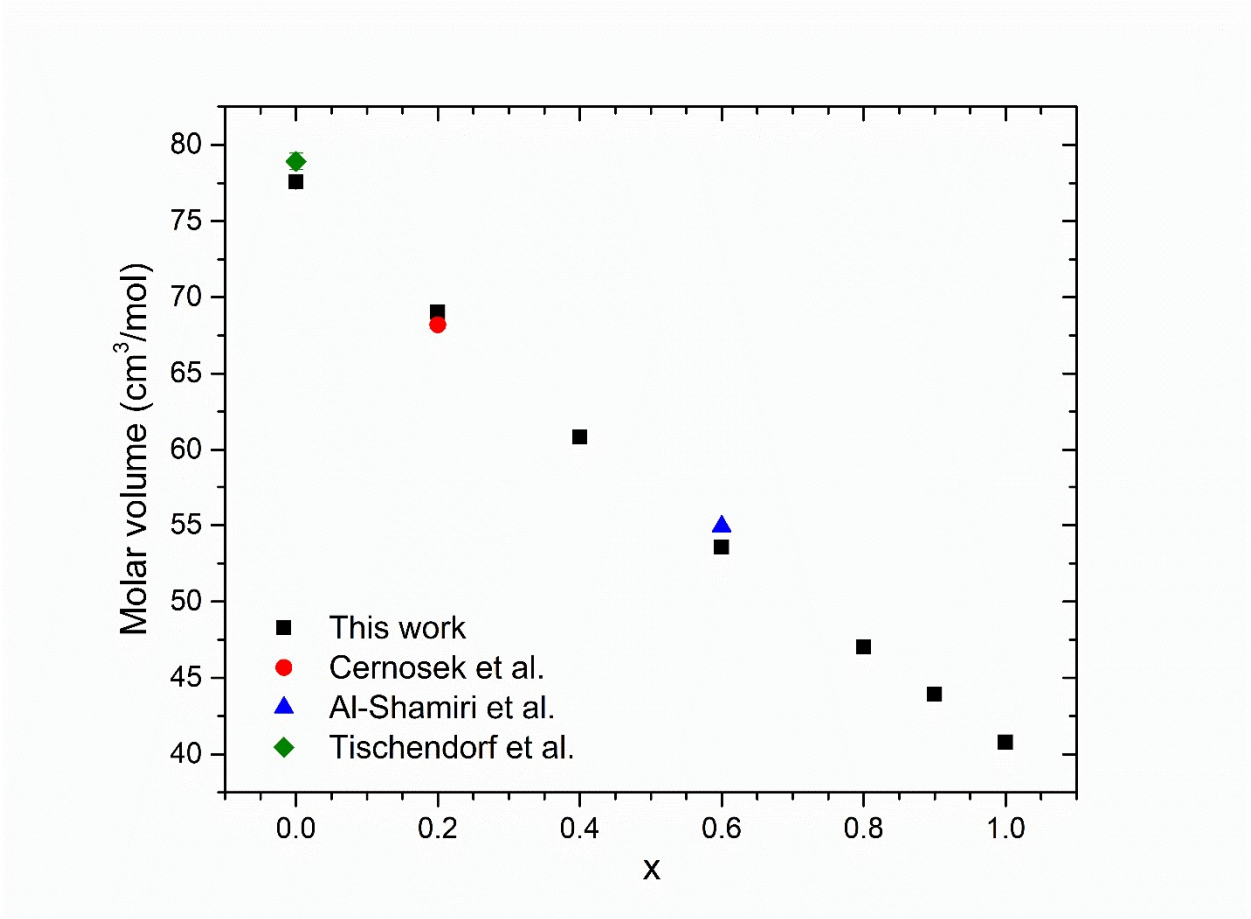

Figure 5-3 Molar volume of $[NaPO_3]_x[Zn(PO_3)_2]_{1-x}$ glasses measured in the present study (black squares). Results reported by Černošek *et al.* [46] (red circle), Al-Shamiri *et al.* [43] (blue triangle) and Tischendorf *et al.* [47] (green diamond) are shown for comparison. Experimental uncertainties are within the size of the symbols.

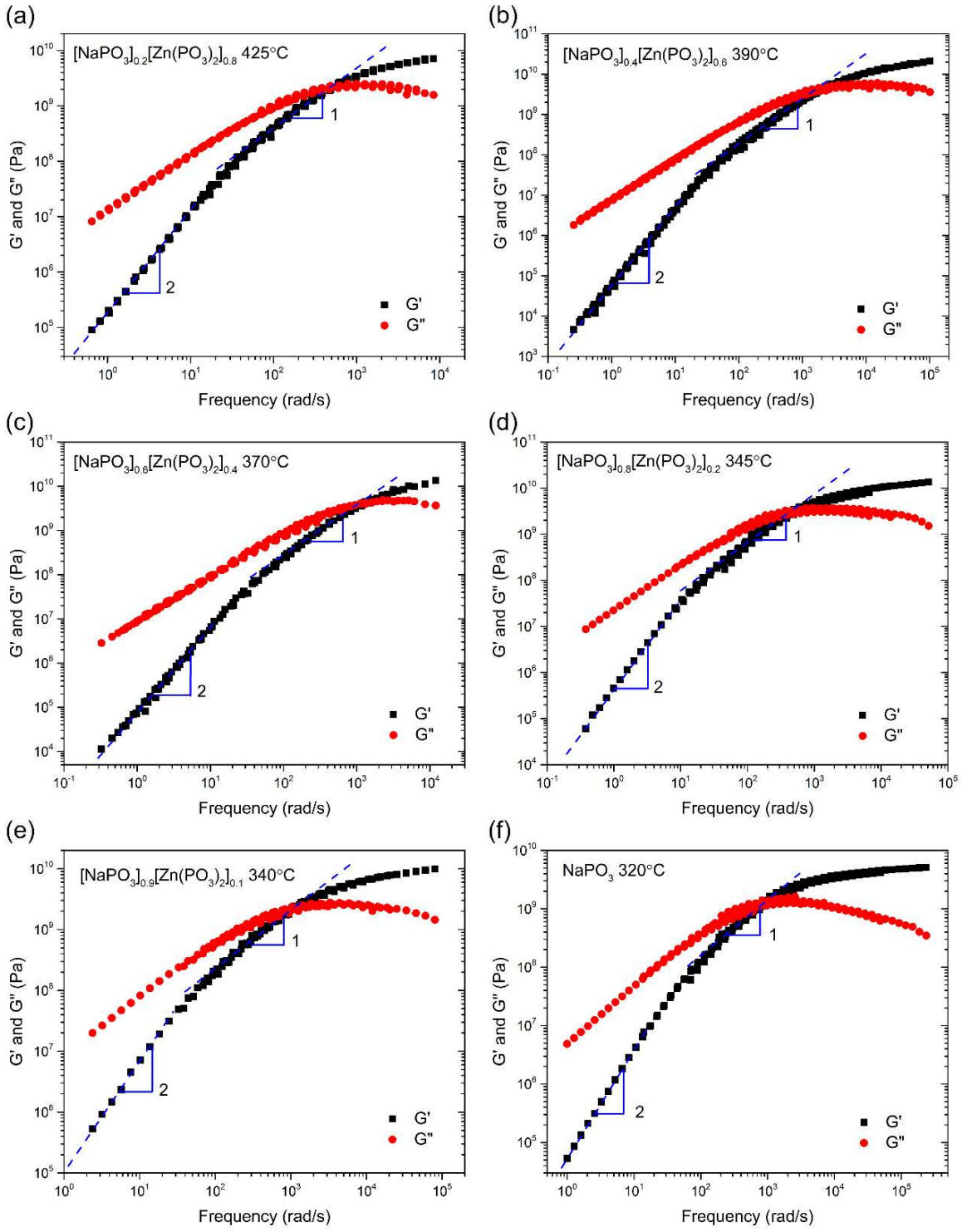

Figure 5-4 Master plots of angular frequency dependence of storage modulus G' (black squares), and loss modulus G'' (red circles) for $[NaPO_3]_x[Zn(PO_3)_2]_{1-x}$ liquids. The TTS reference temperature is listed alongside each composition. Blue dashed lines show frequency scaling of G' changing from $\sim \omega^2$ in low frequency region to $\sim \omega^1$ at higher frequencies.

metaphosphate liquids with short Se or phosphate chains, respectively, and hence, can be ascribed to the chain reorientation dynamics in these liquids [19,26,34,35]. Further insights into the viscoelastic relaxation process in these Na-Zn metaphosphate liquids can be obtained from the van Gurp-Palmen (vGP) plot (Fig. 5-5) of the phase angle $\delta = \tan^{-1}(G''/G')$ vs. the absolute value of complex modulus $|G^*| = \sqrt{G'^2 + G''^2}$, at various temperatures [36]. If a glass-forming liquid is strictly thermorheologically simple, the vGP plots at different temperatures are expected to overlap with each other to form a single curve. It is clear from Fig. 5-5 that such thermorheological simplicity is violated for all $[NaPO_3]_x[Zn(PO_3)_2]_{1-x}$ supercooled liquids in the dissertation, which is indicative of the existence of multiple relaxation processes with different activation energies. As noted above, at least two major dynamical processes have been associated in the past with the relaxation of a metaphosphate liquid, one of which is a reorientation or a segmental motion of the constituent chains and the other involves P-O bond scission/renewal. This scenario is then consistent with the observed violation of thermorheological simplicity in the Na-Zn metaphosphate liquids. Also, it is apparent from Fig. 5-5 that the degree of this violation i.e. the degree of thermorheological complexity increases with increasing Na:Zn ratio in these liquids. In Zn-rich compositions the high degree of thermorheological simplicity is the manifestation of a strong inter-chain cross-linking imparted by the high field strength Zn cations, which results in a mechanistic coupling between the chain motion and the P-O bond scission/renewal, with both processes likely being characterized by similar activation energies. On the other hand, with increasing Na:Zn ratio, the metaphosphate chains become less dynamically constrained and can perform facile segmental motion without the assistance from P-O bond scission/renewal in these liquids. Consequently, the two relaxation processes become decoupled with different activation energies, which gives rise to the observed enhancement in thermorheological complexity in Na-rich compositions. In the

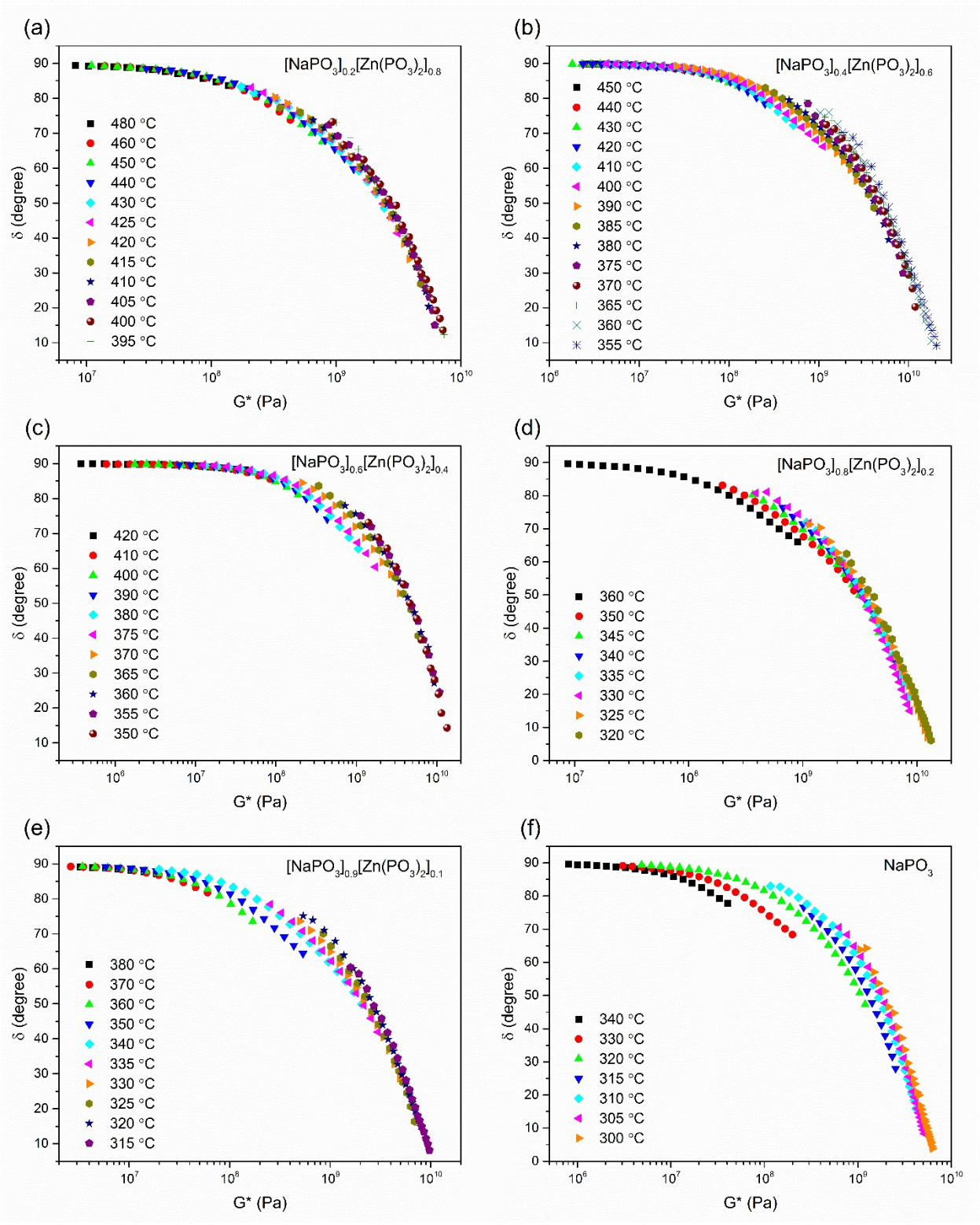

Figure 5-5 The van Gurp-Palmen plot of phase angle δ versus G^* for $[NaPO_3]_x[Zn(PO_3)_2]_{1-x}$ liquids.

extreme case of Na-metaphosphate, the PO_4 tetrahedral chains are the least constrained and Na ions are strongly decoupled from the structural network. This scenario is corroborated by the fact that the ionic conductivity for $NaPO_3$ glass is over four orders of magnitude higher than that of the $Zn(PO_3)_2$ glass near T_g [21], which suggests a significantly weaker coupling between the modifier cation and the phosphate network in the former compared that in the latter.

This hypothesis is further vindicated by the relaxation time spectra $H(\tau)$ of these Na-Zn metaphosphate supercooled liquids (Fig. 5-6) that were be calculated from the collected storage modulus $G'(\omega)$ data using the following relation proposed by Ninomiya and Ferry [37]:

$$H(\tau) = \frac{G'(a\omega)-G'(\omega/a)}{2\ln a} - \frac{a^2}{(a^2-1)^2}\frac{G'(a^2\omega)-G'(\omega/a^2)-2G'(a\omega)+2G'(\omega/a)}{2\ln a}\Big|_{1/\omega=\tau} \quad (3)$$

where a is the frequency interval on a logarithmic frequency scale of the measured $G'(\omega)$ values. As expected from the observed thermorheological complexity in the vGP plots (Fig. 5-5), the relaxation spectra $H(\tau)$ of all liquids can be simulated with two Gaussian peaks corresponding to two relaxation processes with overlapping timescale distributions (Fig. 5-6). Following the previously reported analyses of the $H(\tau)$ spectra of Se-rich As-Se and P-Se liquids [40,41], the broad and intense peak at short timescale in Fig. 5-6 is assigned to the segmental motion of the PO_4 tetrahedral chains, while the weak and narrow peak at long timescale is ascribed to the P–O bond scission/renewal dynamics. As the relative peak intensity is determined by the probability of the relaxation mechanism, the relatively strong intensity of the broad peak in Fig. 5-6 reflects the predominance of the segmental motion of phosphate chains in controlling the viscous flow and shear relaxation of metaphosphate liquids, which increases upon progressive replacement of Zn with Na in the metaphosphate structure [22]. This result is consistent with the hypothesis that the

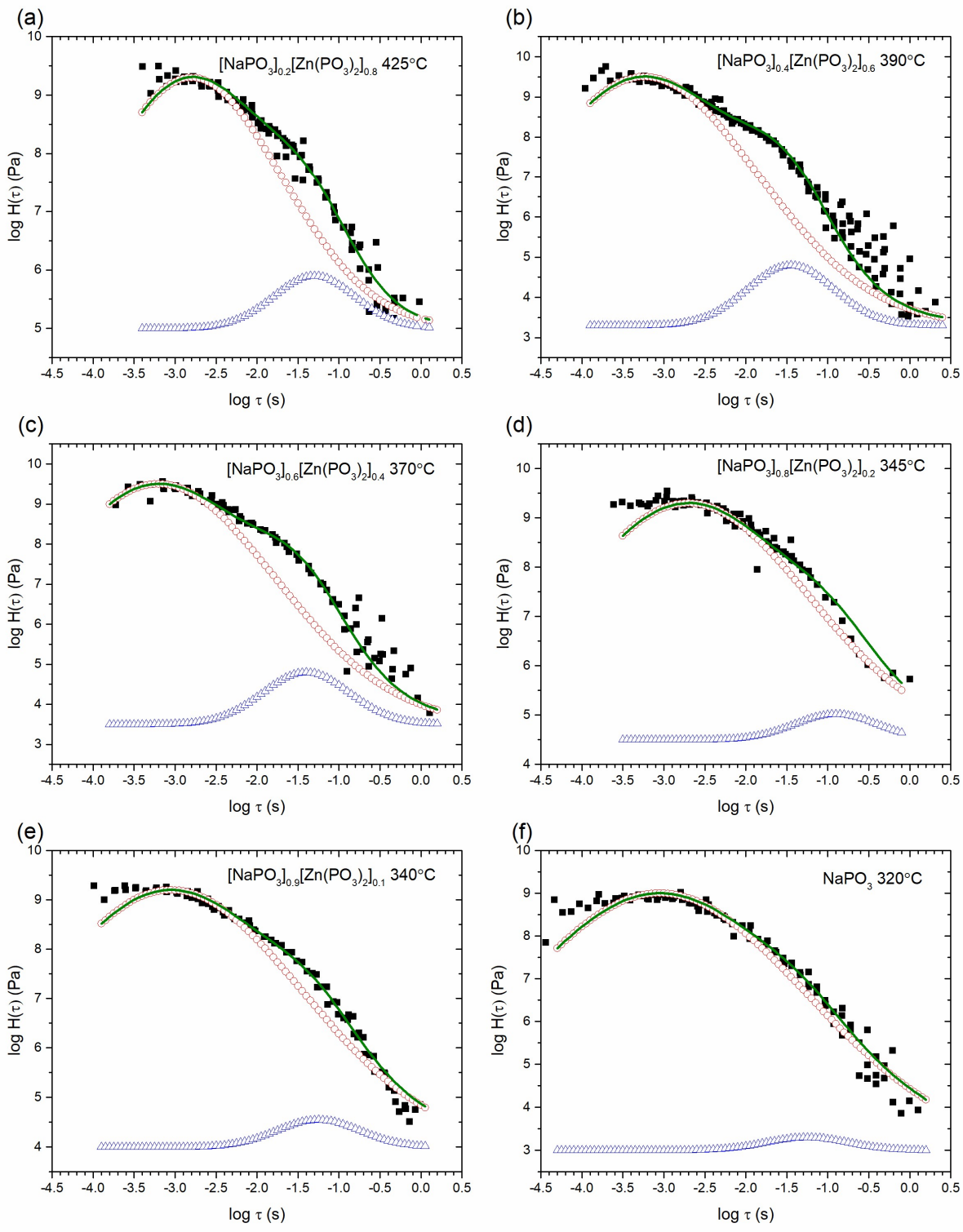

Figure 5-6 Relaxation spectra $H(\tau)$ of $[NaPO_3]_x[Zn(PO_3)_2]_{1-x}$ liquids. Filled squares are experimental data. Open circles and triangles represent the Gaussian components corresponding to the fast and slow processes, respectively. Solid green lines represent the total fit to the experimental data.

weak inter-chain cross-linking in Na-rich compositions gives rise to a lowering of dynamical constraints on chain reorientation.

It was shown in a previous rheological study of supercooled Se-rich P-Se liquids that the width of the timescale distribution for the segmental Se chain motion reflects the associated conformational entropy S_{conf} of the constituent chains and, thus, would be a sensitive function of the effective chain length [39]. Additionally, the fragility index m of a wide variety of inorganic glass-forming network liquids including phosphates has been related in the past to the average connectivity $<r>$ of the network through the relation: $m^* \propto \left(\frac{dS_{conf}}{d<r>}\right)^2$, where $m^* = \frac{m-m_0}{m_0}$ is the reduced fragility index normalized with respect to a minimum fragility index m_0 = 17 and the term $\frac{dS_{conf}}{d<r>}$ can be taken to represent the change in the conformational entropy of chains upon progressive cross-linking and increase in $<r>$ [18]. Therefore, the effective length of the metaphosphate chains or their effective degree of cross-linking, the fragility index m^* and the corresponding peak full-width-at-half-maximum (FWHM) of the fast relaxation process in $H(\tau)$ spectra of these Na-Zn metaphosphate liquids should be qualitatively correlated. The composition dependence of the FWHM of this peak (Fig. 5-7) in these liquids is observed to increase from ~ 2.7 log units to ~ 4.2 log units upon increasing the Na:Zn ratio. The average phosphate chain length is estimated to be ~100–200 PO_4 tetrahedra for metaphosphate liquids [22,40] and is likely somewhat shorter in Zn-metaphosphate in comparison with that in Na-metaphosphate due to the higher extent of Q-species disproportionation in the former [41,42]. Considering this similarity in the nominal chain length, the effective chain length in alkali-zinc metaphosphate glasses is likely to be controlled by the interaction between the phosphate chains and the modifier cations. The stronger cross-linking of the metaphosphate chains via Zn-O polyhedra in Zn-rich compositions

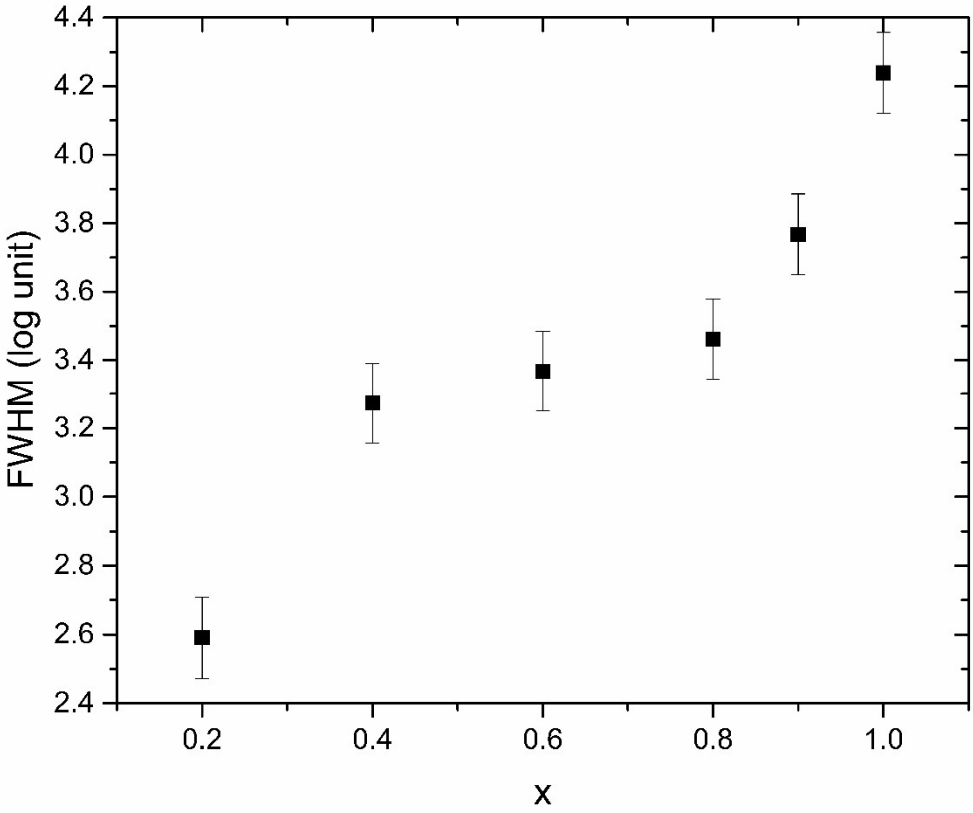

Figure 5-7 FWHM of the Gaussian component corresponding to segmental chain motion in relaxation spectra $H(\tau)$ of $[NaPO_3]_x[Zn(PO_3)_2]_{1-x}$ supercooled liquids.

would likely result in a pinning effect on the chain reorientation and an effective shortening of the chain length, consistent with the observed compositional evolution of the FWHM of the $H(\tau)$ peak for the segmental chain dynamics (Fig. 5-7). This hypothesis is also supported by the compositional variation of the fragility index m of these Na-Zn metaphosphate liquids. The m value, determined calorimetrically in the present study, increases monotonically with increasing Na:Zn ratio (Fig. 5-8). Indeed, as expected from the above discussion, the corresponding reduced fragility indices m^* display an intriguing correlation with the corresponding variation in the square of the FWHM of the fast relaxation process in the $H(\tau)$ spectra of these Na-Zn metaphosphate

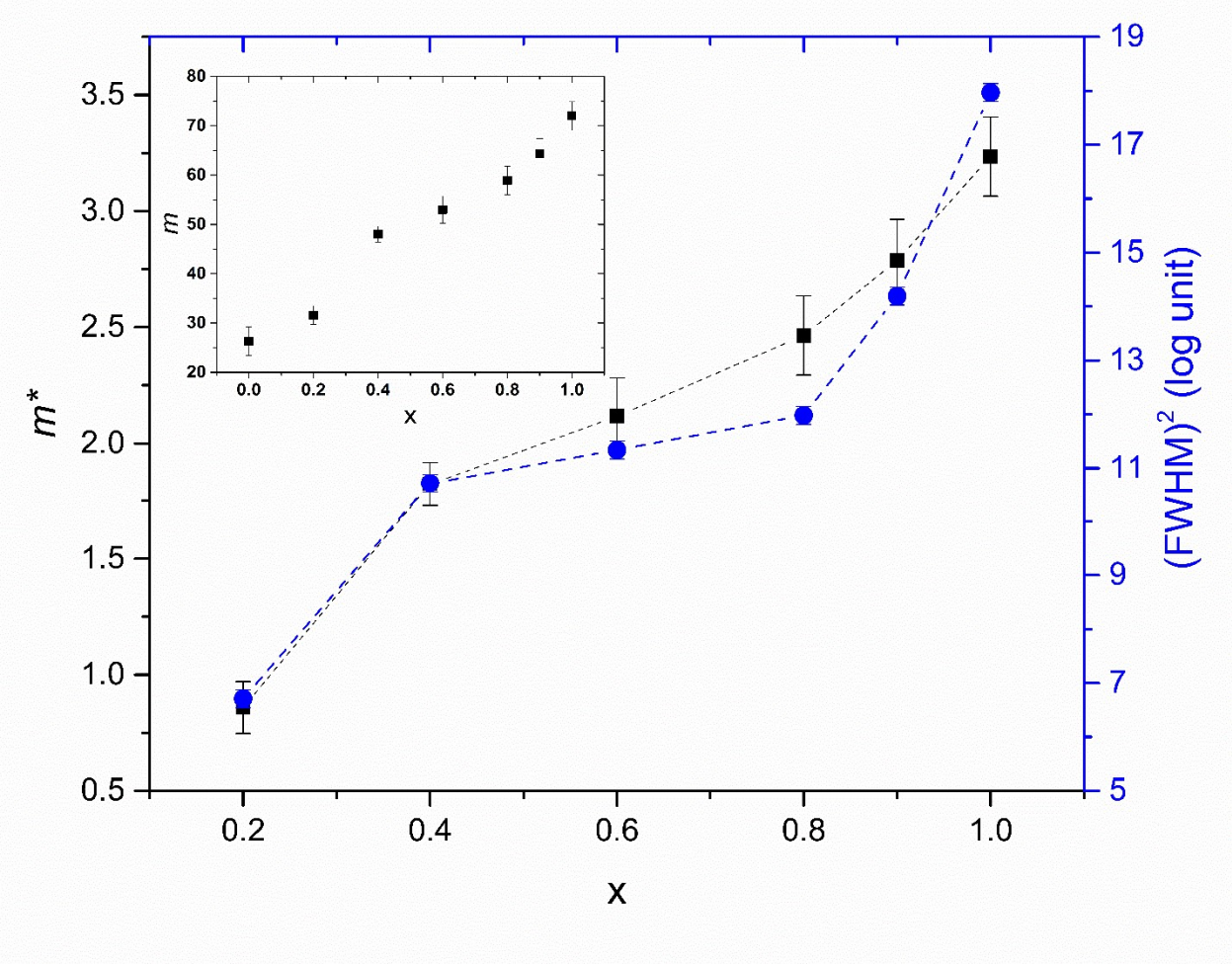

Figure 5-8 Composition dependence of reduced fragility indices of $[NaPO_3]_x[Zn(PO_3)_2]_{1-x}$ supercooled liquids obtained in the present study (black square) and of $(FWHM)^2$ of the Gaussian component corresponding to segmental chain motion in the relaxation spectra $H(\tau)$ (blue circle). Dashed lines are a guide to the eye. Inset shows corresponding compositional variation of the fragility indices of these liquids.

liquids (Fig. 5-8). In contrast, the FWHM of ~1.2 log units for the $H(\tau)$ peak attributed to bond scission/renewal dynamics is found to remain effectively constant for all $[NaPO_3]_x[Zn(PO_3)_2]_{1-x}$ liquids, indicating a nearly compositional independent P–O bond scission and renewal process.

The validity of the deconvolution of the $H(\tau)$ spectra into two relaxation processes can be corroborated by a comparison between the average timescales for these two processes measured in this dissertation with those reported by Sidebottom *et al.* for the $[NaPO_3]_{0.8}[Zn(PO_3)_2]_{0.2}$ liquid

using photon correlation spectroscopy (PCS) [21]. Such a comparison is shown in Fig. 5-9. Sidebottom *et al.* observed two dynamical processes in their study, the faster of which was characterized by a higher activation energy and was assigned to the shear relaxation while the slower process with a lower activation energy was found to be a diffusive mode that was tentatively assigned to the slow diffusion of Zn atoms. It is clear from Fig. 5-9 that the relaxation time of fast chain dynamics obtained by oscillator shear in the present study and that of fast dynamics

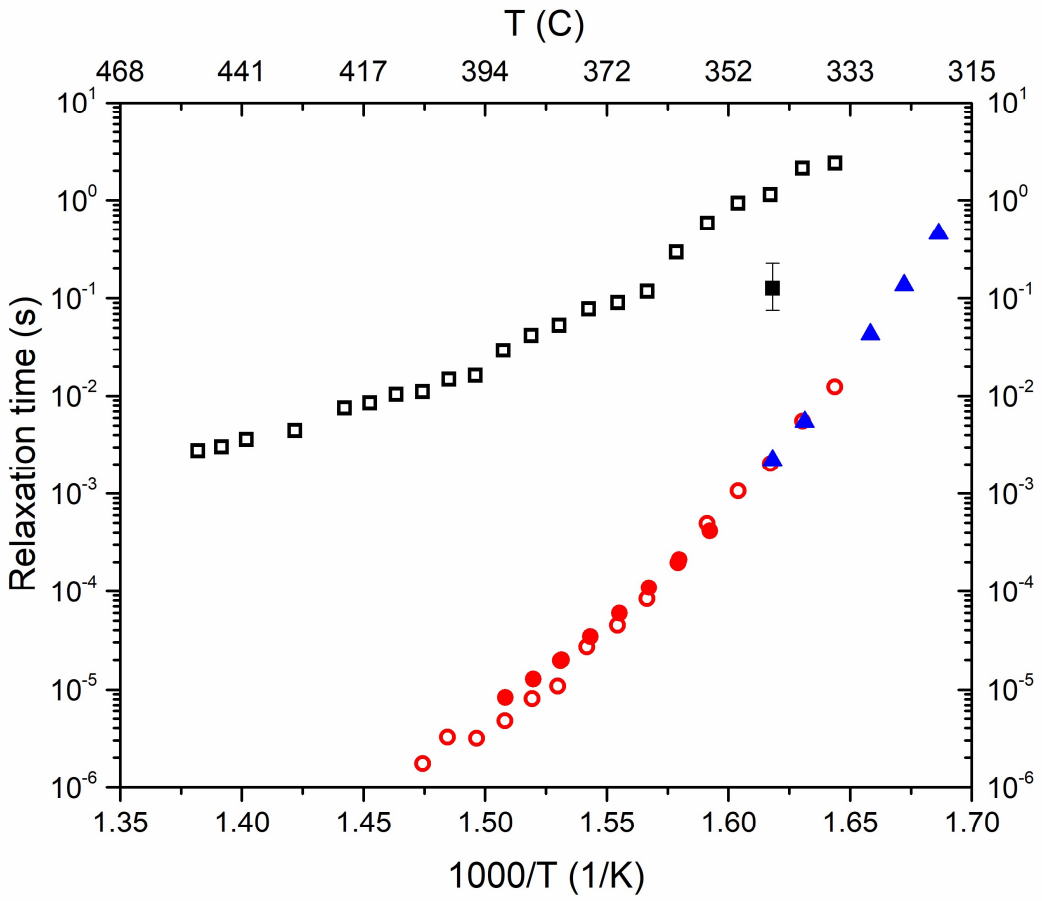

Figure 5-9 Temperature dependence of Maxwell relaxation timescale from viscosity data (filled red circles) and relaxation timescale of the fast (filled blue triangles) and slow (filled black square) dynamical processes obtained from oscillatory shear rheometry in the present study for the $[NaPO_3]_{0.8}[Zn(PO_3)_2]_{0.2}$ liquid. The relaxation time of slow process (open black square) and fast process (open red circle) for this liquid obtained using PCS in a previous study are shown for comparison [21].

reported by Sidebottom *et al.* are in good agreement. Furthermore, these timescales are also in good agreement with the shear relaxation time for this liquid obtained from the Maxwell relation $\tau = \eta/G_\infty$, where η and G_∞ were measured in the present study using steady shear rheometry and RUS, respectively. These results suggest that the shear relaxation of these metaphosphate liquids is controlled by segmental motion of the phosphate chains, the timescale distribution of which is represented by the broad peak at longer timescale in the $H(\tau)$ spectra in Fig. 5-6. On the other hand, the timescale corresponding to the slow bond scission/renewal dynamics in the $[NaPO_3]_{0.8}[Zn(PO_3)_2]_{0.2}$ liquid as observed in the $H(\tau)$ spectrum is consistent with, albeit somewhat faster than, the timescale of the slow process reported by Sidebottom *et al.* using PCS (Fig. 5-9). However, the observed discrepancy in the timescales measured by SAOS rheometry in this chapter and by PCS in [21] may well within be the experimental errors associated with the measurements and estimation processes. Unfortunately, the absence of error bars in the data reported in [21] precludes a definitive conclusion in this regard. It may, however, be noted that Sidebottom *et al.* were able to observe the slow relaxation process only in the Na-rich metaphosphate compositions, which can be explained by the fact that the timescale difference between the fast and slow processes $\Delta\tau$ in $H(\tau)$ spectra in Fig. 5-6 decreases significantly for Zn-rich compositions with x<0.4. This increased temporal coupling between the fast and the slow processes might have prohibited their separation by PCS in the Zn-rich compositions.

5.5 Conclusion

All $[NaPO_3]_x[Zn(PO_3)_2]_{1-x}$ supercooled liquids display thermorheological complexity and the coexistence of two dynamical processes with timescales differing by nearly two orders of magnitude. The fast process, attributed to the segmental motion of the constituent metaphosphate chains, is characterized by a broad timescale distribution and it predominantly controls the shear relaxation process in these liquids. On the other hand, the slow process can be ascribed to the diffusive P-O bond scission/renewal dynamics. The kinetic fragility index of these liquids monotonically increases with increasing Na:Zn ratio and is shown to be correlated with the conformational entropy of the metaphosphate chains. This conformational entropy is hypothesized to be a function of the degree of effective inter-chain cross-linking imparted by the modifier-oxygen coordination polyhedral, which increases with increasing Zn content.

References

[1] R.K. Brow, Review: the structure of simple phosphate glasses, J. Non. Cryst. Solids. 263&264 (2000) 1–28.

[2] E.H. Oelkers, J. Montel, Waste Storage, Elements. 4 (2008) 113–116.

[3] P.Y. Shih, Properties and FTIR spectra of lead phosphate glasses for nuclear waste immobilization, Mater. Chem. Phys. 80 (2003) 299–304.

[4] J.A. Wilder, Glasses and glass ceramics for sealing to aluminum alloys, J. Non. Cryst. Solids. 38–39 (1980) 879–884.

[5] L.L. Hench, R.J. Splinter, W.C. Allen, T.K. Greenlee, Bonding mechanisms at the interface of ceramic prosthetic materials, J. Biomed. Mater. Res. 5 (1971) 117–141.

[6] C. Bergmann, M. Lindner, W. Zhang, K. Koczur, A. Kirsten, R. Telle, H. Fischer, 3D printing of bone substitute implants using calcium phosphate and bioactive glasses, J. Eur. Ceram. Soc. 30 (2010) 2563–2567.

[7] C. Hönninger, F. Morier-Genoud, M. Moser, U. Keller, L.R. Brovelli, C. Harder, Efficient and tunable diode-pumped femtosecond Yb:glass lasers, Opt. Lett. 23 (1998) 126.

[8] N.G. Boetti, D. Pugliese, E. Ceci-Ginistrelli, J. Lousteau, D. Janner, D. Milanese, Highly doped phosphate glass fibers for compact lasers and amplifiers: A review, Appl. Sci. 7 (2017) 1295.

[9] D. Pugliese, N.G. Boetti, J. Lousteau, E. Ceci-Ginistrelli, E. Bertone, F. Geobaldo, D. Milanese, Concentration quenching in an Er-doped phosphate glass for compact optical lasers and amplifiers, J. Alloys Compd. 657 (2016) 678–683.

[10] F. Muñoz, J. Rocherullé, I. Ahmed, L. Hu, Phosphate glasses, in: Springer Handb. Glas., Springer, Cham, 2019: pp. 553–594.

[11] R.K. Brow, T.M. Alam, D.R. Tallant, R.J. Kirkpatrick, Spectroscopic studies on the structures of phosphate sealing glasses, MRS Bull. 23 (1998) 63–67.

[12] J.J. Liang, R.T. Cygan, T.M. Alam, Molecular dynamics simulation of the structure and properties of lithium phosphate glasses, J. Non. Cryst. Solids. 263 (2000) 167–179.

[13] Y. Onodera, S. Kohara, H. Masai, A. Koreeda, S. Okamura, T. Ohkubo, Formation of metallic cation-oxygen network for anomalous thermal expansion coefficients in binary phosphate glass, Nat. Commun. 8 (2017) 1–8.

[14] L.Y. Zhang, H. Li, L.L. Hu, Statistical approach to modeling relationships of composition – structure – property I: Alkaline earth phosphate glasses, J. Alloys Compd. 734 (2018) 163–171.

[15] S. Yan, Y. Yue, Y. Wang, Y. Diao, D. Chen, L. Zhang, Effect of GeO_2 on structure and properties of Yb: Phosphate glass, J. Non. Cryst. Solids. 520 (2019) 119445.

[16] B.G. Aitken, S.C. Currie, B.C. Monahan, L. Wu, E.W. Coonan, Chalcogenide glass for low viscosity extrusion and injection molding, U.S. Patent 7116888, 2006.

[17] D.L. Sidebottom, T.D. Tran, S.E. Schnell, Building up a weaker network: The effect of

intermediate range glass structure on liquid fragility, J. Non. Cryst. Solids. 402 (2014) 16–20.

[18] D.L. Sidebottom, Fragility of network-forming glasses: A universal dependence on the topological connectivity, Phys. Rev. E - Stat. Nonlinear, Soft Matter Phys. 92 (2015) 1–9.

[19] Y. Xia, W. Zhu, M. Lockhart, B. Aitken, S. Sen, Fragility and rheological behavior of metaphosphate liquids : Insights into their chain vs . network characters, J. Non. Cryst. Solids. 514 (2019) 77–82.

[20] L. Muñoz-Senovilla, F. Muñoz, Behaviour of viscosity in metaphosphate glasses, J. Non. Cryst. Solids. 385 (2014) 9–16.

[21] D.L. Sidebottom, D. Vu, Assessing the network connectivity of modifier ions in metaphosphate glass melts : A dynamic light scattering study of Na-Zn mixtures, J. Chem. Phys. 145 (2016) 164503.

[22] Y. Xia, W. Zhu, J. Sen, S. Sen, Observation of polymer-like flow mechanism in a short-chain phosphate glass-forming liquid, J. Chem. Phys. 152 (2020).

[23] S. Wegner, L. Van Wu, G. Tricot, Network dynamics and species exchange processes in aluminophosphate glasses : An in situ high temperature magic angle spinning NMR view, J. Phys. Chem. B. 113 (2009) 416–425.

[24] S. Sen, Dynamics in inorganic glass-forming liquids by NMR spectroscopy, Prog. Nucl. Magn. Reson. Spectrosc. 116 (2020) 155–176.

[25] W. Zhu, B. Aitken, S. Sen, Investigation of the shear relaxation behavior of As-Se liquids within the framework of entropic and elastic models of viscous flow, J. Non. Cryst. Solids. 534 (2020) 119959.

[26] W. Zhu, M. Lockhart, B. Aitken, S. Sen, Dynamical rigidity transition in the viscoelastic properties of chalcogenide glass-forming liquids, J. Non. Cryst. Solids. 502 (2018) 244–248.

[27] R.L. Sammler, J.U. Otaigbe, M.L. Lapham, N.L. Bradley, B.C. Monahan, C.J. Quinn, Melt rheology of zinc alkali phosphate glasses, J. Rheol. 40 (1996) 285.

[28] S. Wei, G.J. Coleman, P. Lucas, C.A. Angell, Glass Transitions, Semiconductor-Metal Transitions, and Fragilities in Ge-V-Te (V=As, Sb) Liquid Alloys: The Difference One Element Can Make, Phys. Rev. Appl. 7 (2017) 1–10.

[29] Y. Xia, B. Yuan, O. Gulbiten, B. Aitken, S. Sen, Kinetic and Calorimetric Fragility of Chalcogenide Glass-Forming Liquids: Role of Shear vs Enthalpy Relaxation, J. Phys. Chem. B. (2021).

[30] F.F. Balakirev, S.M. Ennaceur, R.J. Migliori, B. Maiorov, A. Migliori, Resonant ultrasound spectroscopy: The essential toolbox, Rev. Sci. Instrum. 90 (2019).

[31] A. Migliori, J.L. Sarrao, W.M. Visscher, T.M. Bell, M. Lei, Z. Fisk, R.G. Leisure, Resonant ultrasound spectroscopic techniques for measurement of the elastic moduli of solids, Physica B, Condens. Matter. 183 (1993) 1–24.

[32] O.V. Laukkanen, Small-diameter parallel plate rheometry: a simple technique for measuring rheological properties of glass-forming liquids in shear, Rheol. Acta. 56 (2017)

661–671.

[33] N. V. Pogodina, M. Nowak, J. Läuger, C.O. Klein, M. Wilhelm, C. Friedrich, Molecular dynamics of ionic liquids as probed by rheology, J. Rheol. 55 (2011) 241–256.

[34] C. Gainaru, R. Figuli, T. Hecksher, B. Jakobsen, J.C. Dyre, M. Wilhelm, R. Böhmer, Shear-Modulus investigations of monohydroxy alcohols: Evidence for a short-chain-polymer rheological response, Phys. Rev. Lett. 112 (2014) 1–4.

[35] N. Lou, Y. Wang, X. Li, H. Li, P. Wang, C. Wesdemiotis, A.P. Sokolov, H. Xiong, Dielectric relaxation and rheological behavior of supramolecular polymeric liquid, Macromolecules. 46 (2013) 3160–3166.

[36] S. Trinkle, C. Friedrich, Van Gurp-Palmen-plot : a way to characterize polydispersity of linear polymers, Rheol. Acta. 40 (2001) 322–328.

[37] J.D. Ferry, Viscoelastic Properties of Polymers, John Wiley & Sons, 1980.

[38] W. Zhu, B.G. Aitken, S. Sen, Observation of a dynamical crossover in the shear relaxation processes in supercooled selenium near the glass transition, J. Chem. Phys. 150 (2019).

[39] B. Yuan, B. Aitken, S. Sen, Structural control on the rheological behavior of binary P-Se supercooled liquids, J. Non. Cryst. Solids. 559 (2021) 120669.

[40] M. Crobu, A. Rossi, F. Mangolini, N.D. Spencer, Chain-length-identification strategy in zinc polyphosphate glasses by means of XPS and ToF-SIMS, Anal. Bioanal. Chem. 403 (2012) 1415–1432.

[41] J.W. Wiench, M. Pruski, B. Tischendorf, J.U. Otaigbe, B.C. Sales, Structural studies of zinc polyphosphate glasses by nuclear magnetic resonance, J. Non. Cryst. Solids. 263 (2000) 101–110.

[42] L. Muñoz-Senovilla, S. Venkatachalam, F. Muñoz, L. Van Wüllen, Relationships between fragility and structure through viscosity and high temperature NMR measurements in Li_2O-ZnO-P_2O_5 phosphate glasses, J. Non. Cryst. Solids. 428 (2015) 54–61.

[43] H.A.S. Al-Shamiri, A.S. Eid, Optical and Ultrasonic Properties of Chromium Oxide in Sodium Zinc Phosphate Glass, 1 (2012) 1–8.

[44] K.A. Matori, M. Hafiz, M. Zaid, H.J. Quah, S. Hj, A. Aziz, Z.A. Wahab, M. Sabri, M. Ghazali, Studying the effect of ZnO on physical and elastic properties of $(ZnO)_x(P_2O_5)_{1-x}$ glasses using nondestructive ultrasonic method, Adv. Mater. Sci. Eng. 2015, Arti (2015) 6 pages.

[45] P.K. Jha, O.P. Pandey, K. Singh, FTIR spectral analysis and mechanical properties of sodium phosphate glass-ceramics, J. Mol. Struct. 1083 (2015) 278–285.

[46] Z. Černošek, M. Chládková, J. Holubová, The influence of TiO2 on the structure and properties of sodium-zinc phosphate glasses, J. Non. Cryst. Solids. 531 (2020) 119866.

[47] B.C. Tischendorf, T.M. Alam, R.T. Cygan, J.U. Otaigbe, The structure and properties of binary zinc phosphate glasses studied by molecular dynamics simulations, J. Non. Cryst. Solids. 316 (2003) 261–272.

Chapter 6

Layer-by-Layer Freezing of Nanoconfined Water

6.1 Abstract

Nanoconfined water plays a pivotal role in a vast number of fields ranging from biological and materials sciences to catalysis, nanofluidics and geochemistry. Here, the freezing and melting behavior of water (D_2O) nanoconfined in architected silica-based matrices including Vycor glass and mesoporous silica SBA-15 and SBA-16 with pore diameters ranging between 4-15 nm is reported, which are investigated using differential scanning calorimetry and ^2H nuclear magnetic resonance spectroscopy. The results provide compelling evidence that the extreme dynamical heterogeneity of water molecules is preserved over distances as small as a few angstroms. Solidification progresses in a layer-by-layer fashion with a coexistence of liquid-like and solid-like dynamical fraction at all temperatures during the transition process. The previously reported fragile-to-strong dynamic transition in nanoconfined water is argued to be a direct consequence of the layer-by-layer solidification.

6.2 Introduction

Numerous research findings over the last three decades have shown that water confined in nanometer-sized pores, created in nanoarchitected solids, displays noticeably different behavior compared to bulk water [1–10]. Most interestingly, however, water unlike any other liquid, displays pronounced dynamical heterogeneity under nanoconfinement and freezes in a stepwise fashion. Furthermore, temperature-resolved measurements of the dynamics of nanoconfined water have suggested a fragile-to-strong liquid-liquid polyamorphic transition en route to freezing [11–13]. This nonconformist behavior of water has aroused intense scientific interest in probing the perplexing nature of the freezing dynamics of water in well-defined nanopores contained inside solid materials.

One of the most interesting and well-known effects of nanoconfinement is the depression of the freezing/melting point of water, which has been extensively studied by calorimetry [14–19]. The freezing point of nanoconfined water, for pore diameters larger than 2.5 nm, is found to decrease linearly with the increase in the inverse of an effective pore size following the Gibbs-Thomson (G-T) relation [20]. The G-T relation for the freezing point depression ΔT_m can be expressed as: $\Delta T_m = 2V_{mb}T_{mb}\gamma_{sl}/\Delta H_f(R-t)$, where V_{mb}, T_{mb} and γ_{sl} are the molar volume, melting point and enthalpy of fusion of the bulk crystal, respectively, γ_{sl} is the solid-liquid interfacial energy, *R* is the pore radius and *t* is the thickness of the interfacial water layer.

Although the effects of pore shape, pore filling and pore wall on the water freezing/melting behavior have been studied extensively in the past [14,21,22], the nature of the dynamics of nanoconfined water during the solidification process remains quite controversial [10–13,23–27]. Nevertheless, the majority of experimental and simulation studies indicate the presence of three

spatial regimes for water confined in the pores of silica with pore diameters ranging between 2-20 nm, characterized by quite different structural and dynamical behavior [10]. The first regime is a ~ 0.3 nm thick statistical monolayer of water molecules that are bound to the pore surface and perform restricted rotational motion. This layer is believed to remain unfrozen even down to ~ 190 K. Beyond this layer, water molecules still remain strongly structured by the pore walls of silica up to a distance of ~ 1 nm from the wall. The mobility of this "shell" of water is significantly lower, while its density is higher, compared to that of bulk water. Experimental and simulation studies indicate that this shell of water displays density layering. On the other hand, the density and mobility of the water molecules in the "core" region beyond ~1 nm from the pore wall is believed to be similar to that of bulk water. Therefore, it is likely that upon cooling, the core region will freeze first, followed by the shell region and thus, the latter will display a stronger effect of spatial confinement compared to the former. It is quite likely that instead of an abrupt change in the melting point across the core-shell boundary region, the effect of nanoconfinement will result in a gradual increase in melting point from near the pore wall towards the center. This hypothesis would be consistent with the observation of a long low-temperature tail in the melting endotherm in the differential scanning calorimetric (DSC) scans of water confined in porous silica [20].

On the other hand, ^{2}H nuclear magnetic resonance (NMR) spectroscopic studies of D_2O confined in 2.0 nm diameter pores in mesoporous silica MCM-41 have shown the presence of heterogeneous dynamics with a bimodal behavior characterized by the coexistence of a relatively immobile and a highly mobile fraction of molecules below the DSC freezing point [28]. The relative fraction of the mobile molecules decreases with lowering of temperature, until nearly all molecules become immobile at temperatures below ~ 190 K. This coexistence of mobile and immobile molecules and the progressive increase in the immobile fraction with temperature also

appear to be consistent with the abovementioned hypothesis of the gradual variation of the melting point across the core-shell boundary region. Here, I report the results of a systematic study of the freezing dynamics of water confined in the nanopores of mesoporous silica and Vycor™ with a wide range of pore diameter (~ 4 -15 nm) and geometry that is carried out using a combination of DSC and ^{2}H NMR to test this hypothesis. It is shown that the gradual "layer-by-layer" freezing model is consistent with the kinetics of the solidification process observed in experiments and can also explain the recently reported observation of an apparent fragile-to-strong dynamic crossover in nanoconfined water.

6.3 Experimental Methods

6.3.1 Sample preparation

Mesoporous SBA-15 and SBA-16 silica powders were synthesized according to acidic reaction methods as previously reported [29]. SBA-15 was synthesized by dissolving 4.0 g of triblock copolymer poly (ethylene oxide)20-poly(propylene oxide)70-poly(ethylene oxide)20 (Pluronic® P123, Aldrich), in 30 mL of water and 120 mL of 2 M HCl solution. Then, 9.1 mL of tetraethylorthosilicate (TEOS, Aldrich) was added to the solution, which was kept at 37 °C for 20 hours. Subsequently, the mixture was placed in an oven at 70 °C for hydrothermal treatment for 16 hours. This temperature was chosen to obtain SBA-15 samples with thick walls and to avoid formation of pores connecting the mesopore channels [30]. The resulting white precipitate was then washed with water and ethanol, dried in an oven at 70 °C and calcined at 500 °C for 3 hours. To synthesize SBA-16, 3.0 g of triblock copolymer poly (ethylene oxide)106-poly(propylene oxide)70-poly(ethylene oxide)106 (Pluronic® F127, Aldrich) were dissolved in 144 mL of water and 144 mL of 2 M HCl solution. Subsequently, 11 mL of butyl alcohol and 15 mL of TEOS were

added. The solution was then kept in an oven at 45 °C for 24 hours, followed by a hydrothermal treatment 100 °C for 24 hours. The resulting white precipitate was then washed, dried, and calcined as described above for SBA-15.

The mesopore structure was determined by transmission electron microscopy (TEM) characterization (see Chapter 7). For TEM imaging, SBA-15 and SBA-16 powders were dispersed in ethanol. A small amount of this dispersion was placed on a TEM grid by drop-casting and dried in air. TEM images of mesoporous materials were taken by an FEI Tecnai 12 transmission electron microscope. Nitrogen adsorption/desorption isotherms were obtained using a Sorptometer (Gemini 5, Micromeritics) at 77 K. The mesoporous materials were degassed at 523 K for 6 hours at a pressure of 3 mTorr prior to adsorption. The specific surface areas of the samples were calculated by the Brunauer-Emmett-Teller (BET) method, and pore size distribution were calculated by the Density Functional Theory (DFT) method using Micromeritics software kernels. The average pore size of two different SBA-15 samples with hexagonally arranged cylindrical pores was found to be 4.4 and 5.4 nm, whereas in cage-structured SBA-16, large spherical pores (5.5 nm) are body-centered-cubic arranged and connected by narrow openings (3.2 nm). D_2O was added to excess amount of as-prepared mesoporous silica powder and the mixture was stirred to obtain partially hydrated samples for DSC and NMR experiments.

The Vycor-109 and Vycor-145 porous glasses with average pore size of 10.9 nm and 14.5 nm, respectively, were obtained from Corning Inc. in the form of buttons of dimensions 6.9 mm diameter and 2.5 mm height by Corning Glass Works. These glasses were prepared from commercial Vycor (Corning code 7930) parent glass using extended heat treatments to coarsen the microstructure of the leachable phase followed by sequential etch treatments. Vycor-109 (145) was prepared by a heat treatment of the 7930 parent glass for 10 (80) h at 580 °C followed by

cooling at 25(10) °C /h. These heat-treated samples were then immersed in 30 wt% NH_4F solution for 5 minutes and subsequently directly transferred to 0.25N HNO_3 kept at 95 °C, and were etched for 2 h. Etched samples were rinsed at 95 °C in deionized water for 1h and dried at 100 °C in an oven. The average pore size of these samples were determined using mercury porosimetry at 50% intrusion level. 'Thirsty' Vycor glass was obtained by baking all samples at 200 °C overnight to remove any absorbed organic impurities.

The thirsty Vycor glass buttons were immersed in pure D_2O (Aldrich) for 10 minutes to obtain fully hydrated samples. These samples were subsequently dried at ambient condition for 1h to remove any freezable bulk water on the sample surface through water evaporation, crushed into powder and used in DSC and NMR experiments.

6.3.2 Differential scanning calorimetry

The DSC measurements were carried out using a Mettler Toledo DSC1 differential scanning calorimeter. About 10-25 mg partially hydrated samples were hermetically sealed in 40 μL aluminum pans. Scans were taken in a flowing nitrogen environment with a heating rate of 5 K/min from –100 °C to 25 °C. Melting point was determined to within ± 2 °C as the onset of the melting endotherm. The degree of water loading was found to have negligible effect on melting temperature determination [14]. The temperature scale was calibrated to the onset of the melting endotherm of pure bulk D_2O at 277.0 K.

6.3.3 ^2H Nuclear Magnetic Resonance spectroscopy

All ^2H wideline NMR spectra of the hydrated samples were acquired using a Bruker Avance500 spectrometer equipped with a Bruker magnet operating at 11.7 T (^2H Larmor

frequency of 76.7 MHz). The powder samples were taken in 4 mm and 7 mm ZrO_2 rotors and NMR spectra were collected using either a Bruker 4mm triple-resonance probe or a Bruker 7mm double-resonance probe. The temperature was controlled to within ± 2 K using nitrogen gas boil-off from liquid nitrogen. A solid-echo pulse sequence ($\pi/2-\tau-\pi/2-$acquisition) was employed for spectral acquisition with $\pi/2$ pulse length of 3.2 μs, τ = 10 μs and a recycle delay of 1 s. Each spectrum was obtained by Fourier transforming the average of 512 free induction decays. Multiple spectra, acquired with stepped offset in carrier frequency covering overlapping frequency ranges with uniform excitation, were stitched together to obtain the full spectral line shape at each temperature. All ^2H NMR line shapes were simulated using the software DMFit [31].

6.4 Results and Discussion

6.4.1 Melting point depression of nanoconfined D_2O

DSC heating curves for D_2O in two mesoporous silica SBA-15 with regular cylindrical 4.4 and 5.4 nm diameter pores, in mesoporous silica SBA-16 with large spherical pores (5.5 nm diameter) connected by narrow cylindrical channels (3.2 nm diameter) and in two Vycor glass samples with tortuous channels with average diameters of 10.9 nm and 14.5 nm (denoted, respectively, as Vycor-109 and Vycor-145) are shown in Fig. 6-1a. While only one melting peak exists in the DSC scans of all samples with a single nanopore/channel size, two endothermic peaks are observed for the partially hydrated SBA-16 sample, corresponding to water confined in this bimodal pore structure. This is the first report, to the best of our knowledge, of observation of two distinct freezing points for water nanoconfined in interconnected pores of different size. Considering the connectivity between the spherical and cylindrical pores in SBA-16, the observation of dual melting points in this system implies that under nanoconfinement strong

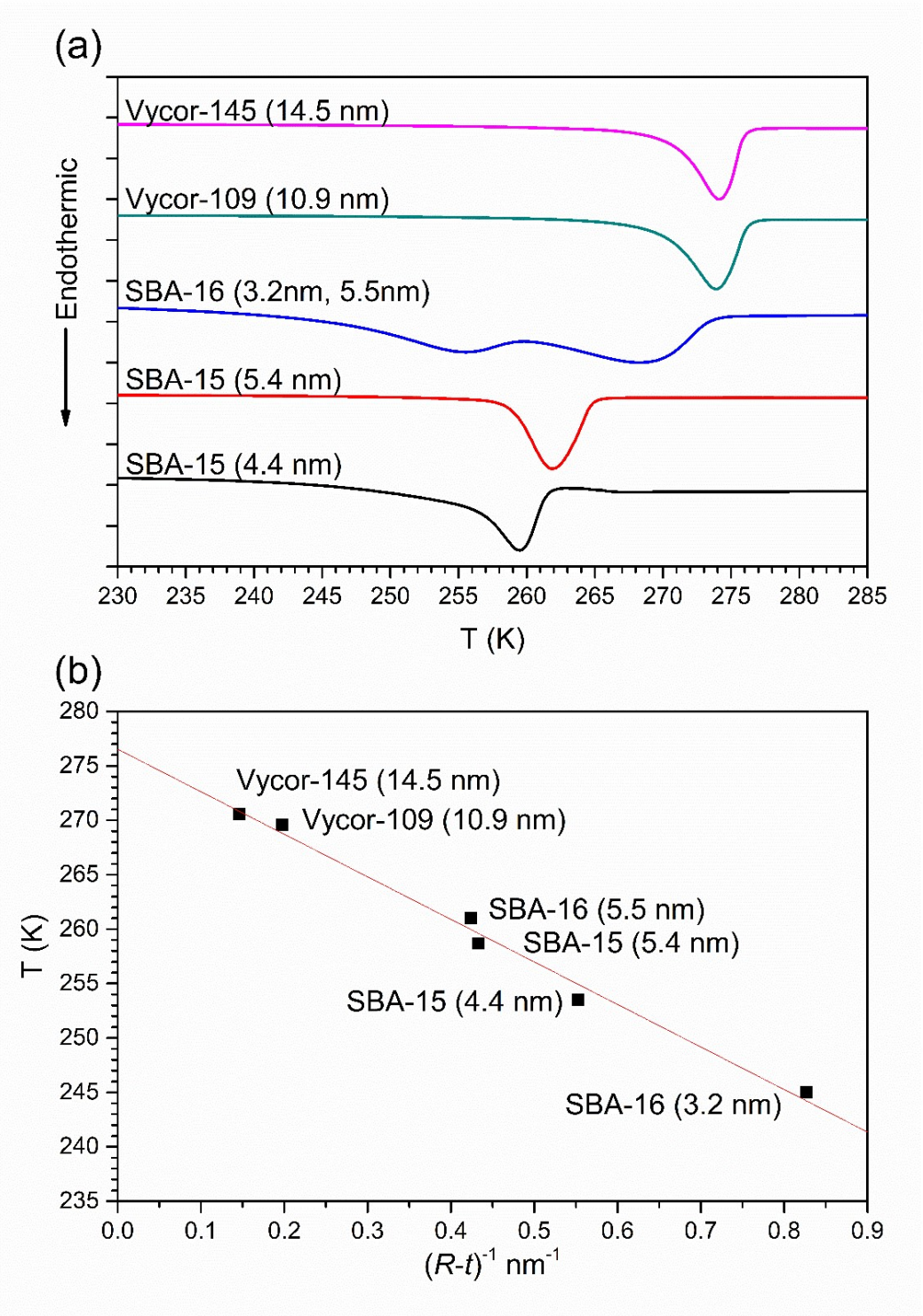

Figure 6-1 (a) DSC melting scans at 5 K/minute for D_2O confined in Vycor-145, Vycor-109, SBA-15 and SBA-16. Corresponding pore diameters are given in the legend. (b) Melting point onsets determined from the DSC scans in (a) as a function of the inverse of the effective pore radius. Red straight line through the data points is a linear least-squares fit of the simplified Gibbs-Thomson equation (see text for details).

dynamical heterogeneity of water molecules can be preserved even over such short distances of a few Å. The melting temperature T_m of confined D_2O in these systems, corresponding to the onset of the DSC endothermic peak, strictly obeys the G-T relation and varies linearly with the inverse of the effective pore size ($R - t$) as shown in Fig. 6-1b. The least-squares fitting of melting points according to the simplified form of the G-T relation: $\Delta T_m = K/(R - t)$ yields fitting parameters $K = 39.1 \pm 2.1$ K·nm and $t = 0.39 \pm 0.06$ nm, the latter being consistent with the thickness of the statistical monolayer of water molecules attached to the pore wall. Furthermore, this value of t for confined D_2O is similar to that obtained for confined H_2O,[14] where $t = 0.38 \pm 0.06$ nm, suggesting a similar interfacial bonding scenario for H_2O and D_2O. The experimental value of K is somewhat smaller than the theoretical constant $K_{th} = \frac{2V_{mb}T_{mb}\gamma_{sl}}{\Delta H_f} = 50.4$ K·nm, as obtained from using the values for bulk D_2O, i.e. the melting temperature $T_{mb} = 277.0$ K, specific volume $V_{mb} = 0.9009 \times 10^{-6}$ m^3/g, solid-liquid interfacial energy $\gamma_{sl} = 31.7 \times 10^{-3}$ J/ m^2 and enthalpy of fusion $\Delta H_f = 313.6$ J/g [32]. The deviation between the experimental and theoretical values of K is probably due to the sharp-interface approximation that is implicit in the G-T model. Finally, it is important to note that in all cases, the DSC heating curve endotherms display a long low-temperature tail associated with the main peak, which is consistent with the scenario of gradual melting and progression of the solid-liquid interface from the pore wall towards the center, across the core-shell boundary.

6.4.2 Freezing kinetics of nanoconfined D_2O from ^2H wideline NMR spectroscopy

^2H wideline NMR spectra are acquired for all samples of nanoconfined D_2O over a temperature range of 193-283 K and representative spectra are shown in Fig. 6-2a for the Vycor-109 sample. Spectra collected during cooling and heating were found to be identical, indicating

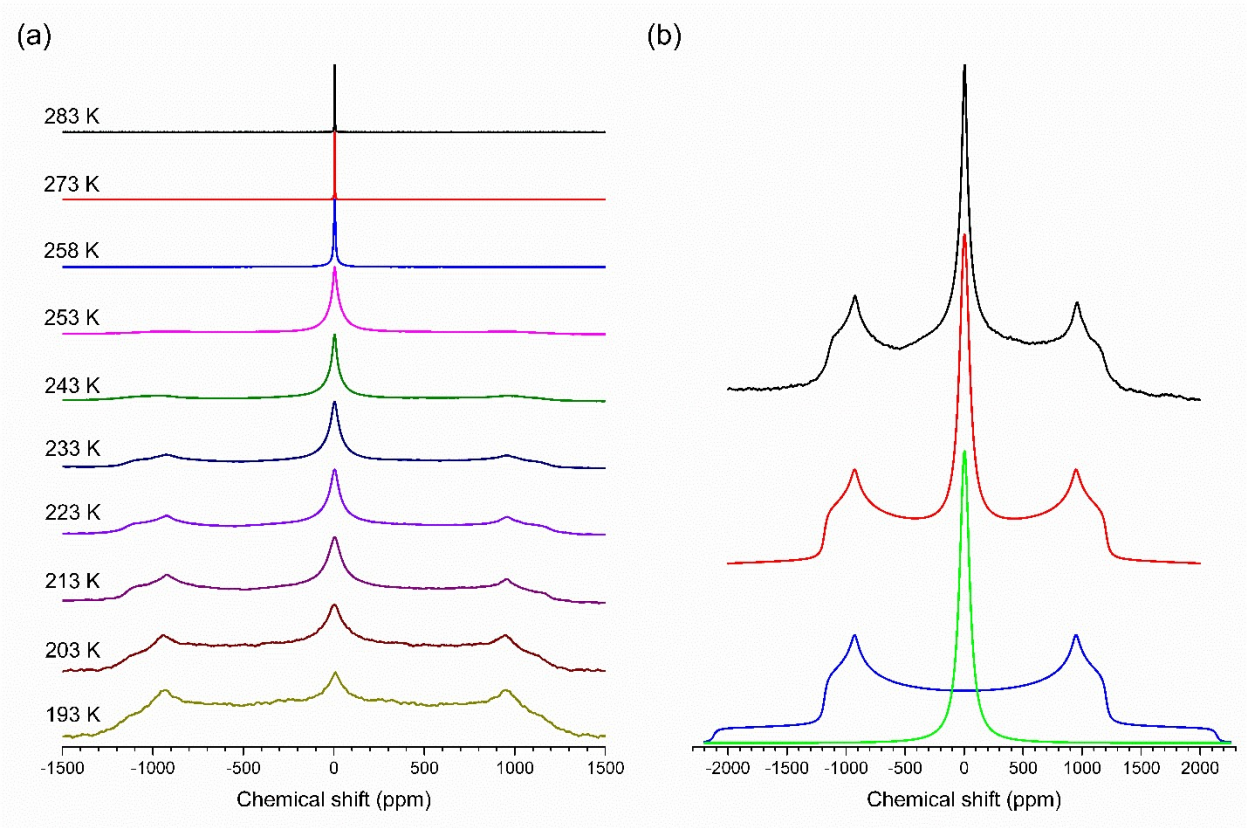

Figure 6-2 (a) Representative variable-temperature ^{2}H NMR wideline spectra of D_2O confined in Vycor-109. (b) Comparison between experimental (black line, top) and simulated (red line, middle) line shapes for the ^{2}H NMR spectrum collected at 223 K from (a). Individual simulation components are shown in green and blue (bottom). The Lorentzian line (green) and the Pake pattern (blue) correspond to the liquid-like and solid-like fraction, respectively.

the absence of any hysteresis. At the highest temperatures the ^{2}H NMR spectra are characterized by a narrow Lorentzian line indicative of rapid isotropic reorientation of D_2O molecules, characteristic of liquid water. An additional broad powder-like pattern (Pake pattern) appears at temperatures below 263 K, which corresponds to a sub-population of molecules that are either completely rigid or performing rotational motion at a frequency on the order of a few kHz or less. Simulation of this Pake pattern yields a quadrupolar coupling constant C_Q of 215 ± 10 kHz and an asymmetry parameter $\eta = 0.1 \pm 0.02$ at all temperatures for all samples (Fig. 6-2a). These values are in good agreement with the literature values for polycrystalline and single crystal ice [33,34].

These two spectral components corresponding to a fast liquid-like and a slow ice-like dynamic sub-population of water molecules coexist down to the lowest temperature (193 K) explored in the present study, although the relative fraction of the Lorentzian component decreases rapidly with cooling. Similar observations were also made in previous studies of water under nanoconfinement in other porous materials such as in mesoporous silica MCM-41 and in proteins such as collagen, elastin and myoglobin [25,28]. Such 'quasi' two-phase spectra imply the presence of a rather broad distribution of rotational correlation times or activation barriers, where the spectral line shape is dominated by the slow and fast populations [35]. This type of dynamical behavior is unprecedented in bulk liquids, but it is the hallmark of glassy dynamics with strong static heterogeneity and a lack of significant diffusive exchange between the slow and fast sub-populations. As such, this static heterogeneity is consistent with a layered core-shell structure of water in nanopores.

The relative fraction of the liquid-like dynamical population W can be obtained from the simulation of these ^{2}H NMR spectra with a Lorentzian line and a Pake pattern (Fig. 6-2b). The temperature dependence of this fraction $W(T)$ for all samples is shown in Fig. 6-3a and is compared with that reported in a previous study for D_2O confined in 2.0 nm diameter pores in MCM-41[28]. The onset temperature where $W(T)$ starts to decrease below 1, i.e. the solid-like sub-population starts to appear in the ^{2}H NMR spectra, is consistent with the melting temperature from the DSC measurement. With further reduction in temperature, $W(T)$ monotonically decreases following a sigmoidal kinetics until it reaches to ~ 0.1 near 193 K for all samples. This limiting value of $W(T)$ likely corresponds to the water molecules in the immediate vicinity of the pore wall that remain mobile down to 193 K. The most interesting result however, is the fact that the fast-to-slow sub-population conversion rate upon cooling is the highest for water confined in either the smallest

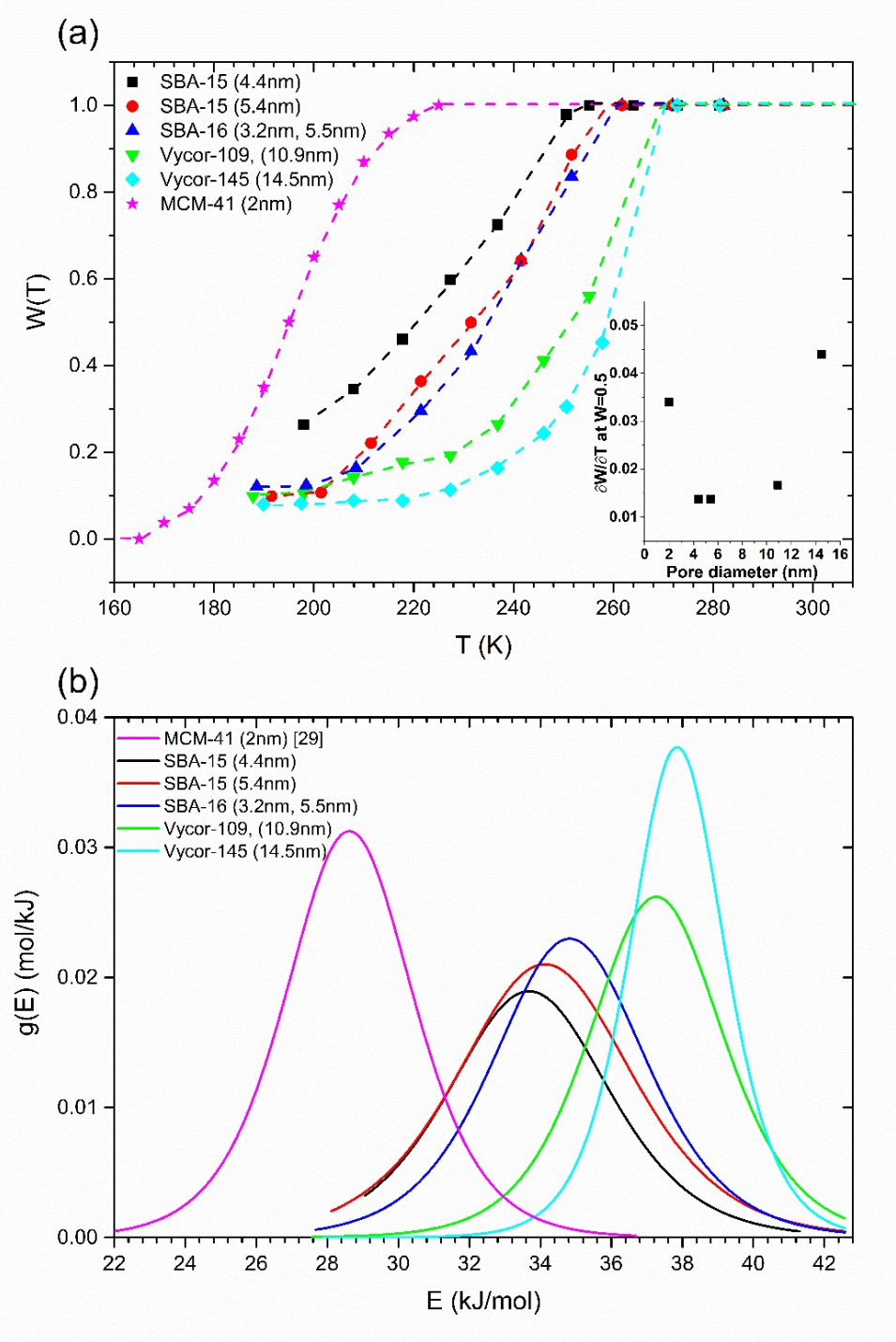

Figure 6-3 (a) Temperature dependence of the relative fraction of liquid-like dynamical population W(T) of D_2O confined in different silica matrices. Inset shows variation of the slope $\partial W(T)/\partial T$ at $W = 0.5$, as a function of pore diameter. (b) Activation energy distribution *g(E)* for molecular dynamics of D_2O confined in different silica matrices, obtained from the temperature derivative of W(T) curves in (a). For details of the calculation see text. W(T) data for MCM-41 is from [28].

(~2.0 nm) or the largest (≥10 nm) pores, while the rates are lower for confinement in intermediate-sized (4-6 nm) pores. This result is completely consistent with the core-shell model. Considering the pore diameters and the aforementioned thickness of the shell (~ 1nm), one would expect that the vast majority of the water molecules reside in the shell for pores with diameter ≤3 nm, while they reside in the core for pores with diameter ≥10 nm. Therefore, these regions being characterized by a relatively narrow temperature range of melting/freezing, *W(T)* is expected to show a rapid drop with temperature on cooling. On the other hand, for intermediate pore diameters between 3 and 10 nm, the relative fractions of core and shell regions become comparable and the hypothesized gradual variation in the melting/freezing point across the core-shell boundary would lead to a gentle drop in *W(T)* on cooling. These expected variations in *W(T)* are indeed borne out in the experimental results as shown in Fig. 6-3a, thereby lending support to the "layer-by-layer" freezing model mentioned above.

Additionally, for weakly temperature-dependent distribution of energy barriers, following the Arrhenius law, it can be shown that the activation energy distribution *g(E)* is related to the derivative of *W(T)* with respect to temperature as [35]: $g(E) = \frac{\partial W(T)/\partial T}{\ln\left(\frac{\tau^*}{\tau_0}\right)}$. In this expression τ^* is ~ $1/C_Q$, which is ~10^{-6}s for ^{2}H and τ_0 is a phonon timescale (10^{-13} to 10^{-14} s), corresponding to an attempt rate. The temperature scale is converted to an energy scale using the Arrhenius relation $E = RT \ln\left(\frac{\tau^*}{\tau_0}\right)$ where R is the gas constant, τ^*= 4.5*10^{-6}s and τ_0 = 10^{-13} s. As expected, the activation energy distribution becomes narrower for smaller and larger pores, compared to that for the intermediate pore sizes (Fig. 6-3b). However, the average activation energy ranges between ~ 28 and 38 kJ.mol^{-1}, consistent with previous reports of activation energy measurements using

NMR spin-lattice relaxation, dielectric relaxation and quasi-elastic neutron scattering techniques [13,27,36].

6.4.3 Core vs. shell dynamics and fragile-to-strong transition in confined water

The layer-by-layer freezing model also offers an explanation for the observation of an apparent transition in the temperature dependence of the relaxation time of water from a non-Arrhenius (i.e. fragile) to an Arrhenius (i.e. strong) behavior upon cooling [11,12]. As recently noted by Lederle *et al.* [37], with progressive freezing of nanoconfined water from the center towards the pore wall, the remaining liquid fraction becomes increasingly confined by the

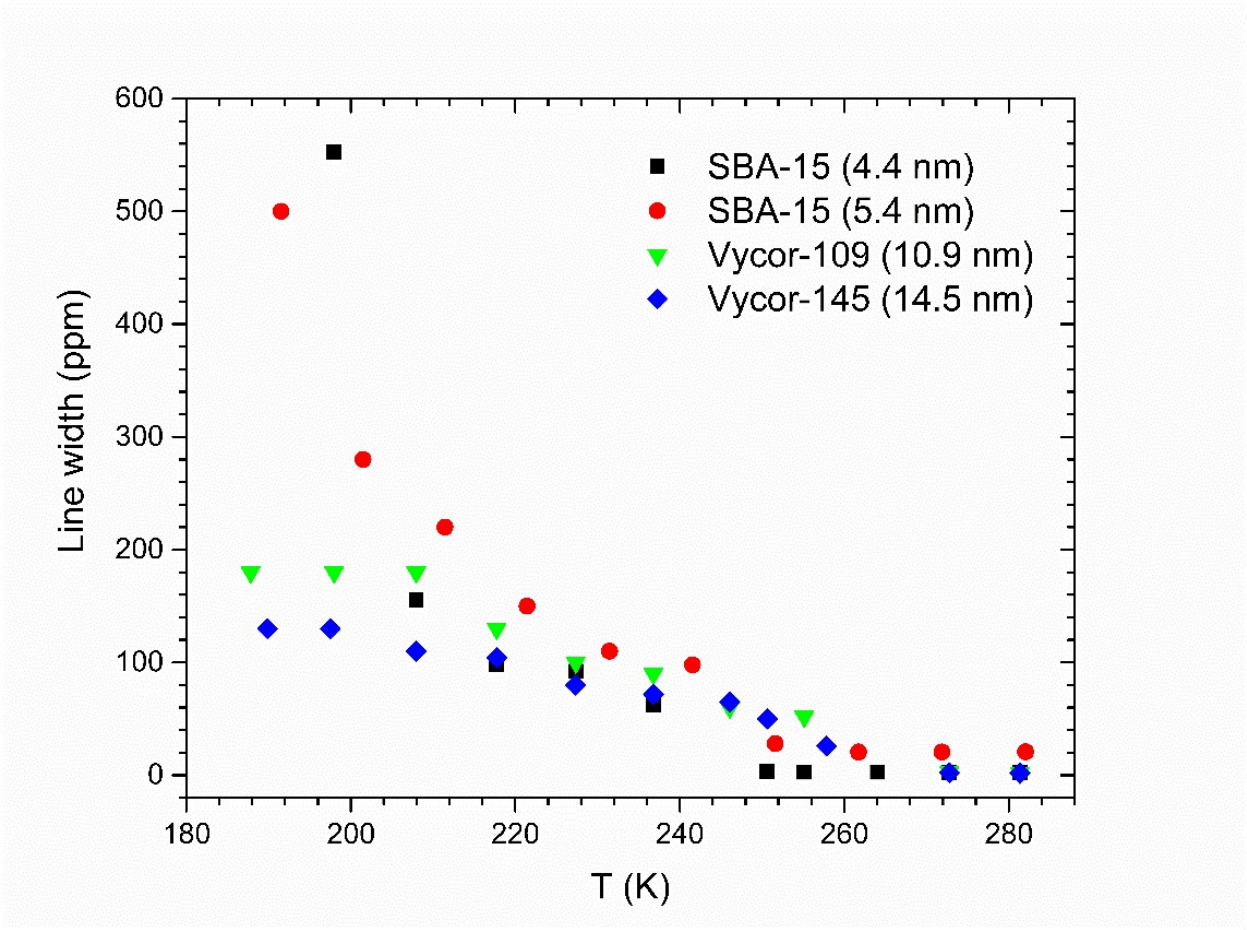

Figure 6-4 Full-width-at-half-maximum of the Lorentzian component in ^{2}H NMR spectra of D_2O confined in different silica matrices as a function of temperature.

surrounding. This confinement is expected to be particularly severe in smaller pores. The width Δ of the Lorentzian ^{2}H NMR line corresponding to the liquid-like dynamical population is a direct measure of the mobility of the water molecules in the liquid fraction. The temperature dependence of Δ for all samples is shown in Fig. 6-4, which increases with the lowering of temperature indicating that the mobility of the liquid fraction slows down with increasing solid-like fraction. This lowering in the mobility becomes rapid and strong as the pore size decreases (Fig. 6-4), implying increased effect of confinement on the remainder of the liquid fraction. As the length scale of this confinement becomes comparable to or smaller than that of the cooperatively rearranging regions responsible for structural or α-relaxation of the liquid, the effect of cooperative molecular motion would greatly diminish, and the dynamics would become Arrhenius [38]. Such a transition in the dynamical behavior upon strong nanoconfinement has been reported in the past for glass-forming liquids such as glycerol [39]. Therefore, we argue that the fragile-to-strong transition is a direct consequence of the layer-by-layer solidification behavior of water under strong nanoconfinement.

6.5 Conclusion

In summary we report a systematic study of the melting and freezing dynamics of D_2O confined in the nanopores of glassy and crystalline solid silica matrices with pore sizes ranging between ~ 4-15 nm, using a combination of DSC and ^{2}H NMR. In spite of the differences between the mesoporous silica and amorphous Vycor in the nature of their internal pore surfaces and possibly in their interactions with water, the melting point depression in all materials obey a single Gibbs-Thomson relation. Moreover, for all confining media the results are generally consistent with a model of freezing characterized by strong spatially heterogeneous glassy dynamics. The

extreme spatial heterogeneity in the dynamics is manifested in the very first observation of two distinct freezing points for water nanoconfined in interconnected pores of two different diameters in mesoporous silica SBA-16. The freezing likely starts at the center of the nanopores and proceeds gradually layer-by-layer, towards the periphery of the pore. This layer-by-layer freezing model that we propose also provides a credible explanation for an apparent fragile-to-strong transition in the temperature dependence of the relaxation time of nanoconfined water as reported in previous studies.

References

[1] R. Guégan, Confinement effects on water structure in membrane lyotropic phases, J. Colloid Interface Sci. 358 (2011) 485–490.

[2] J.L. Skinner, P.A. Pieniazek, S.M. Gruenbaum, Vibrational spectroscopy of water at interfaces, Acc. Chem. Res. 45 (2012) 93–100.

[3] F. Goettmann, C. Sanchez, How does confinement affect the catalytic activity of mesoporous materials?, J. Mater. Chem. 17 (2007) 24–30.

[4] R.B. Schoch, J. Han, P. Renaud, Transport phenomena in nanofluidics, Rev. Mod. Phys. 80 (2008) 839–883.

[5] A. Navarre-Sitchler, C.I. Steefel, P.B. Sak, S.L. Brantley, A reactive-transport model for weathering rind formation on basalt, Geochim. Cosmochim. Acta. 75 (2011) 7644–7667.

[6] A.A. Darhuber, S.M. Troian, Principles of microfluidic actuation by modulation of surface stresses, Annu. Rev. Fluid Mech. 37 (2005) 425–55.

[7] D.W.M. Hofmann, L. Kuleshova, B. D'Aguanno, V. Di Noto, E. Negro, F. Conti, M. Vittadello, Investigation of water structure in nafion membranes by infrared spectroscopy and molecular dynamics simulation, J. Phys. Chem. B. 113 (2009) 632–639.

[8] N. Alcantar, J. Israelachvili, J. Boles, Forces and ionic transport between mica surfaces: Implications for pressure solution, Geochim. Cosmochim. Acta. 67 (2003) 1289–1304.

[9] I.C. Bourg, G. Sposito, Connecting the molecular scale to the continuum scale for diffusion processes in smectite-rich porous media, Environ. Sci. Technol. 44 (2010) 2085–2091.

[10] I.C. Bourg, C.I. Steefel, Molecular dynamics simulations of water structure and diffusion in silica nanopores, J. Phys. Chem. C. 116 (2012) 11556–11564.

[11] F. Mallamace, M. Broccio, C. Corsaro, A. Faraone, D. Majolino, V. Venuti, L. Liu, C.-Y. Mou, S.-H. Chen, Evidence of the existence of the low-density liquid phase in supercooled, confined water, Proc. Natl. Acad. Sci. 104 (2007) 424–428.

[12] F. Mallamace, M. Broccio, C. Corsaro, A. Faraone, U. Wanderlingh, L. Liu, C.Y. Mou, S.H. Chen, The fragile-to-strong dynamic crossover transition in confined water: Nuclear magnetic resonance results, J. Chem. Phys. 124 (2006) 161102.

[13] A. Faraone, L. Liu, C.-Y. Mou, C.-W. Yen, S.-H. Chen, Fragile-to-strong liquid transition in deeply supercooled confined water, J. Chem. Phys. 121 (2004) 10843.

[14] A. Schreiber, I. Ketelsen, G.H. Findenegg, Melting and freezing of water in ordered mesoporous silica materials, Phys. Chem. Chem. Phys. 3 (2001) 1185–1195.

[15] M. Brun, A. Lallemand, J.-F. Quinson, C. Eyraud, A new method for the simultaneous determination of the size and shape of pores: the thermoporometry, Thermochim. Acta. 21 (1977) 59–88.

[16] J.C. van Miltenburg, J.P. van der Eerden, Very large melting point depression of water in silica, J. Cryst. Growth. 128 (1993) 1143–1149.

[17] T. Takamuku, M. Yamagami, H. Wakita, Y. Masuda, T. Yamaguchi, Thermal Property,

Structure, and Dynamics of Supercooled Water in Porous Silica by Calorimetry, Neutron Scattering, and NMR Relaxation, J. Phys. Chem. B. 101 (1997) 5370–5376.

[18] E.W. Hansen, H.C. Gran, E.J. Sellevold, Heat of fusion and surface tension of solids confined in porous materials derived from a combined use of NMR and calorimetry, J. Phys. Chem. B. 101 (1997) 7027–7032.

[19] R. Schmidt, E.W. Hansen, M. Stacker, D. Akporiaye, O.H. Ellestad, Pore size determination of MCM-41 mesoporous materials by means of NMR spectroscopy, N2 adsorption, and HREM. a preliminary study, J. Am. Chem. Soc. 117 (1995) 4049–4056.

[20] S. Kittaka, S. Takahara, H. Matsumoto, Y. Wada, T.J. Satoh, T. Yamaguchi, Low temperature phase properties of water confined in mesoporous silica MCM-41: thermodynamic and neutron scattering study, J. Chem. Phys. 138 (2013) 204714.

[21] K. Morishige, Influence of pore wall hydrophobicity on freezing and melting of confined water, J. Phys. Chem. C. 122 (2018) 5013–5019.

[22] K. Morishige, H. Yasunaga, Y. Matsutani, Effect of pore shape on freezing and melting temperatures of water, J. Phys. Chem. C. 114 (2010) 4028–4035.

[23] M. Vogel, NMR studies on simple liquids in confinement, Eur. Phys. J. Spec. Top. 189 (2010) 47–64.

[24] L. Liu, S.-H. Chen, A. Faraone, C.-W. Yen, C.-Y. Mou, Pressure dependence of fragile-to-strong transition and a possible second critical point in supercooled confined water, Phys. Rev. Lett. 95 (2005) 117802.

[25] S.A. Lusceac, M.R. Vogel, C.R. Herbers, 2H and 13C NMR studies on the temperature-dependent water and protein dynamics in hydrated elastin, myoglobin and collagen, Biochim. Biophys. Acta. 1804 (2010) 41–48.

[26] S.A. Lusceac, M. Vogel, 2H NMR Study of the Water Dynamics in Hydrated Myoglobin, J. Phys. Chem. B. 114 (2010) 10209–10216.

[27] M. Vogel, Origins of apparent fragile-to-strong transitions of protein hydration waters, Phys. Rev. Lett. 101 (2008) 225701.

[28] M. Sattig, M. Vogel, Dynamic crossovers and stepwise solidification of confined water: A 2H NMR study, J. Phys. Chem. Lett. 5 (2014) 174–178.

[29] D. Zhao, Q. Huo, J. Feng, B.F. Chmelka, G.D. Stucky, Nonionic triblock and star diblock copolymer and oligomeric surfactant syntheses of highly ordered, hydrothermally s, mesoporous silica structures, J. Am. Chem. Soc. 120 (1998) 6024–6036.

[30] A. Galarneau, H. Cambon, F. Di Renzo, R. Ryoo, M. Choi, F. Fajula, Microporosity and connections between pores in SBA-15 mesostructured silicas as a function of the temperature of synthesis, New J. Chem. 27 (2003) 73–79.

[31] D. Massiot, F. Fayon, M. Capron, I. King, S. Le Calvé, B. Alonso, J.O. Durand, B. Bujoli, Z. Gan, G. Hoatson, Modelling one- and two-dimensional solid-state NMR spectra, Magn. Reson. Chem. 40 (2002) 70–76.

[32] S. Jähnert, V. Chavez, G.E. Schaumann, A. Schreiber, M. Schönhoff, G.H. Findenegg, Melting and freezing of water in cylindrical silica nanopores, Phys. Chem. Chem. Phys. 10

(2008) 6039–6051.

[33] R.J. Wittebort, M.G. Usha, D.J. Ruben, D.E. Wemmer, A. Pines, Observation of Molecular Reorientation in Ice by Proton and Deuterium Magnetic Resonance, J. Am. Ceram. Soc. 110 (1988) 5668–5671.

[34] P. Waldstein, S.W. Rabideau, J.A. Jackson, Nuclear Magnetic Resonance of Single Crystals of D2O Ice, J. Chem. Phys. 41 (1964) 3407.

[35] R. Böhmer, G. Diezemann, G. Hinze, E. Rössler, Dynamics of supercooled liquids and glassy solids, Prog. Nucl. Magn. Reson. Spectrosc. 39 (2001) 191–267.

[36] J. Sjöström, J. Swenson, R. Bergman, S. Kittaka, Investigating hydration dependence of dynamics of confined water: Monolayer, hydration water and Maxwell-Wagner processes, J. Chem. Phys. 128 (2008) 154503.

[37] C. Lederle, M. Sattig, M. Vogel, Effects of partial crystallization on the dynamics of water in mesoporous silica, J. Phys. Chem. C. 122 (2018) 15427–15434.

[38] M. Alcoutlabi, G.B. McKenna, Effects of confinement on material behaviour at the nanometre size scale, J. Phys. Condens. Matter. 17 (2005) R461–R524.

[39] A.A. Levchenko, P. Jain, O. Trofymluk, P. Yu, A. Navrotsky, S. Sen, Nature of molecular rotation in supercooled glycerol under nanoconfinement, J. Phys. Chem. B. 114 (2010) 3070–3074.

Chapter 7

Coexistence of Structural and Dynamical Heterogeneity in Liquids Under Nanoconfinement

7.1 Abstract

Spatiotemporal heterogeneity is one of the hallmarks of the relaxation dynamics associated with the glass transition. A key question in this regard is whether the dynamical heterogeneity has a structural origin. We report differential scanning calorimetry (DSC) data that reveal the presence of extreme spatial heterogeneity in the freezing dynamics of water (D_2O) and the glass transition dynamics in the supercooled molecular liquid ortho-terphenyl (OTP), when these liquids are confined in nano-architected mesoporous silica with interconnected pores of different geometry. The results demonstrate, for the first time, that despite connectivity between the pores, nanoconfined water and OTP display distinct freezing/melting points and glass transition temperatures characteristic of each pore type. Viewed as a whole, these experimental results point to the coexistence of strong spatial heterogeneities over length scales of a few nanometers in the structure and dynamics of these liquids, suggesting a close mechanistic connection between them.

7.2 Introduction

The remarkable slowdown of the primary or α relaxation in supercooled liquids appears to necessitate the existence of a growing or even diverging length scale as the temperature approaches the glass transition temperature T_g upon cooling [1]. In fact, most of the experimental and simulation studies have indicated that a growing dynamical length scale is responsible for the sharp rise in the α-relaxation timescale near the glass transition [2–7]. Multi-point space-time correlation functions and related measurements suggest the appearance of long-lived spatially correlated dynamical clusters or regions of fast and slow dynamics that persist on the timescale of structural relaxation and the length scale of these clusters grows upon cooling [8]. These spatially heterogeneous dynamics are now believed to be a hallmark of the glass transition that can be linked to the nonlinear, non-Arrhenius and non-exponential nature of the relaxation process [9,10].

Although there is a possibility that the origin of the dynamical heterogeneity can be purely kinetic in the trajectory space and unrelated to any corresponding structural fluctuation [11], a number of simulation studies suggest that such heterogeneities may be closely associated with structural fluctuations at length scales corresponding to intermediate range order, i.e. they have a thermodynamic origin [2,12]. For example, clusters of slow dynamics have been identified in metallic glass-forming liquids with the appearance of interconnected regions of icosahedral ordering, while those in colloidal liquids are characterized by hexagonally close-packed structures with bond orientational order. However, direct experimental observation of such correspondence between structural and dynamical heterogeneity remains challenging. In this regard it is interesting to note that liquids such as water display pronounced structural and dynamical heterogeneity under nanoconfinement and freeze in a stepwise fashion [13–15].

The differences in the dynamical behavior between a liquid in bulk form and under nanoconfinement arises primarily from (i) the thermodynamic effect of curvature of the confined space and the fact that the length scale of confinement becomes comparable to or smaller than some characteristic length scale of the liquid as well as (ii) the structural effects exerted by the pore-liquid interface, such as oscillations in the molecular packing density of the liquid as a function of distance from the interface [16]. Extensive experimental and simulation studies in the recent past have indicated that such heterogeneity in the case of water confined in the pores of silica with pore diameters ranging between 2-20 nm can be linked to strong density layering [17]. In particular, water molecules remain strongly structured by the pore walls of silica up to a distance of ~ 1 nm from the wall and are characterized by significantly lower mobility and higher density, compared to bulk water. On the other hand, the density and mobility of the water molecules in the region beyond ~1 nm from the pore wall is believed to become increasingly similar to that of bulk water towards the center of the pore. Again a direct demonstration of the connection between the structural and dynamical heterogeneity in a confined liquid remains somewhat scarce in the literature, although recent simulation studies on partially pinned systems under neutral confinement provide interesting insights into such connections [18–21].

Here we present experimental evidence for extreme spatial heterogeneity in the freezing dynamics of water and in the glass transition dynamics in the van der Waals bonded supercooled molecular liquid ortho-terphenyl ($C_{18}H_{14}$, OTP), when these liquids are nanoconfined in architected mesoporous silica with interconnected pores of different geometry. Such heterogeneity is reminiscent of glassy dynamics and is manifested in the very first observation of two distinct freezing points for water and two glass transition temperatures (T_g) for supercooled OTP, where each transition corresponds to a specific pore geometry.

7.3 Experimental Methods

7.3.1 Sample preparation and physical characterization

Mesoporous silica powders with bimodal pores (FDU-5 and SBA-16) and with uniform cylindrical pores (SBA-15) were synthesized according to acidic reaction methods as previously reported [22–24]. To synthesize SBA-16, 3.0 g of triblock copolymer poly(ethylene oxide)$_{106}$-poly(propylene oxide)$_{70}$-poly(ethylene oxide)$_{106}$ (Pluronic® F127, Aldrich) were dissolved in 144 mL of deionized (DI) water and 144 mL of 2 M hydrochloric acid. Subsequently, 11 mL of butyl alcohol and 15 mL of tetraethyl orthosilicate (TEOS, Aldrich) were added. The solution was then kept in an oven at 45 °C for 24 hours, followed by a hydrothermal treatment at 100 °C for 24 hours. The resulting white precipitate was then washed with DI water and ethanol, dried in an oven at 70 °C and calcined at 500 °C for 3 hours. SBA-15 was synthesized by dissolving 4.0 g of triblock copolymer poly(ethylene oxide)$_{20}$-poly(propylene oxide)$_{70}$-poly(ethylene oxide)$_{20}$ (Pluronic® P123, Aldrich), in 30 mL of DI water and 120 mL of 2 M hydrochloric acid. Then, 9.1 mL of TEOS was added to the solution, which was kept at 37 °C for 20 hours. Subsequently, the mixture was placed in an oven at 70 °C for hydrothermal treatment for 16 hours. The resulting white precipitate was then washed with DI water and ethanol, dried in an oven at 70 °C and calcined at 500 °C for 3 hours. The synthesis of FDU-5 followed a procedure described in [22]. Briefly, 1.0 g of Pluronic® P123 and 0.115 g of sodium dodecyl sulfate were dissolved in a mixture of 26 g DI water and 12 g of 2 M hydrochloric acid at room temperature. 2.08 g of TEOS was added to this solution under vigorous stirring. The solution was kept at 30 °C for 24 hours, and then transferred into a Teflon autoclave and heated at 100 °C for another 24 hours. The precipitated solid was washed with DI water, dried in an oven at 70 °C and calcined at 550 °C for 3 hours.

The phase identification and lattice parameter determination of the mesoporous silica samples were carried out using powder x-ray diffraction (Fig. 7-1). The mesopore arrangement and pore size were evaluated, respectively, by transmission electron microscopy (TEM) and nitrogen adsorption-desorption analysis. Details of these experiments can be found in previous publications [19,20]. For TEM imaging, powders were dispersed in ethanol. A small amount of this dispersion was placed on a TEM grid by drop-casting and dried in air. TEM images of mesoporous materials were taken by a FEI Tecnai 12 transmission electron microscope (Fig. 7-2). Nitrogen adsorption/desorption isotherms were obtained using a Sorptometer (ASAP 2020, Micromeritics) at 77 K. The mesoporous materials were degassed at 523 K for 6 hours (3 mTorr)

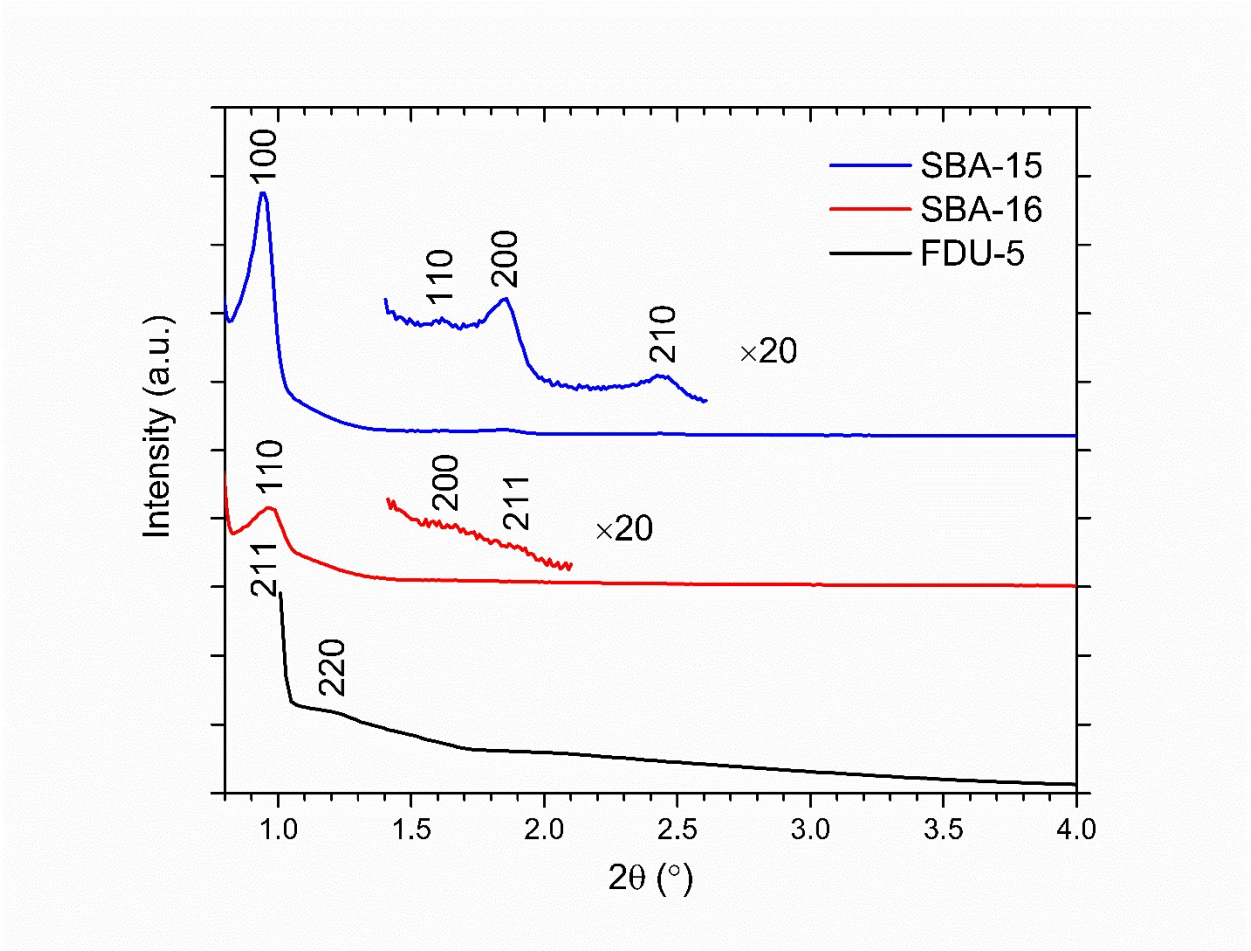

Figure 7-1 X-ray diffraction patterns of mesoporous silica SBA-15, SBA-16 and FDU-5.

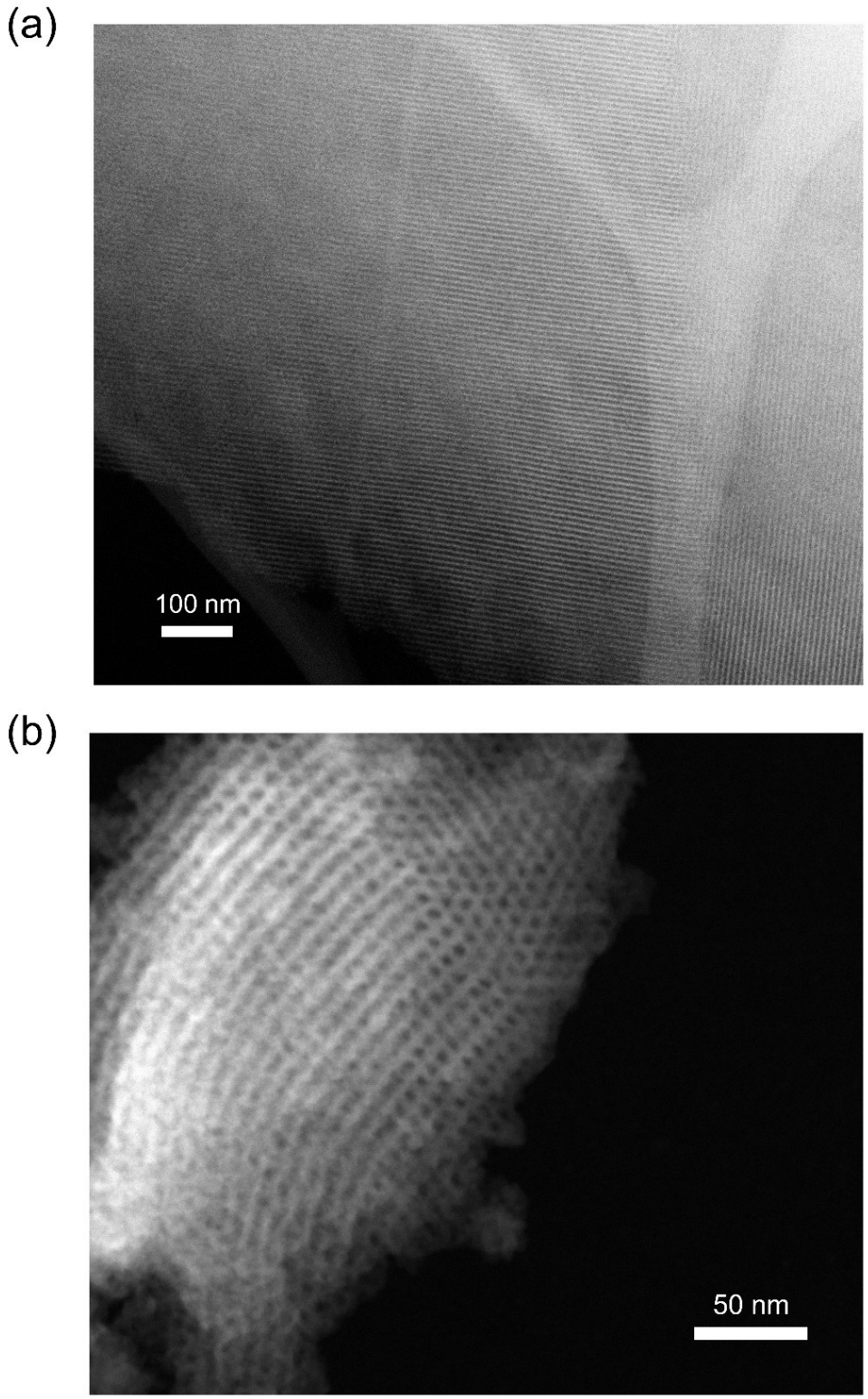

Figure 7-2 Scanning TEM images of (a) SBA-16 and (b) FDU-5 showing nano-sized ordered mesoporous structures.

prior to adsorption. The specific surface areas of the samples were calculated by the Brunauer-Emmett-Teller (BET) method, and pore size distributions were calculated by the Barrett-Joyner-Halenda (BHJ) and density functional theory (DFT) methods.

Mesostructure geometries and pore sizes for SBA-15, SBA-16 and FDU-5 were determined by a combination of TEM imaging, nitrogen adsorption/desorption analysis using BJH and DFT methods, and X-ray diffraction. Results from these three characterization methods were then compared to published results [23–27]. In detail, the cage-structured SBA-16 is characterized by large spherical pores (5.5 nm diameter) that are body-centered-cubic arranged (Fig. 7-3) and connected by narrow cylindrical openings (3.2 nm diameter and 1.5 to 2 nm in length). 3D large-pore FDU-5 possesses an *Ia*3*d*-type bicontinuous cubic mesostructural order with cylindrical pores of 8.7 nm in diameter. As shown in Fig. 7-3, at the crossing locations of the cylindrical pores, larger "pore-openings" occur. From *Ia*3*d* unit-cell analysis and pore size analysis, we estimate the length of the diagonal at the crossing of two identical cylinders to be 12.4 nm. Finally, the two mesostructured SBA-15 samples are characterized by cylindrical pores with diameters of 4 and 5 nm, arranged in a honeycomb-type hexagonal lattice (Fig. 7-3).

The Vycor-5, Vycor-109 and Vycor-145 porous silica glasses with average pore sizes of 5 nm, 10.9 nm and 14.5 nm, respectively, were obtained from Corning Inc. in the form of buttons of dimensions 6.9 mm diameter and 2.5 mm height. 'Thirsty' Vycor glass was prepared by baking all samples at 200 °C overnight to remove any adsorbed organic impurities.

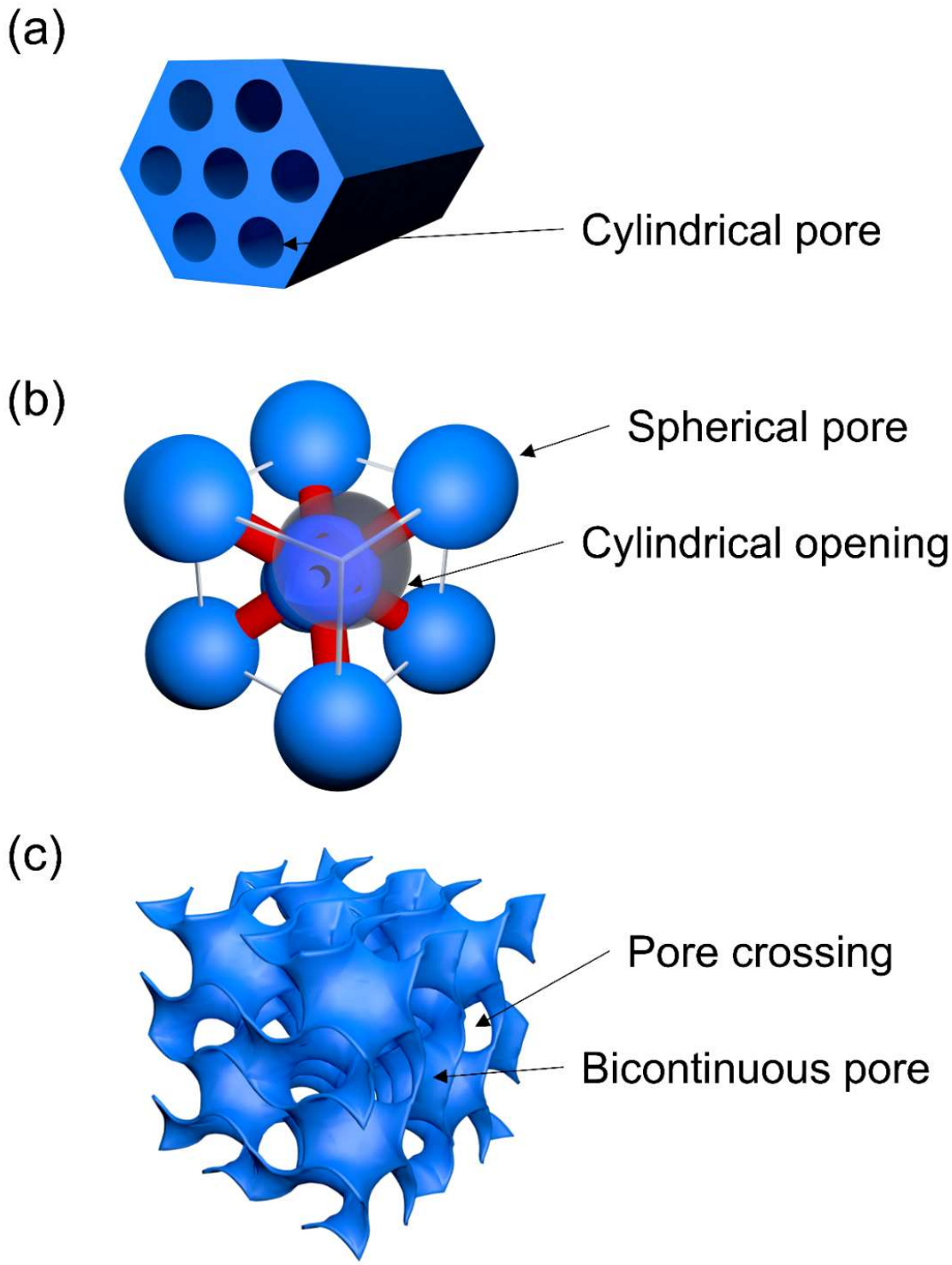

Figure 7-3 Schematic pore structure of mesoporous silica (a) SBA-15, (b) SBA-16 and (c) FDU-5.

D_2O was added to excess amount of as-prepared mesoporous silica powder and the mixture was stirred to obtain partially hydrated samples for DSC and NMR experiments. The thirsty Vycor glass buttons were immersed in pure D_2O (Aldrich) for 10 minutes to obtain fully hydrated samples. These samples were subsequently dried at ambient condition for 1 hour to remove any freezable bulk water on the sample surface through water evaporation, crushed into powder and used in DSC and NMR experiments.

Reagent grade OTP (Aldrich) was melted at 130 ℃ without further purification. Mesoporous silica powder and Vycor buttons were submerged in the OTP melt and equilibrated for 24 hours in a furnace. Precipitated powder and buttons were transferred into hermetically sealed aluminum pans and subsequently quenched in liquid nitrogen for DSC measurements.

7.3.2 Differential scanning calorimetry

The DSC measurements were carried out using a Mettler Toledo DSC1 differential scanning calorimeter. About 10-25 mg samples were hermetically sealed in 40 μL aluminum pans. Scans were taken in a flowing nitrogen environment with a heating rate of 5 K/min. Melting point and T_g were determined to within ± 2 °C as the onset of the corresponding endotherms. The temperature scale was calibrated to the onset of the melting endotherm of pure bulk D_2O at 277.0 K.

7.4 Results and Discussion

7.4.1 Freezing transition of water

DSC heating curves for D_2O in mesoporous silica SBA-15, SBA-16 and FDU-5 are shown in Fig. 7-4. While SBA-15 displays only one endothermic melting peak of water in the nanopores, two endothermic peaks are observed for SBA-16 and FDU-5 corresponding to the melting of water confined in the two pore types in these bimodal pore structures. The depression of the melting temperature T_m of confined D_2O in these systems, corresponding to the onset of the DSC endothermic peak, with respect to the bulk value T_{mB} approximately obeys the Gibbs-Thompson

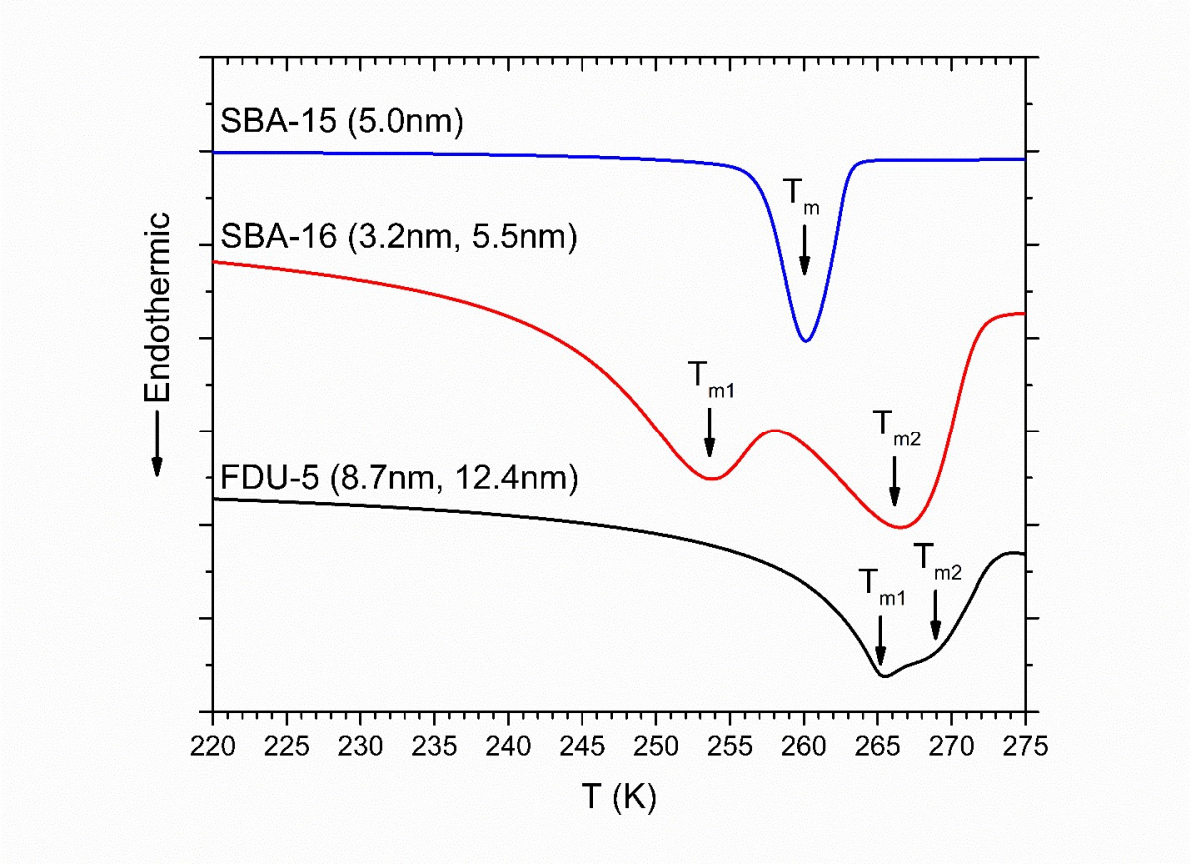

Figure 7-4 DSC melting scans for D_2O confined in SBA-15, SBA-16 and FDU-5. Corresponding pore diameters are given alongside the scans. T_m corresponding to melting in nanopores are indicated by solid arrows.

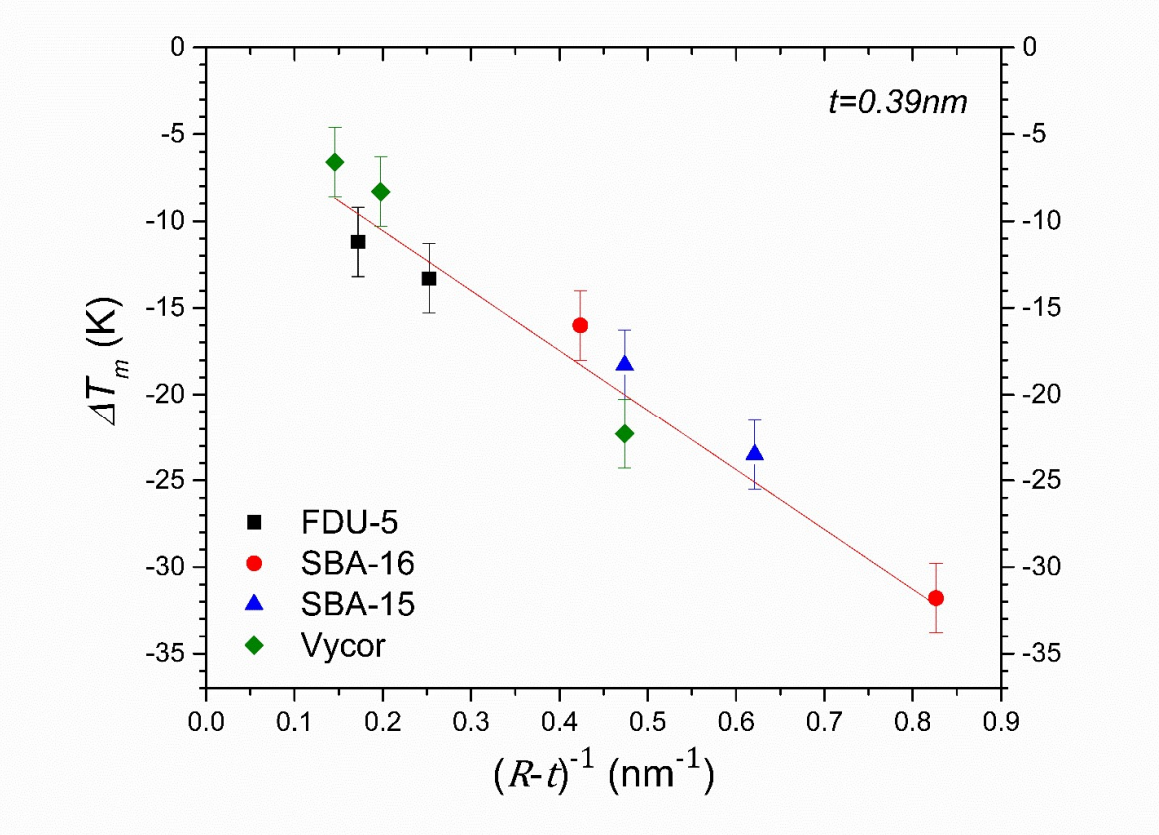

Figure 7-5 Depression of melting point as a function of inverse of effective pore radius. Red straight line through the data points is a linear least-squares fit of the simplified Gibbs-Thomson equation $\Delta T_m = K/(R-t)$ where t is the thickness (0.4 nm) of the statistical monolayer of water molecules attached to the pore wall. Data for Vycor-5, Vycor-109 and Vycor-145 samples are taken from a previous study [15].

(G-T) relation as $\Delta T_m = (T_{mB} - T_m)$ varies nearly linearly with the inverse of the effective pore size R (Fig. 7-5). This result is consistent with those reported in previous studies of similar behavior of water under nanoconfinement in monodispersed pores and suggests that the volume to interface ratio dominates the freezing point depression behavior of water in mesoporous silica [28,29]. However, and more interestingly, the observation in the present study of two different freezing points for the two pore sizes in SBA-16 and FDU-5 with interconnected pores implies that under nanoconfinement the dynamical characteristics of water molecules in each pore type can be preserved in spite of the fact that these pores are completely interconnected. Therefore, the

nanoconfined water is dynamically heterogeneous, even over distances on the order of a few nanometer (see below). Moreover, the difference in the volume to interface ratio between the two pore types would also imply corresponding differences in the length scale of structuring of the water molecules. Thus, these results, when taken together, suggest a close connection between the structural and dynamical heterogeneities in nanoconfined liquids.

7.4.2 Glass transition of supercooled OTP

DSC heating curves for glassy OTP confined in dual pore SBA-16 and FDU-5 samples are shown in Fig. 7-6a. In each case, two T_g peaks are observed, both of which are below the bulk OTP glass transition temperature of ~299 K, corresponding to the glass transition in the two pore types. On the other hand, the SBA-15 and Vycor samples with nearly unimodal pore sizes display only one T_g (Fig. 7-6b). Interestingly, and in contrast with the melting/freezing transition of water, the glass transition of OTP does not display an approximately universal dependence of $\Delta T_g = \left(T_{gB} - T_g\right)$ on the pore size R (Fig. 7-7), in spite of the chemical similarity of the host structures. Instead, two separate linear trends are observed for the crystalline mesoporous silica and amorphous Vycor samples in accordance with the G-T relationship. This result may be suggestive of the differences in the strength of the pore-liquid interfacial interaction and the interface roughness between the crystalline and the amorphous structures [16].

It is well known that similar to the thermodynamic freezing/melting transition, the kinetic process of glass transition of supercooled liquids could also be strongly affected by confinement of the liquid to nanometer length scales. However, the corresponding response is known to be non-universal in the sense that T_g can either increase or decrease with the dimensionality and extent of confinement [16]. Nanoconfinement can affect the dynamics of a supercooled liquid in two

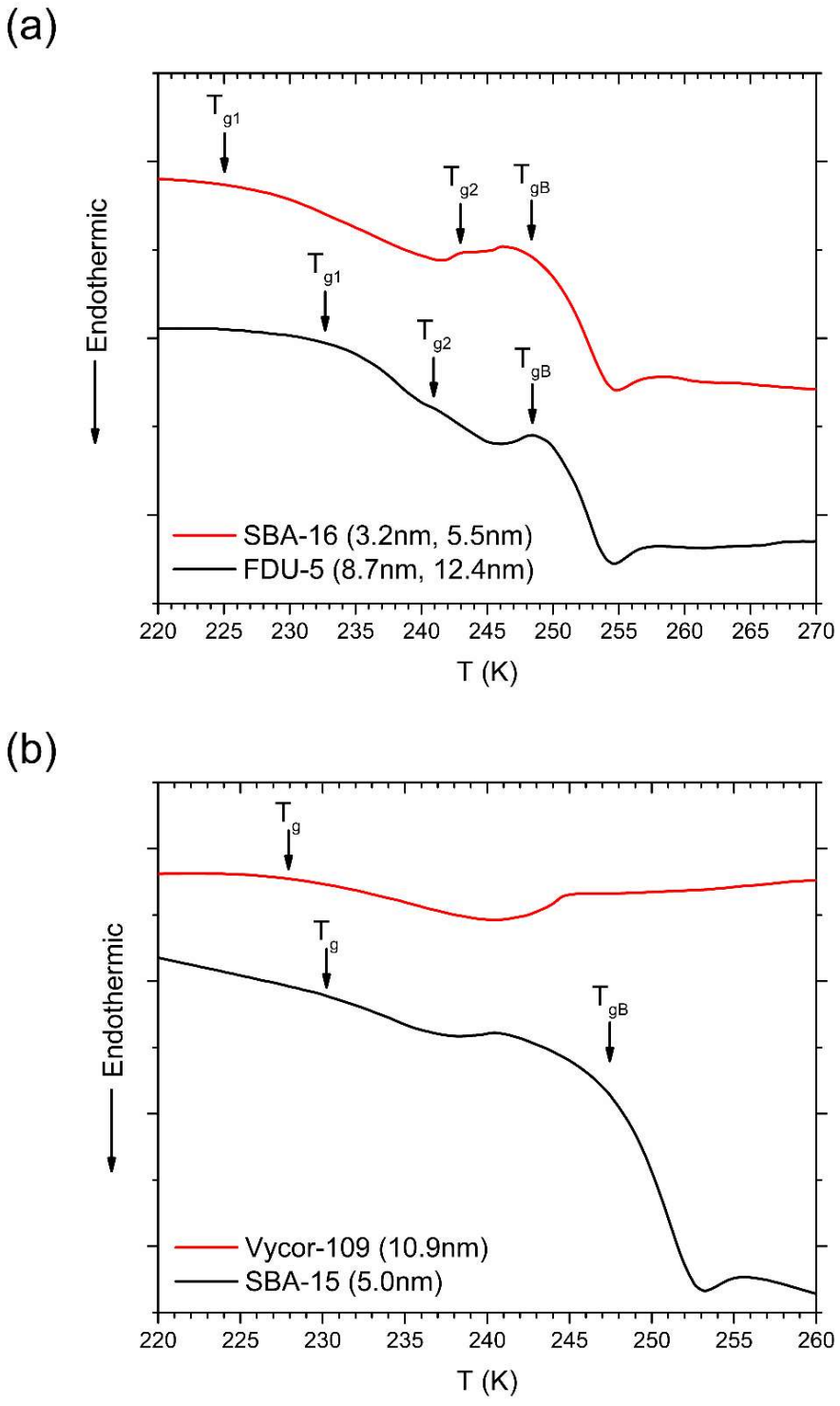

Figure 7-6 DSC heating scans for OTP confined in (a) SBA-16 and FDU-5, (b) SBA-15 and Vycor-109. Scans for other vycor samples are not shown. T_g corresponding to glass transition in nanopores and signals from bulk OTP (T_{gB}) are indicated by solid arrows.

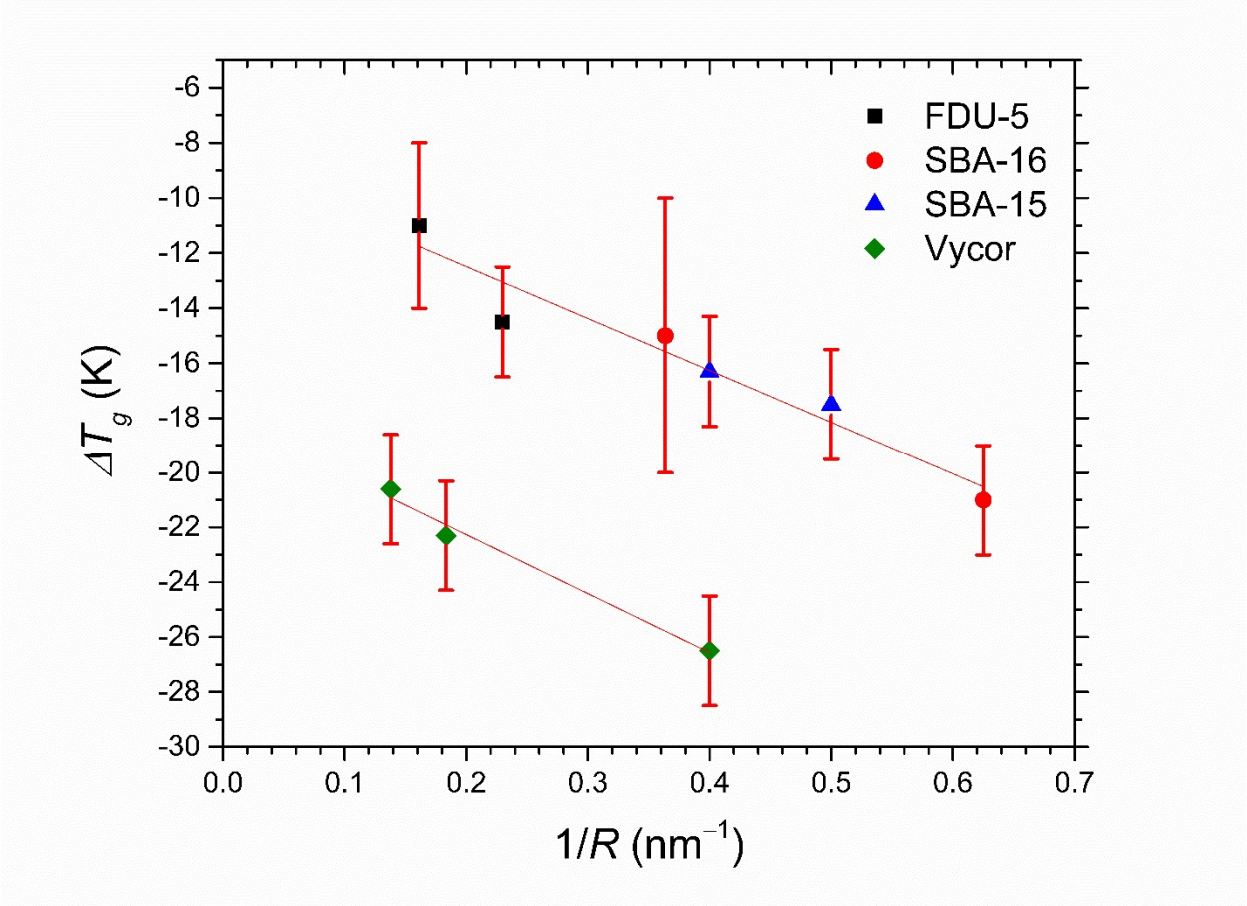

Figure 7-7 Depression of T_g of OTP nanoconfined in FDU-5 (black square), SBA-16 (red circle), SBA-15 (blue triangles) and Vycor samples (green diamonds) determined from the DSC scans, as a function of the inverse of pore radius R. Straight lines through the data are guide to the eye.

ways. First, if the length scale of confinement becomes comparable to or smaller than that of the cooperatively rearranging regions (CRR) responsible for structural or α-relaxation, then the effect of cooperative molecular dynamics and the temperature dependence of configurational entropy are greatly diminished, which would result in an enhancement in the liquid dynamics, resulting in a lowering of T_g [30]. The volume of the CRRs near glass transition is expected to have the dimension of 100-200 molecules [31], which corresponds to a characteristic length scale of the CRRs on the order of approximately 6 molecular diameters, which for OTP is ~ 4.5 nm. Therefore, the pore sizes of the mesoporous silica samples studied here may indeed satisfy this condition,

which is consistent with the observed depression in T_g. Second, the relative effects of the pore-liquid interface on the structuring of the liquid become stronger as the length scale of confinement decreases and the interface:bulk ratio increases, although the sign of change in T_g from the interface effect cannot be predicted a priori and can be positive or negative. However, both configurational entropy and interface effects are expected to influence the structure of the confined liquid. Therefore, similar to the two T_m for the freezing transition of water, the observation of two T_g for OTP confined in the interconnected two-pore structures suggests coexistence of structural and dynamical heterogeneities and their preservation over length scales that are on the order of the pore dimensions. The self-diffusion coefficient for OTP molecules near T_g is ~ 10^{-16} cm^2/s [32] and the relaxation timescale is on the order of ~ 100 s, which yields a characteristic molecular diffusion distance of ~1 nm during relaxation. Therefore, the diffusion distances during structural relaxation are of the same order of magnitude as the pore dimensions in SBA-16 and FDU-5, and yet the structural and dynamical heterogeneities can be preserved over the same length scales and timescales. This observation indicates that the preservation of the dynamical heterogeneity is only possible because the liquid structure in each pore type is unique and cannot be homogenized, thus suggesting a close connection between the structure and dynamics in liquids under nanoconfinement.

7.5 Conclusion

In summary, we report a systematic study of the melting and freezing dynamics of D_2O and the glass transition dynamics of supercooled OTP confined in the nanopores of glassy and crystalline solid silica matrices using DSC. The observation of two distinct melting points for water and two glass transition temperatures for OTP nanoconfined in the interconnected pores of two different diameters in mesoporous silica SBA-16 and FDU-5 indicates the coexistence of structural and dynamical heterogeneity in these liquids at length scales on the order of a few nanometer. Collectively, these results suggest a close mechanistic connection between structure and dynamics in both liquids.

References

[1] A. Cavagna, Supercooled Liquids for Pedestrians, Phys. Rep. 476 (2009) 51–124.

[2] M.S.G. Razul, G.S. Matharoo, P.H. Poole, Spatial correlation of the dynamic propensity of a glass-forming liquid, J. Phys. Condens. Matter. 23 (2011) 235103.

[3] K. Schmidt-Rohr, H.W. Spiess, Nature of Nonexponential Loss of Correlation above the Glass Transition Investigated by Multidimensional NMR, Phys. Rev. Lett. 66 (1991) 3020–3023.

[4] D. Chandler, J.P. Garrahan, Dynamics on the Way to Forming Glass: Bubbles in Space-Time, Annu. Rev. Phys. Chem. 61 (2010) 191–217.

[5] L. Berthier, G. Biroli, J.-P. Bouchaud, L. Cipelletti, W. van Saarloos, eds., Dynamical Heterogeneities in Glasses, Colloids, and Granular Media, Oxford University Press, USA, 2011.

[6] S. Karmakar, C. Dasgupta, S. Sastry, Growing Length and Time Scales in Glass-Forming Liquids, Proc. Natl. Acad. Sci. 106 (2009) 3675–3679.

[7] K. Kim, S. Saito, Multiple Length and Time Scales of Dynamic Heterogeneities in Model Glass-Forming Liquids: A Systematic Analysis of Multi-Point and Multi-Time Correlations, J. Chem. Phys. 138 (2013) 12A506.

[8] L. Berthier, G. Biroli, Theoretical Perspective on the Glass Transition and Amorphous Materials, Rev. Mod. Phys. 83 (2011) 587–645.

[9] J.C. Dyre, Colloquium: The Glass Transition and Elastic Models of Glass-Forming Liquids, Rev. Mod. Phys. 78 (2006) 953–972.

[10] M.D. Ediger, Spatially Heterogeneous Dynamics in Supercooled Liquids, Annu. Rev. Phys. Chem. 51 (2000) 99–128.

[11] L.O. Hedges, R.L. Jack, J.P. Garrahan, D. Chandler, Dynamic Order-Disorder in Atomistic Models of Structural Glass Formers, Science (80-.). 323 (2009) 1309–1313.

[12] T. Kawasaki, H. Tanaka, Structural Origin of Dynamic Heterogeneity in Three-Dimensional Colloidal Glass Formers and its Link to Crystal Nucleation, J. Phys. Condens. Matter. 22 (2010) 232102.

[13] S.A. Lusceac, M.R. Vogel, C.R. Herbers, 2H and 13C NMR studies on the temperature-dependent water and protein dynamics in hydrated elastin, myoglobin and collagen, Biochim. Biophys. Acta. 1804 (2010) 41–48.

[14] M. Sattig, M. Vogel, Dynamic crossovers and stepwise solidification of confined water: A 2H NMR study, J. Phys. Chem. Lett. 5 (2014) 174–178.

[15] Y. Xia, H. Cho, M. Deo, S.H. Risbud, M.H. Bartl, S. Sen, Layer-by-Layer Freezing of Nanoconfined Water, Sci. Rep. 10 (2020) 5327.

[16] S. Napolitano, E. Glynos, N.B. Tito, Glass Transition of Polymers in Bulk, Confined Geometries, and Near Interfaces, Rep. Prog. Phys. 80 (2017) 036602.

[17] I.C. Bourg, C.I. Steefel, Molecular dynamics simulations of water structure and diffusion

in silica nanopores, J. Phys. Chem. C. 116 (2012) 11556–11564.

[18] W. Kob, S. Roldán-Vargas, L. Berthier, Non-monotonic temperature evolution of dynamic correlations in glass-forming liquids, Nat. Phys. 8 (2012) 164–167.

[19] F. Klameth, P. Henritzi, M. Vogel, Static and dynamic length scales in supercooled liquids: Insights from molecular dynamics simulations of water and tri- propylene oxide, J. Chem. Phys. 140 (2014) 144501.

[20] G.M. Hocky, T.E. Markland, D.R. Reichman, Growing Point-to-Set Length Scale Correlates with Growing Relaxation Times in Model Supercooled Liquids, Phys. Rev. Lett. 108 (2012) 225506.

[21] R. Horstmann, E.P. Sanjon, B. Drossel, M. Vogel, Effects of confinement on supercooled tetrahedral liquids, J. Chem. Phys. 150 (2019) 214704.

[22] D. Zhao, S. Qiu, Y. Tang, C. Yu, eds., Recent Progress in Mesostructured Materials, Volume 165, Proceedings of the 5th International Mesostructured Materials Symposium (IMMS 2006) Shanghai, China, August 5-7, 2007.

[23] D. Zhao, Q. Huo, J. Feng, B.F. Chmelka, G.D. Stucky, Nonionic triblock and star diblock copolymer and oligomeric surfactant syntheses of highly ordered, hydrothermally stable, mesoporous silica structures, J. Am. Chem. Soc. 120 (1998) 6024–6036.

[24] H. Maheshwari, J.D. Roehling, B.A. Turner, J. Abdinor, T.B. Tran-Roehling, M.D. Deo, M.H. Bartl, S.H. Risbud, K. van Benthem, Robust mesoporous silica compacts: multi-scale characterization of microstructural changes related to physical–mechanical properties, J. Mater. Sci. 51 (2016) 1–11.

[25] Y. Ishii, Y. Nishiwaki, A. Al-Zubaidi, S. Kawasaki, Pore Size Determination in Ordered Mesoporous Materials Using Powder X-Ray Diffraction, J. Phys. Chem. C. 117 (2013) 18120–18130.

[26] F. Carniato, G. Paul, C. Bisio, S. Caldarelli, L. Marchese, On the Organic/Inorganic Interface Between Mesoporous SBA-16 Silica and its Structural Directing Polymer: a Combined FT-IR and Solid State NMR Study, RSC Adv. 2 (2012) 1153–1160.

[27] X. Liu, B. Tian, C. Yu, F. Gao, S. Xie, B. Tu, R. Che, L. Peng, D. Zhao, Room-Temperature Synthesis in Acidic Media of Large-Pore Three-Dimensional Bicontinuous Mesoporous Silica with Ia3d Symmetry, Angew. Chem. Int. Ed. 41 (2002) 3876–3878.

[28] S. Kittaka, S. Takahara, H. Matsumoto, Y. Wada, T.J. Satoh, T. Yamaguchi, Low temperature phase properties of water confined in mesoporous silica MCM-41: thermodynamic and neutron scattering study, J. Chem. Phys. 138 (2013) 204714.

[29] K. Morishige, H. Yasunaga, Y. Matsutani, Effect of pore shape on freezing and melting temperatures of water, J. Phys. Chem. C. 114 (2010) 4028–4035.

[30] M. Alcoutlabi, G.B. McKenna, Effects of confinement on material behaviour at the nanometre size scale, J. Phys. Condens. Matter. 17 (2005) R461–R524.

[31] J.D. Stevenson, J. Schmalian, P.G. Wolynes, The Shapes of Cooperatively Rearranging Regions in Glass-Forming Liquids, Nat. Phys. 2 (2006) 268–274.

[32] M.K. Mapes, S.F. Swallen, M.D. Ediger, Self-Diffusion of Supercooled o-Terphenyl near

the Glass Transition Temperature, J. Phys. Chem. B. 110 (2006) 507–511.

Chapter 8
Conclusions and Future Work

The viscoelastic behavior of supercooled As-Se and Ge-Se liquids is investigated using oscillatory parallel-plate rheometry. The rheological spectra of Se-rich liquids indicates the presence of two relaxation processes which are assigned to a fast disjointed Se-chain segmental motion and a slow bond scission/renewal dynamics [1]. Upon addition of crosslinking Ge/As atoms, the fast process corresponding to the 'floppy' modes disappears in liquids with higher network connectivity or average coordination number $\langle r \rangle$, implying a dynamical rigidity transition. In the case of metaphosphate liquids consisting of long chains of PO_4 tetrahedra, the rheological results indicate that liquids containing low field strength cations such as Ag and weak inter-chain interaction are thermorheologically complex, while they become thermorheologically simple with stronger interchain crosslinking provided by high field strength modifiers such as Zn. The thermorheological complexity of these fragile liquids with weak network connectivity suggest the existence of multiple relaxation processes, where the segmental motion of $[PO_3]_n^{-1}$ chains is likely responsible for shear relaxation in these liquids, in addition to the reported P–O bond breaking dynamics in network phosphate liquids in literature [2]. The physical assignment of the segmental chain motion to the shear relaxation process is directly corroborated in a short-chain silver phosphate liquid using high temperature ^{31}P NMR spectroscopy. This scenario is further investigated in a mixed-cation Na-Zn metaphosphate system, where the network connectivity contributed from the modifier-oxygen interchain crosslinking can be tuned by the Na:Zn ratio. Two relaxation processes with time scales differing over two orders of magnitude are observed in the relaxation spectra obtained from the rheological results. The P-O bond scission/renewal dynamics is found to exist at longer timescales for all metaphosphate liquids. The contribution of the bond scission/renewal dynamics to relaxation becomes weaker with progressive addition of alkali cations to the network and this process becomes more strongly coupled to the segmental

dynamics of $[PO_3]_n^{-1}$ chains in Na-deficient compositions, which reduces the thermorheological complexity.

The results presented in this dissertation suggest that the high fragility of Se-rich chalcogenide liquids and Na-rich metaphosphate liquids originates from the conformational entropy of Se-chains and PO_4 tetrahedral chains, respectively. A floppy to rigid transition threshold at $\langle r \rangle \sim 2.2$ is observed in the As-Se and Ge-Se systems, instead of the conventional value of 2.4 proposed by Phillips and Thorpe [3,4]. The fragility index m of supercooled metaphosphate liquids can vary over a rather large range spanning from ~ 30 to 90 and shows a systematic trend with the extent and the strength of crosslinking provided by modifier-oxygen connection. As interaction between the modifier cation and metaphosphate chains increases, a shortening of effective chain length results from the stronger pinning effect on the chain reorientation. When taken together, the compositional variation of fragility of Se-contained chalcogenide and metaphosphate systems display an intriguing correlation with the conformational entropy of the constituent Se and $[PO_3]_n^{-1}$ chains. Our findings provide a novel understanding of the origin of fragility in chain dominated glass-forming systems. It would be thus of considerable importance to extend these investigations to other chalcogenide and oxide amorphous systems that are dominated by different structural moieties such as rings, molecules or 3-dimensional network. Good candidates in the oxide family include binary alkali and alkaline-earth borates, where a mixture of structural units such as boroxol rings and three and four coordinated boron atoms can coexist in the glass network. Another interesting candidate is the vanadate glass-forming liquids, which is characterized by low melting temperature and optimal electronic properties for semiconducting applications. Vanadate glasses have a similar structure as phosphate glasses where

V atoms are primarily fourfold coordinated with the existence of V=O bonds [5]. Besides, the presence of some fraction of VO_5 groups can modulate the network connectivity.

The dynamics of nanoconfined water and of molecular liquid OTP in mesoporous silica matrices from the SBA, MCM and FDU families are investigated using a combination of DSC and ^{2}H NMR spectroscopy. DSC measurements provide the first observation of two melting points and two glass transition temperatures corresponding to the liquids confined in two interconnected pores of different size and shapes. The results indicate the coexistence of structural and dynamical heterogeneity for both liquids at length scale of a few angstroms. ^{2}H NMR spectroscopic results revealed a layer-by-layer freezing process of water under nanoconfinement where the mobile liquid-like water molecules and rigid solid-like water molecules coexist far below the bulk water freezing point. Such a model also provides an explanation for the apparent fragile-to-strong transition in the temperature dependence of the relaxation time observed for nanoconfined water. When taken together, our findings indicate a close relation between structure and dynamics in fluids under nanoconfinement. Despite the promising results in this work, there are potential knowledge gaps for a deeper atomistic understanding on the confinement effect. One future research direction would be to separate the spatial and interfacial effects of nanoconfinement. On the other hand, a systematic study combining the glass transition behavior under nanoconfinement with simultaneous measurement of the structural evolution of the liquid would be highly insightful to explore if there is any universality hidden in the apparently nonuniversal effect of confinement on T_g.

References

[1] W. Zhu, B. Aitken, S. Sen, Investigation of the shear relaxation behavior of As-Se liquids within the framework of entropic and elastic models of viscous flow, J. Non. Cryst. Solids. 534 (2020) 119959.

[2] S. Wegner, L. Van Wu, G. Tricot, Network Dynamics and Species Exchange Processes in Aluminophosphate Glasses : An in situ High Temperature Magic Angle Spinning NMR View, J. Phys. Chem. B. 113 (2009) 416–425.

[3] J.C. Phillips, Topology of covalent non-crystalline solids: Short-range order in chalcogenide alloys, J. Non. Cryst. Solids. 34 (1979) 153–181.

[4] M.F. Thorpe, Continuous deformations in random networks, J. Non. Cryst. Solids. 57 (1983) 355–370.

[5] U. Hoppe, R. Kranold, J.M. Lewis, C.P. O'Brien, H. Feller, S. Feller, M. Affatigato, J. Neuefeind, A.C. Hannon, Structure of binary alkaline earth vanadate glasses: an x-ray and neutron diffraction investigation, Phys. Chem. Glas. 44 (2003) 272–279.